

**STUDY OF JET TRANSVERSE MOMENTUM AND JET RAPIDITY
DEPENDENCE OF DIJET AZIMUTHAL DECORRELATIONS
WITH THE DØ DETECTOR**

by

Kiran Chakravarthula, B.Tech., M.S.

A Dissertation Presented in Partial Fulfillment
of the Requirements for the Degree
Doctor of Philosophy

COLLEGE OF ENGINEERING AND SCIENCE
LOUISIANA TECH UNIVERSITY

August 2012

Replace this page with the Signature Page.

ABSTRACT

In a collision experiment involving highly energetic particles such as hadrons, processes at high momentum transfers can provide information useful for many studies involving Quantum Chromodynamics (QCD). One way of analyzing these interactions is through angular distributions. In hadron-hadron collisions, the angular distribution between the two leading jets with the largest transverse momentum (p_T) is affected by the production of additional jets. While soft radiation causes small differences in the azimuthal angular distribution of the two leading jets produced in a collision event, additional hard jets produced in the event have more pronounced influence on the distribution of the two leading jets produced in the collision. Thus, the dijet azimuthal angular distribution can serve as a variable that can be used to study the transition from soft to hard QCD processes in a collision event. This dissertation presents a triple-differential study involving the azimuthal angular distribution and the jet transverse momenta, and jet rapidities of the first two leading jets. The data used for this research are obtained from proton-antiproton ($p\bar{p}$) collisions occurring at a center of mass energy of 1.96 TeV, using the DØ detector in Run II of the Tevatron Collider at the Fermi National Accelerator Laboratory (FNAL) in Illinois, USA. Comparisons are made to perturbative QCD (pQCD) predictions at next-to-leading order (NLO).

Replace this page with the approval for scholarly dissemination form.

DEDICATION

To my mother, Mrs. Chandrakala,
for inspiring me at a young age about physics
and about pursuing a Ph.D. program

To my father, Mr. Srinivasa Sarma,
for inspiring me with his energy levels
and supporting us all for all that we chose

To my brother, Mr. Praveen,
for inspiring me to embark on quests for knowledge
and supporting me with more than just his sound advice

TABLE OF CONTENTS

ABSTRACT	iii
DEDICATION	v
LIST OF TABLES	ix
LIST OF FIGURES	x
ACKNOWLEDGMENTS	xiii
CHAPTER 1 INTRODUCTION	1
CHAPTER 2 PHENOMENOLOGY	3
2.1 The Standard Model	3
2.2 Quantum Chromodynamics	5
2.2.1 Strong Coupling Constant	9
2.2.2 Parton Distribution Functions.....	10
2.3 Introduction to Jets	11
2.4 Dijet Azimuthal Decorrelations.....	14
2.5 Previous Measurements of Dijet Azimuthal Decorrelations	15
2.6 Phase Space Definition.....	16
2.7 Theory Predictions.....	17
CHAPTER 3 EXPERIMENTAL SETUP	21
3.1 The Tevatron Collider	21
3.2 The DØ Detector	24

3.2.1	Tracking System	26
3.2.2	Preshower Detectors	27
3.2.3	Calorimetry	28
3.2.4	Muon System.....	32
3.2.5	Luminosity Monitor.....	33
3.2.6	Triggers.....	34
3.2.7	Data Acquisition at D \emptyset	37
3.3	Jet Energy Calibration and p_T Resolution.....	38
3.3.1	Jet Energy Calibration	38
3.3.2	p_T Resolution.....	43
3.4	Detector Simulation	43
CHAPTER 4 MEASUREMENT PROCEDURE		45
4.1	Data Selection	45
4.2	Triggers	48
4.3	The Observable $R_{\Delta\phi}$	50
4.4	Correction Factors.....	52
4.5	Systematic Uncertainties.....	54
CHAPTER 5 RESULTS		56
CHAPTER 6 CONCLUSIONS AND OUTLOOK		60
6.1	Conclusions	60
6.2	Outlook	61
APPENDIX A TRIGGER EFFICIENCIES		62
APPENDIX B CORRECTION FACTORS		76

APPENDIX C SYSTEMATIC UNCERTAINTIES	83
BIBLIOGRAPHY	92

LIST OF TABLES

Table 4.1: H_T ranges and integrated luminosities for triggers in this analysis 50

LIST OF FIGURES

Figure 2.1: The Standard Model of Physics.....	4
Figure 2.2: Feynman diagrams for 2-jet production.....	9
Figure 2.3: PDFs for various quark flavors and a gluon.....	10
Figure 2.4: Dijet azimuthal angular decorrelation in radiative processes.....	14
Figure 2.5: Angular distributions for LO/NLO pQCD predictions overlaid on the experimental data	15
Figure 2.6: Hadronization corrections for $R_{\Delta\phi}$	19
Figure 2.7: Underlying event corrections for $R_{\Delta\phi}$	20
Figure 2.8: Total non-perturbative corrections for $R_{\Delta\phi}$	20
Figure 3.1: Fermilab's accelerator chain.....	23
Figure 3.2: The Run II D \emptyset detector	25
Figure 3.3: The coordinate system for the D \emptyset detector	26
Figure 3.4: Central tracking system of the D \emptyset detector	27
Figure 3.5: The D \emptyset calorimeter in Run II	29
Figure 3.6: Readout chain of the D \emptyset calorimeter	31
Figure 3.7: Schematic of a quadrant of the D \emptyset calorimeters showing the distribution of pseudorapidity.....	32
Figure 3.8: Integrated luminosity in Run II.....	34
Figure 3.9: Data flow in D \emptyset triggers	36
Figure 3.10: Trigger framework in D \emptyset triggers.....	37

Figure 3.11: Jet energies at parton, particle, and calorimeter levels.....	39
Figure 4.1: Event counts per bin.....	51
Figure 4.2: $R_{\Delta\phi}$ distributions overlaid with detector-level SHERPA and PYTHIA Monte Carlo simulations	51
Figure 4.3: Total correction factors obtained from fast-parametrized Monte Carlo simulations	53
Figure 4.4: Upper and lower variation of the total systematic uncertainties	55
Figure 5.1: Observable $R_{\Delta\phi}$ along with LO and NLO pQCD predictions.....	56
Figure 5.2: Observable $R_{\Delta\phi}$ as a function of y^* in selected H_T regions and for different $\Delta\phi_{max}$ requirements.....	57
Figure 5.3: Ratio of the data and theory	58
Figure A.1: Trigger turn-on curves (Trigger: JT45; $0.0 < y^* < 0.5$)	64
Figure A.2: Trigger turn-on curves (Trigger: JT45; $0.5 < y^* < 1.0$)	65
Figure A.3: Trigger turn-on curves (Trigger: JT45; $1.0 < y^* < 2.0$)	66
Figure A.4: Trigger turn-on curves (Trigger: JT65; $0.0 < y^* < 0.5$)	67
Figure A.5: Trigger turn-on curves (Trigger: JT65; $0.5 < y^* < 1.0$)	68
Figure A.6: Trigger turn-on curves (Trigger: JT65; $1.0 < y^* < 2.0$)	69
Figure A.7: Trigger turn-on curves (Trigger: JT95; $0.0 < y^* < 0.5$)	70
Figure A.8: Trigger turn-on curves (Trigger: JT95; $0.5 < y^* < 1.0$)	71
Figure A.9: Trigger turn-on curves (Trigger: JT95; $1.0 < y^* < 2.0$)	72
Figure A.10: Trigger turn-on curves (Trigger: JT125; $0.0 < y^* < 0.5$)	73
Figure A.11: Trigger turn-on curves (Trigger: JT125; $0.5 < y^* < 1.0$)	74
Figure A.12: Trigger turn-on curves (Trigger: JT125; $1.0 < y^* < 2.0$)	75
Figure B.1: Correction factors for jet ID efficiency, obtained from fast-parametrized Monte Carlo simulations	78

Figure B.2: Correction factors for inclusion of muons and neutrinos, obtained from fast-parametrized Monte Carlo simulations.....	79
Figure B.3: Correction factors for η resolution, obtained from fast-parametrized Monte Carlo simulations	80
Figure B.4: Correction factors for ϕ resolution, obtained from fast-parametrized Monte Carlo simulations	81
Figure B.5: Correction factors for p_T resolution, obtained from fast-parametrized Monte Carlo simulations	82
Figure C.1: Upper and lower variation of the JES uncertainty.....	85
Figure C.2: Upper and lower variation of the p_T resolution uncertainty	86
Figure C.3: Upper and lower variation of the ϕ uncertainty.....	87
Figure C.4: Upper and lower variation of the η resolution uncertainty	88
Figure C.5: Upper and lower variation of the η bias uncertainty	89
Figure C.6: Upper and lower variation of the jet ID effiency uncertainty.....	90
Figure C.7: Upper and lower variation of the vertex uncertainty	91

ACKNOWLEDGMENTS

This is my opportunity to thank all those individuals who helped me in completing my research successfully and documenting the same in the form of my dissertation. My parents, Mr. N. C. S. Sarma and Mrs. N. C. Chandrakala, and my brother and sister-in-law, Praveen Chakravarthula and Smitha Iyer-Chakravarthula, were with me all along, expending their love, energy, and hopes on my well-being in this distant land as I pursue my academic goals. I sincerely thank them for giving me all they could, and sometimes more, including emotional support however frequently I may have needed it.

I sincerely thank Dr. Markus Wobisch for being my research advisor, a friend, philosopher, and guide, supporting me in as many ways as he could, sometimes even extending beyond his bounds. I also thank Dr. H. Lee Sawyer, Jr. for agreeing to be on my Advisory Committee, helping me through as the Program Chair of Physics right from the time of my admission into the Ph.D. program. Dr. Zeno D. Greenwood receives my sincere thanks for agreeing to be on the Advisory Committee and for his critical and useful comments that helped me understand the project better. I also extend my thanks to Drs. Sumeet Dua and David Hall for agreeing to be on the Advisory Committee and providing their insights during my proposal defense and dissertation defense. Comments and support from colleagues at Fermilab, particularly those that are part of the QCD Working Group: Don Lincoln, Dmitry Bandurin,

Mandy Rominsky, Zdenek Hubacek, Sabine Lammers are much appreciated. It was a pleasure to be work on the Inter-Cryostat Detector during the 2009 shut-down of the DØ detector at Fermilab, and I appreciate the help of Heather Brown, Abhinav Dubey, Walter Geist, and Andrew White during that time. I also thank all the DØ Collaboration members that helped me while I was monitoring the Calorimeter and Muon Systems in the Control Room through numerous shifts; this experience and knowledge had helped me understand and appreciate the experiment better. My thanks are also due to all the authors and scholars who have enlightened me with the knowledge that they imparted to me through their books, articles, presentations, and posters. Particular thanks are also due to my research group members, Ramasudhakar Dhullipudi and Scott Atkins, who helped me through parts of my work with their guidance and to the other members, Anirvan Sircar and Rajivalochan Subramaniam, interactions with whom helped me get some more clarity. I also profusely thank Ms. Lori Gaskin in the Department of Chemistry and Physics for all the help and timely paperwork that she had done during the course of my Ph.D., also literally going that extra mile to the bank several times for me while I was posted at Fermilab. Thanks to our Systems Administrator, Michael Bryant, whose expertise helped create a seamless work environment in the lab.

I sincerely thank my physics teachers: Mr. B. Govinda Rao and Mr. S. Ramesh Babu at St. Joseph's English School, Kurnool, India; Dr. K. Ramakrishna and Mr. H. N. Ranganatha Rao at Bapatla Engineering College, Bapatla, India – it was these teachers that watered the seedling of my penchant for physics, which my mother had planted in my mind. Thanks are also due to Dr. Donald T. Haynie, my advisor

for Master of Science in Biomedical Engineering at Louisiana Tech University, whose background in Biophysics continued to kindle my interest in physics.

I sincerely thank all staff at LaTech that made my stay here a pleasurable one. Requiring particular mention are the Director of the International Student Office, Mr. Daniel Erickson, and the Coordinator of the International Student Office, Ms. Bijoya Chakraborty, who had helped me through my journey as an international student in the U.S.A. and helped me find a second home in Ruston. I earnestly thank the Associate Dean for Graduate Research, Dr. Bala Ramachandran, for his timely guidance and support at many instances when I needed it. It is also appropriate to remember and thank my previous research and academic advisors at LaTech, namely Drs. Michael McShane, Donald Haynie, Steve Jones, and Hisham Heghab. Mere thanks are not enough to appreciate the support that my numerous relatives and friends at Louisiana Tech and outside had given to me during this phase of my life. Particular mention is needed for some of them at LaTech: Sekhar Ravi, Venu Madhav Kotipalli, Koutilya Buchapudi, Surya Mangipudi, Krishna Karthik Koilada, Sri Krishna Chaitanya Kasinadhuni, Bharat Karumuri, Kiran Kumar Katkuri, and Sukeerth Challangundla. I also thank the Association of Indian Students at Louisiana Tech and the Indian community in Ruston for their part in making me feel at home here in Ruston and at Louisiana Tech University.

Most importantly, I thank the Almighty for giving me the great gift of Life, for filling in my mind Eternal support, courage, encouragement, and hope, and for creating opportunities all through my life even though I fell back several times during the course of my Life.

CHAPTER 1

INTRODUCTION

The objective of this research is to study how dijet azimuthal decorrelations vary with jet transverse momentum, p_T , and jet rapidity, y , in proton-antiproton ($p\bar{p}$) collision events occurring at a center of mass energy $\sqrt{s} = 1.96$ TeV.

In a high-energy collision involving particles such as protons and antiprotons, collimated sprays of multiple particles, called “jets”, may be produced. Study of radiative processes allows to test predictions of perturbative QCD and to search for phenomena beyond the Standard Model. One way of understanding these radiative effects better is by studying the angular distributions of the two jets with the highest transverse momenta, or the two “leading jets”. In the situation where such collisions produce exactly two jets with equal transverse momentum, the azimuthal angles of the two jets differ by a value of $\Delta\phi = \pi$ radians as they go in exactly opposite directions in the azimuthal plane. However, the azimuthal angular distribution varies due to radiative effects. Thus, the dijet azimuthal decorrelation shall be a single observable that may be used to estimate the transition between soft and hard QCD processes without requiring additional jet reconstruction.

Previous studies such as [1] have studied the angular distribution of inclusive dijet production in the central rapidity region only. The current study covers a

wider range of jet transverse momenta ($p_T \approx 90 - 450 \text{ GeV}$) and a wide range of jet rapidities ($|y| \leq 2.5$) through reliable statistics obtained by culling through more than forty million collision events. Such a vast study not only provides significantly useful information about the dijet azimuthal decorrelations but also paves way to similar analyses with larger amounts of collision data obtained at the Fermi National Accelerator Laboratory (FNAL, or Fermilab) where this study was conducted, and also at the Conseil Européen pour la Recherche Nucléaire (CERN, or European Organization for Nuclear Research).

The documentation of this research includes a modest introduction to particle physics and outlines the setup of the collision experiment being conducted inside the Tevatron Collider at Fermilab and the data taking at the laboratory's D \emptyset detector, identifying the ranges of transverse momenta where particular triggers are fired during the collision, and a triple differential study of p_T , y , and $\Delta\phi$. Furthermore, next-to-leading-order (NLO) calculations in perturbative QCD are compared to the experimental data.

CHAPTER 2

PHENOMENOLOGY

From the times of Kanāda in India or Democritus in Greece, both of whom predicted a few millennia ago that all matter is composed of smaller elements or particles, it is a long journey of discovery with thanks due to the advancements in physics, chemistry, optics, electronics, electromagnetics, mechanics, and the likes in science, technology, and engineering. This chapter shall provide the relevant background information to understand the history and development of particle physics while introducing the concepts necessary to understand the theory behind the proton-antiproton collision experiment that provides the data for the current research.

2.1 The Standard Model

The field of particle physics is based entirely on what is called the “Standard Model”, which enlists all particles that theory has predicted so far. Matter, as we know it, constitutes quarks and leptons, which are together termed “fermions”. The Standard Model lists six different flavors of quarks, three different flavors of leptons and corresponding neutrinos for each lepton flavor, and the force carrier particles called the bosons, as shown in Figure 2.1. While the Standard Model was proposed and standardized in the late 1970s [2], the three particles found after that, *i.e.* bottom quark (1977), top quark (1995), and τ neutrino (2000), corroborated the Standard

Model. This set of six quarks, three leptons and three corresponding neutrinos (and the antiparticles thereof), along with the gauge bosons through which these particles interact are considered the fundamental elementary particles as known today. Indications to the discovery of the Higgs boson have appeared in the most recent data from the CERN's Large Hadron Collider [3]. This set of particles and their interactions are called the “Standard” Model because it successfully describes all known matter and its structure and interactions and this model has not been refuted by any statistically significant results [2].

Quarks	2.4 MeV $\frac{2}{3}$ $\frac{1}{2}$ up u	1.27 GeV $\frac{2}{3}$ $\frac{1}{2}$ charm c	171.2 GeV $\frac{2}{3}$ $\frac{1}{2}$ top t	0 0 1 photon γ
	4.8 MeV $-\frac{1}{3}$ $\frac{1}{2}$ down d	104 MeV $-\frac{1}{3}$ $\frac{1}{2}$ strange s	4.2 GeV $-\frac{1}{3}$ $\frac{1}{2}$ bottom b	0 0 1 gluon g
				? 0 0 Higgs field H
Leptons	<2.2 eV 0 $\frac{1}{2}$ electron neutrino νe	<0.17 MeV 0 $\frac{1}{2}$ muon neutrino νμ	<15.5 MeV 0 $\frac{1}{2}$ tau neutrino ντ	91.2 GeV 0 1 weak force Z
	0.511 MeV -1 $\frac{1}{2}$ electron e	105.7 MeV -1 $\frac{1}{2}$ muon μ	1.777 GeV -1 $\frac{1}{2}$ tau τ	80.4 GeV +1 1 weak force W⁺
				Bosons (Forces)

Figure 2.1: The Standard Model of Physics [4]

A quark is believed to be a zero-dimensional particle that cannot exist by itself, and has to combine with one or two more quarks to form “hadrons”, namely a meson (a quark and antiquark pair) or a baryon (three quarks or antiquarks) respectively. On the other hand, leptons are independent particles by themselves without any known substructures. The various flavors of quarks and leptons differ in their properties such as mass and charge, while the force-carrier particles called the (gauge) bosons also differ in spin from the quarks and leptons; the left side column in each box in Figure 2.1 lists these properties (in that order). While all fermions are spin- $\frac{1}{2}$ particles, the bosons are all spin-1 particles. All the quarks and leptons have their corresponding antiparticles such that the mass and spin quantum number are the same but the charge reverses its polarity.

Each of the bosons mediates a kind of force field. The photons are the carriers of the electromagnetic force and the gluons are the mediators of the strong force, while the Z and W bosons mediate the weak force. The Higgs boson is responsible for the Higgs field which gives mass to particles that interact with it. It may also be noted that the Standard Model does not account for gravity.

2.2 Quantum Chromodynamics

The particle physics scene changed a lot since the 1960s as has been outlined earlier, as the decade 1960–’70 saw the advent of particle collision experiments in the giga-electronvolt (GeV) ranges. Experiments at the Stanford Linear Accelerator (SLAC) Laboratory in this decade proved that hadronic particles had substructures, and the parton model proposed during this decade by Richard Feynman and others

explained the interactions among these substructures constituting “partons” (quarks or gluons), while the quark model proposed by Gell-Mann and others helped provide a rational basis to hadronic spectroscopy [5].

Quarks, and the “force carrier particles” called gluons that interact with quarks, anti-quarks, and gluons themselves, are defined to have a “color charge”, which is of three flavors, called “red”, “green”, or “blue”. While individual quarks or gluons have color charge, hadrons are “colorless” or “white”. Quantum Chromodynamics (QCD) is a non-Abelian gauge theory that describes hadronic interactions as the interactions of quarks and gluons at small distances [6]. The QCD theory proposes two phenomena that play a major role in understanding partons and the interactions of partons with strong force, namely, color confinement and asymptotic freedom. Color confinement proposes that particles with color charge cannot be isolated, and consequently no free quarks are thus far directly observable. Confinement is thus the basis for the formation of hadrons. Colored partons emerging from a high-energy interaction undergo “fragmentation” (radiation of gluons, and splitting of gluons into quark-antiquark pairs) and “hadronization” (formation of hadrons). It also follows that no fraction of the fundamental electric charge e can be observed directly and only integral multiples of the fundamental charge can be found in nature. Asymptotic freedom refers to the asymptotic nature of freely moving partons: the interactions between partons are stronger when they are separated by larger distances in length and/or when the energy scales are smaller. This phenomenon keeps quarks and gluons within a hadron bound to each other so strongly that unbinding them requires large energy. (Asymptotic freedom, discovered in 1973, also awarded its discoverers – David

Gross, Frank Wilczek, and David Politzer – a Nobel Prize in Physics for the year 2004. Color confinement is yet to be analytically proven.) These two phenomena of QCD are instrumental in understanding particle collision experiments such as calculating the cross section of interactions [6].

Since partons interact weakly at high energies, perturbation theory may be used to compute the cross sections of deep inelastic processes involving partons. Perturbative QCD (pQCD), supported by experiment, eventually developed into a formal theory to describe high-energy, large-momentum transfer cross sections [5]. It may be noted that confinement is not a perturbative prediction while asymptotic freedom is. Thus, non-perturbative QCD methods such as lattice QCD are used to understand confinement and other non-perturbative phenomena such as quark-gluon plasma formation [5].

Terms in perturbative expansion increase in exponents by an order of the strong coupling constant, α_s (*cf.* Section 2.2.1). The first non-trivial term of the perturbative expansion of the scattering cross section is called the “Leading Order” (LO) term, the next higher order term (increased by a multiplicative scale of α_s compared to the LO term) is called “Next-to-Leading Order” (NLO) term, the next term in the expansion (increased by a multiplicative scale of α_s compared to the NLO term) is called “Next-to-Next-to-Leading Order” (NNLO) term and so on. The coefficients of these terms are predicted by theory while the strong coupling constant is determined from experiment. The cross section σ is thus expanded perturbatively as

$$\sigma = C_0 + C_1 \alpha_s + C_2 \alpha_s^2 + C_3 \alpha_s^3 + \dots \quad (2.1)$$

These interactions of pQCD are represented in two-dimensional diagrams similar to the electromagnetic interactions in Quantum Electrodynamics (QED) theory, and are called Feynman diagrams, after Richard Feynman who developed the parton model and laid down rules for these diagrams [7]. Quarks are represented as straight lines and gluons are represented as curled lines in Feynman diagrams for QCD theory. It is a feature of non-Abelian gauge theories that gluons can couple to any color-charged particles and thus can couple to themselves or to quarks. Each vertex in these diagrams corresponds to a factor of $\sqrt{\alpha_s}$. Leading order terms are tree-level diagrams with no internal loops while higher order terms may be loop diagrams. Time flow is indicated by the left-to-right direction, and thus a vertically-directed arrow indicates that the intermediate parton in the particular QCD interaction does not travel in time. In $qq \rightarrow qq$ interaction, both horizontal and vertical interactions are added and the interference as a product of these two interactions is also added and ultimately squared to compute the cross section. The initial states always annihilate each other in a horizontally represented diagram and are thus a parton and its corresponding anti-parton only; the initial and corresponding final partons are definitely the same in a vertically represented Feynman diagram. Figure 2.2 shows examples of Feynman diagrams in 2-jet production.

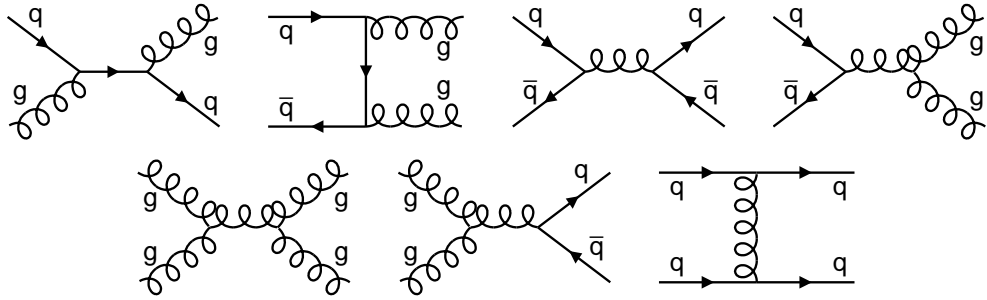


Figure 2.2: Feynman diagrams for 2-jet production

2.2.1 Strong Coupling Constant

The strong coupling constant specifies the strength of strong interactions. The value of α_s decreases for high-energy or short-distance interactions due to asymptotic freedom in hard/deep-inelastic processes. A perturbative expansion is employed to calculate the QCD cross section. While calculating the cross section, divergence must be avoided in loop graphs; the modified minimal subtraction scheme ($\overline{\text{MS}}$) [8] of renormalization is commonly employed for this purpose. Renormalization dependence at NLO introduces the mass scale μ_R . Perturbation theory is valid if μ_R is chosen of the order of a process-relevant energy scale. The coefficients of terms beyond LO in the perturbative expansion depend on the renormalization scheme and the renormalization scale [9]. The running coupling in 1-loop approximation is given by the following expression of α_s at a specific energy scale Q^2 in $\overline{\text{MS}}$ scheme:

$$\alpha_s(Q^2) = \frac{1}{\beta_0 \ln(Q^2/\Lambda_{\overline{\text{MS}}}^2)}, \quad (2.2)$$

where $\Lambda = \frac{\mu}{e^{1/(2\beta_0\alpha_s(\mu^2))}}$, $\beta_0 = \frac{33 - 2N_f}{12\pi}$, and N_f is the number of active quark flavors at the energy scale Q [9].

2.2.2 Parton Distribution Functions

Parton distribution functions (PDFs, sometimes termed “parton density functions”) indicate the probability density of finding partons in a hadron, given as a function of the fraction x of hadronic momentum carried by the parton and the factorization scale μ_F used to remove divergences due to soft radiation collinear to the beam in the perturbative coefficients to all orders. As the QCD bound state renders pQCD inapplicable for long-distance parton interactions, PDFs are used to parametrize the missing knowledge of the interactions of partons inside the hadrons. The evolution of a single PDF with μ_F requires knowing all the parton distributions over the entire range of momentum fractions. PDFs are process-independent and are useful as inputs to any hadronic processes for perturbative calculations. It is necessary to know the PDFs in order to describe hard processes with one or two hadrons in the initial state [10]. Figure 2.3 shows the PDFs obtained using “the most recent collider data from deep-inelastic scattering, vector boson production, and single-inclusive jet production” [11].

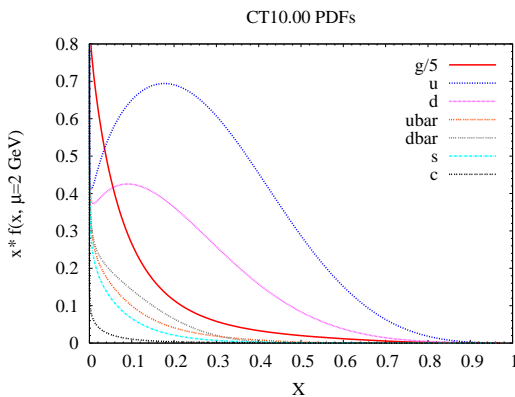


Figure 2.3: PDFs for various quark flavors and a gluon [11]

2.3 Introduction to Jets

A jet may generally be loosely defined as “a collection of collimated particles” [12]. Formation of jets is inevitable in a particle collision experiment involving hadrons, as is explained by the quark confinement phenomenon of the QCD theory. The actual definition of a jet is provided by a jet algorithm. Jet studies help assess more information about the particles involved before and after the collisions and about interactions which can be tested through pQCD. Thus, jet studies play a significant role in furthering our knowledge of the particulate world, confirming the existence of known particles, and estimating the presence of new particles and their substructures. In case of highly energetic jets, the effects of fragmentation and hadronization are small and thus the particle-jet four-vectors are closely related to the parton-jet four-vectors. In other words, the particles jets resemble the footprints of the partons emerging from high-energy interactions of hadrons.

Study of radiative processes are crucial for precision measurements and when searching for phenomena defining new physics; angular distribution of the jets involved is a simple way to study these processes [1]. Such QCD studies require particles, partons, and/or energy deposition on calorimeter towers (*cf.* Section 3.2.3) or MC simulations thereof to first be defined as jets. A few measurable variables ought to be defined before jets can be defined, to facilitate a better understanding of the jet definition:

The four-momentum of a particle is defined as the momentum of a particle in four-dimension space-time, using energy E , and the momentum $\vec{p} = (\vec{p}_x, \vec{p}_y, \vec{p}_z)$. However, a more convenient way of representing this four-momentum is by using the

variables transverse momentum (p_T), rapidity (y), azimuthal angle (ϕ), and energy (E) of the particle [14].

The transverse momentum vector \vec{p}_T is defined as the sine component of the momentum vector, and thus has a magnitude of

$$p_T = p \sin \theta, \quad (2.3)$$

where θ is the polar angle with respect to the beam axis (Figure 3.3).

Rapidity is defined as

$$y = \frac{1}{2} \ln \left(\frac{E + p_z}{E - p_z} \right), \quad (2.4)$$

where E is the energy of the particle and p_z is the magnitude of the momentum component in z -direction. An alternate definition of rapidity is

$$y = \frac{1}{2} \ln \left(\frac{1 + \beta \cos \theta}{1 - \beta \cos \theta} \right), \quad (2.5)$$

where β is the relative velocity of the particle with respect to that of light, *i.e.*

$$\beta = \frac{v}{c} = \frac{|\vec{p}|}{E}. \quad (2.6)$$

Pseudorapidity η is defined as

$$\eta = \frac{1}{2} \ln \left(\frac{1 + \cos \theta}{1 - \cos \theta} \right) = -\ln \tan \frac{\theta}{2}. \quad (2.7)$$

This term is referred to as pseudo-rapidity because this would be the rapidity of a massless particle; it may be noted that a massless particle must travel at a velocity equal to that of light and thus $\beta = 1$.

The DØ Run II Jet Cone Algorithm [15] is an iterative seed-based cone algorithm that defines jets with a cone of radius $\mathcal{R}_{cone} = 0.7$ in the $y\text{-}\phi$ plane. Spatial distance is defined by $\Delta\mathcal{R} = \sqrt{(\Delta y)^2 + (\Delta\phi)^2}$ in the space of rapidity, y , and azimuthal angle ϕ . The quantities Δy and $\Delta\phi$ are defined as the absolute difference of individual jet rapidities and that of azimuthal angles of the jets respectively.

All particles, namely calorimeter energy deposits from the $p\bar{p}$ collision, stable particles in the particle level Monte Carlo simulations, and partons in pQCD, are considered as seeds for jet reconstruction in the iterative jet cone algorithm. In a first pass, for each seed, the cone axis is set as the direction of the particle and a cone is drawn around the axis. All particles within the radius $\Delta\mathcal{R} \leq \mathcal{R}_{cone}$ are added to the proto-jet, and the four-vector for the proto-jet is determined subsequently. This procedure is repeated until a stable solution, for which the proto-jet axis is the same as the cone axis, is found. Adding midpoints between pairs of proto-jets from the first pass as additional seeds ensures that the algorithm is infrared-safe, *i.e.* the procedure is insensitive to small amounts of radiation added between the jets. Infrared safety is necessary to be able to use the algorithm to make pQCD predictions.

Once all stable solutions are obtained, identical solutions are removed from the list and overlapping jets are addressed. In order to remove overlaps, jets are first sorted in descending order of transverse energies. For every pair of proto-jets, if the energies of the two proto-jets overlap by more than 50 %, *i.e.* $f = \frac{p_T^{overlap}}{p_T^{min}} > 0.5$ (where p_T^{min} represents the smaller jet transverse momentum of the two proto-jets), the two proto-jets are merged; if $f < 0.5$, the proto-jets are split and all the particles in the overlapping region are assigned to the closest proto-jet. After each iteration of

split-and-merge, the proto-jets are sorted in descending order of E_T again so that jets of maximal p_T are preferentially reconstructed. Only the proto-jets that pass through multiple iterations of the split-and-merge procedure are ultimately defined as jets.

2.4 Dijet Azimuthal Decorrelations

In the absence of radiative effects, pQCD predicts dijets are produced with equal p_T and jet vectors in the azimuthal plane are correlated. QCD radiation decorrelates the dijet system, thereby increasing the azimuthal angular separation $\Delta\phi = |\phi_{jet1} - \phi_{jet2}|$ of the two jets. Therefore, the difference of $\Delta\phi$ to π is a measure of the dijet azimuthal decorrelations. A decrease in $\Delta\phi$ to a value between π and $\frac{2\pi}{3}$ indicates a third hard jet production, and a decrease to a value further lower indicates that more additional jets are being produced as illustrated in the Figure 2.4.

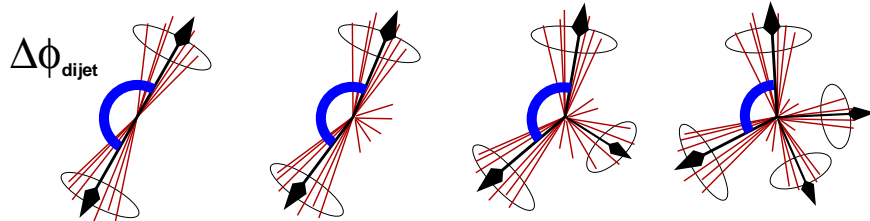


Figure 2.4: Dijet azimuthal angular decorrelation in radiative processes [16]

Thus, a single observable based on $\Delta\phi$, which is sensitive to production of three or more jets, may be used to estimate the transition between hard and soft QCD processes without requiring additional jet reconstruction [1].

2.5 Previous Measurements of Dijet Azimuthal Decorrelations

The angular distribution of inclusive jet production was studied earlier [1] for the central rapidities ($|y_{jet}| < 0.5$). This analysis, which was published as the first QCD result from the DØ Collaboration in Run II of the Fermilab Tevatron Collider, was performed with an inclusive dijet sample corresponding to an integrated luminosity of 150 pb^{-1} , requiring that the transverse momentum of the first leading jet is at least 75 GeV and that of the second leading jet is at least 40 GeV .

Figure 2.5 shows the results obtained through this analysis. It may be noticed that there is a change in the shape for the curves plotted by the observable as the transverse momentum increases. However, this dependence on transverse momentum was not explicitly measured as a part of this analysis.

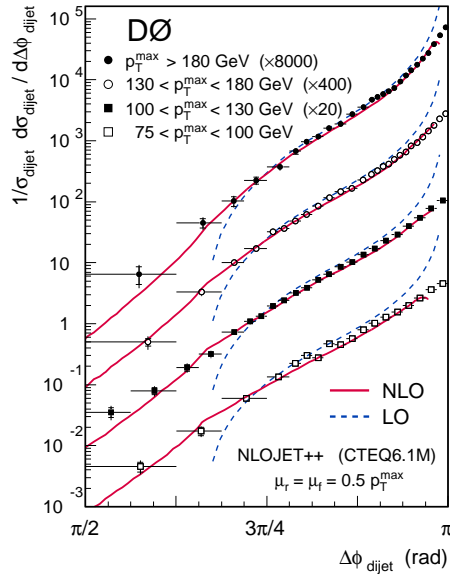


Figure 2.5: Angular distributions for LO/NLO pQCD predictions overlaid on the experimental data [1]

2.6 Phase Space Definition

The current analysis presented in this dissertation is based on an inclusive dijet event sample with the p_T of the second leading jet, $p_{T_2} > 30 \text{ GeV}$, and spans across rapidities up to $|y_{jet}| = 2.5$. However, the actual rapidity limits are set through the variables y^* and y^{boost} defined as below:

$$y^* = \frac{|y_1 - y_2|}{2}, \quad (2.8)$$

$$y^{boost} = \frac{y_1 + y_2}{2}. \quad (2.9)$$

These definitions lead to the observation that the accessible detector rapidity, $y^{detector}$, is limited by the sum of the maximum values of y^* and y^{boost} . In other words, the maximum value of $y^{detector}$ is given as

$$y_{max}^{detector} = y_{max}^* + y_{max}^{boost}. \quad (2.10)$$

For this analysis, y^* is divided into three regions ranging from $0.0 < y^* < 0.5$, $0.5 < y^* < 1.0$, and $1.0 < y^* < 2.0$ and y^{boost} is limited to $y^{boost} < 0.5$, thereby limiting the maximum range of rapidities to $|y| < 2.5$.

While the observable in the previous work was measured as a function of p_T , the observable in the present work is measured as a function of H_T , defined as the sum of all jet transverse momenta where the transverse momenta of individual jets are at least 30 GeV and the absolute difference of individual jet rapidity and boost rapidity is less than the maximum value of y^* of 2.0 , mathematically expressed as:

$$H_T = \sum_{i \in \mathbb{C}} p_{T_i}, \quad (2.11)$$

where the index i runs over all jets in the set \mathbb{C} defined as

$$\mathbb{C} = \left\{ \begin{array}{l} \forall \text{jets } i : 1 \leq i \leq n_{jets}; \\ p_{T_i} > 30 \text{ GeV}; \\ |y_i - y^{boost}| < y_{max}^* = 2.0 \end{array} \right\}. \quad (2.12)$$

The transverse momentum of the leading jet, p_{T_1} , is required to be greater than $\frac{H_T}{3}$.

The observable $R_{\Delta\phi}$ used in the current analysis is thus defined as a triple differential variable in H_T , y^* , and $\Delta\phi_{max}$. It is measured in various y^* regions (0.0–0.5, 0.5–1.0, and 1.0–2.0) corresponding to different rapidities in the dijet center-of-mass frame, and for different $\Delta\phi_{max}$ values of $\frac{7}{8}\pi$, $\frac{5}{6}\pi$, or $\frac{3}{4}\pi$. Thus,

$$R_{\Delta\phi}(H_T, y^*, \Delta\phi) = \frac{\frac{\partial^2 \sigma_{dijet}(\Delta\phi < \Delta\phi_{max})}{\partial H_T \partial y^*}}{\frac{\partial^2 \sigma_{dijet}(\text{inclusive})}{\partial H_T \partial y^*}}. \quad (2.13)$$

2.7 Theory Predictions

The pQCD prediction is calculated at NLO as the ratio of an inclusive three-jet cross section and the inclusive dijet cross section both evaluated at their respective NLO; most of the dependences on the PDFs for the numerator and denominator cancel in the ratio. fastNLO [17] program based on the simulation software NLOJET++ [18], [19] in the $\overline{\text{MS}}$ scheme [8] is used to compute the NLO pQCD results. The pQCD results mean that the perturbative calculations produce predictions for parton-level jets. These results do not include the non-perturbative effects such as hadronization

(the process in which partons form hadrons) and underlying event (the contribution from interactions of additional partons from the initial-state hadrons). Full theory predictions include the pQCD predictions to which the correction factors for non-perturbative effects are applied.

In order to bring the NLO pQCD calculation at the parton-level to the particle-level with underlying event, non-perturbative corrections are determined and applied to the NLO pQCD predictions. The non-perturbative corrections are calculated using Monte Carlo simulations by the PYTHIA 6.4 generator with different tunes, namely AMBT1 and DW which differ in the underlying event and the parton shower model [16]. The PYTHIA tune DW [16] was tuned to a Run II D \emptyset measurement of dijet azimuthal decorrelations, whereas the PYTHIA tune AMBT1 [20] was derived by the ATLAS collaboration and includes LHC data measured at a center-of-mass energy $\sqrt{s} = 7 \text{ TeV}$. Three event samples, namely parton shower level without underlying event, hadron level with and without underlying event, are generated for each of these tunes with 320 million events over the kinematic range $30 < \hat{p}_T < 680 \text{ GeV}$. The hadronization correction is obtained from the ratio of the observable on the parton-level (after the parton shower) and the particle-level (including all stable particles), both without underlying event. The underlying event correction is computed from the ratio of the observable computed at the particle-level with and without the underlying event. The product of hadronization corrections and the underlying event corrections provide the total non-perturbative corrections applicable to the NLO pQCD calculation. Correction factors are also found using the tune A (similar to tune DW with one half the statistics) and the tune S Global (similar to tune AMBT1

with one half the statistics) in addition to the tunes AMBT1 and DW; however, the final non-perturbative correction factors applied to the data are the average of those obtained using the PYTHIA tunes AMBT1 and DW.

Figure 2.6 shows the non-perturbative correction factors for hadronization correction, and Figure 2.7 shows the non-perturbative correction factors for the underlying event correction. The hadronization correction factors are typically 1–3 % and never deviate from unity by more than 6 %, while the underlying event correction factors are typically 2–4 % and never deviate from unity by more than 8 %. Figure 2.8 shows the total non-perturbative corrections from all the four tunes. The total non-perturbative correction factors are always small, typically 2–4 %, and never deviate from unity by more than 8 %.

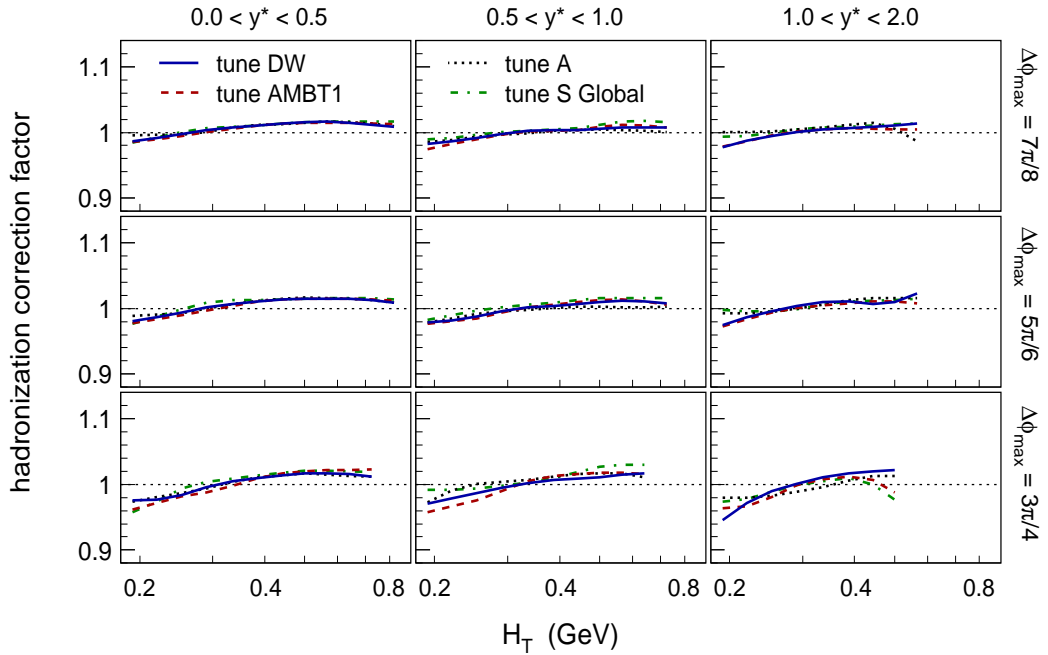
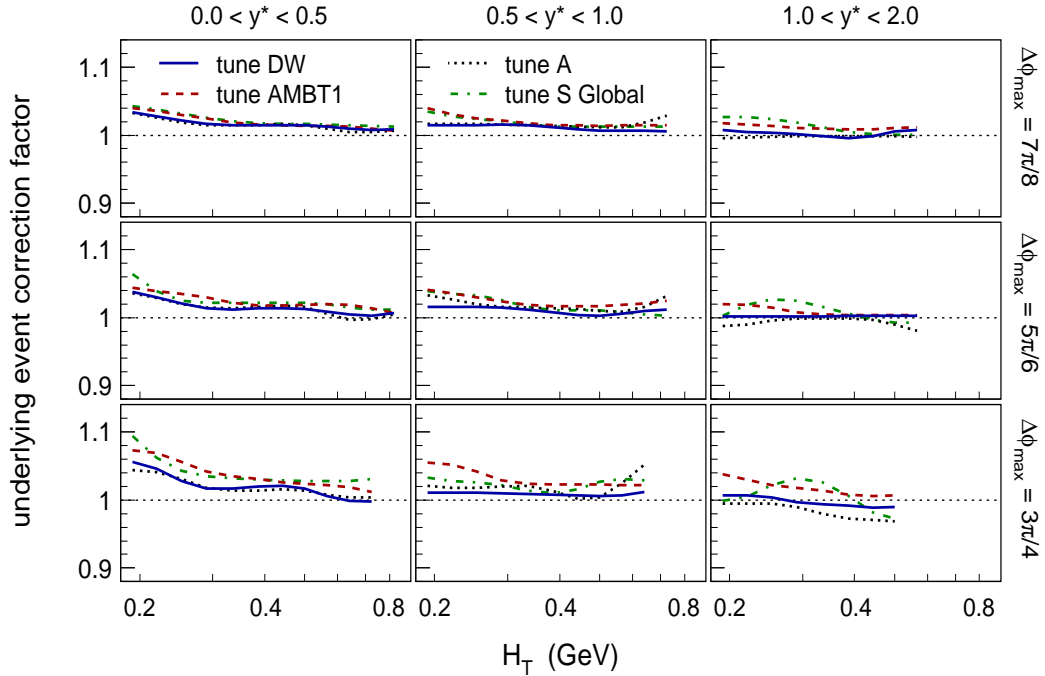
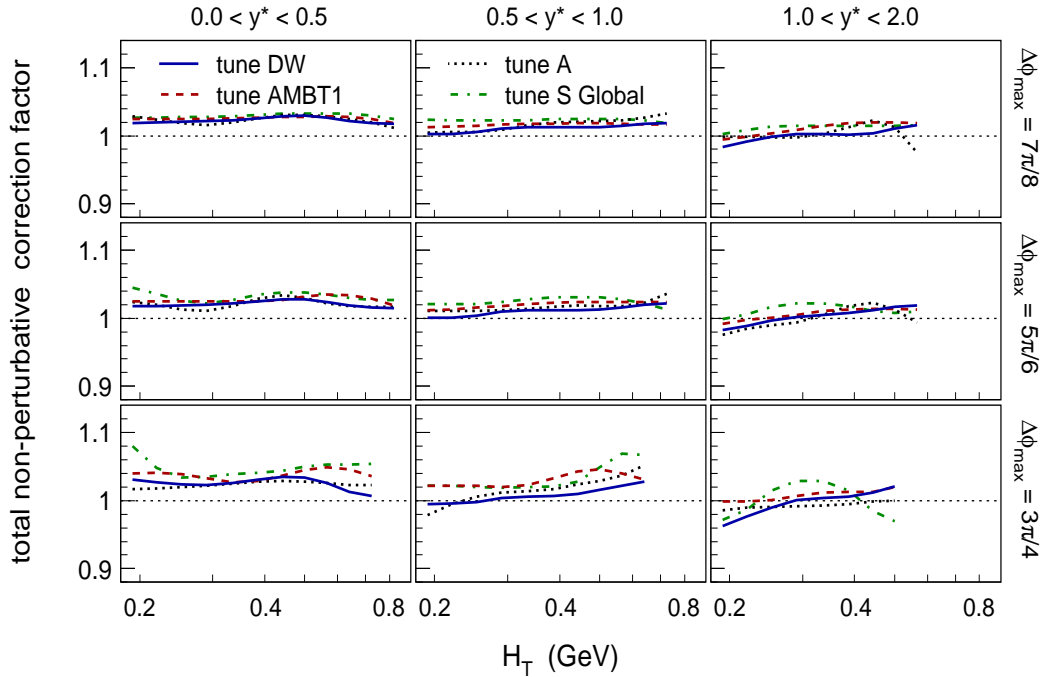


Figure 2.6: Hadronization corrections for $R_{\Delta\phi}$

Figure 2.7: Underlying event corrections for $R_{\Delta\phi}$ Figure 2.8: Total non-perturbative corrections for $R_{\Delta\phi}$

CHAPTER 3

EXPERIMENTAL SETUP

The Fermi National Accelerator Laboratory, also called “Fermilab”, is an accelerator facility run by the United States Department of Energy (USDoE). Its mission is “to advance the understanding of the fundamental nature of matter and energy” and to facilitate “basic research at the frontiers of high energy physics and related disciplines”. Since its establishment in 1967 as the National Accelerator Laboratory, Fermilab had witnessed several major discoveries including those of the bottom quark in 1977, the top quark in 1995, and the τ neutrino in 2000.

Fermilab conducts experiments in three domains – Energy Frontier, Intensity Frontier, and Cosmic Frontier – involving protons and antiprotons, neutrinos, muons, dark energy and dark matter. More projects such as Long Baseline Neutrino Experiment (LBNE), Mu2e, Project X, NO ν A, MicroBooNE, MICE, Dark Energy Survey, and Large Synoptic Survey Telescope (LSST) are proposed for the future.

3.1 The Tevatron Collider

The Fermilab Tevatron Collider is the world’s most powerful proton-antiproton collider.¹ In the past, the Fermilab housed fixed-target particle physics experiments

¹CERN’s Large Hadron Collider (LHC) is the world’s most powerful hadron-hadron collider where proton-proton collision experiments are conducted.

with particle beams colliding stationary targets. The advent of the Tevatron in 1985 brought forth counter-rotating, colliding particle beam experiments at the Collider Detector at Fermilab (CDF); the DØ detector was installed in 1992. Protons and antiprotons are accelerated to 99.9999954 % of the speed of light as they are passed through a four-mile circumference, bending the particle beams into a circular path with the help of more than a thousand superconducting magnets operating at -450°F placed outside the vacuum pipe along the beam's path. The proton and antiproton beams, traveling at 0.98 tera electron-volt (or approximately 1 TeV, and hence the name “Tevatron”) of energy in opposite directions, are collided to generate particle collisions at a center of mass energy of 1.96 TeV, at two detectors in the beam path, namely the CDF and the DØ detectors. Protons are created by removal of electrons from negatively charged hydrogen (H^-) ions using a carbon foil after accelerating them to 70 % of the speed of light in a linear accelerator (“linac”). Antiprotons are created by directing a portion of these protons onto a nickel target. Both these beams are prepared for collisions by accumulating, cooling, and accelerating the particles appropriately using booster, recycler, and main injector before sending the particles into the Tevatron. Figure 3.1 shows the Fermilab’s accelerator chain that depicts the particle collision experimental setup at Fermilab.

FERMILAB'S ACCELERATOR CHAIN

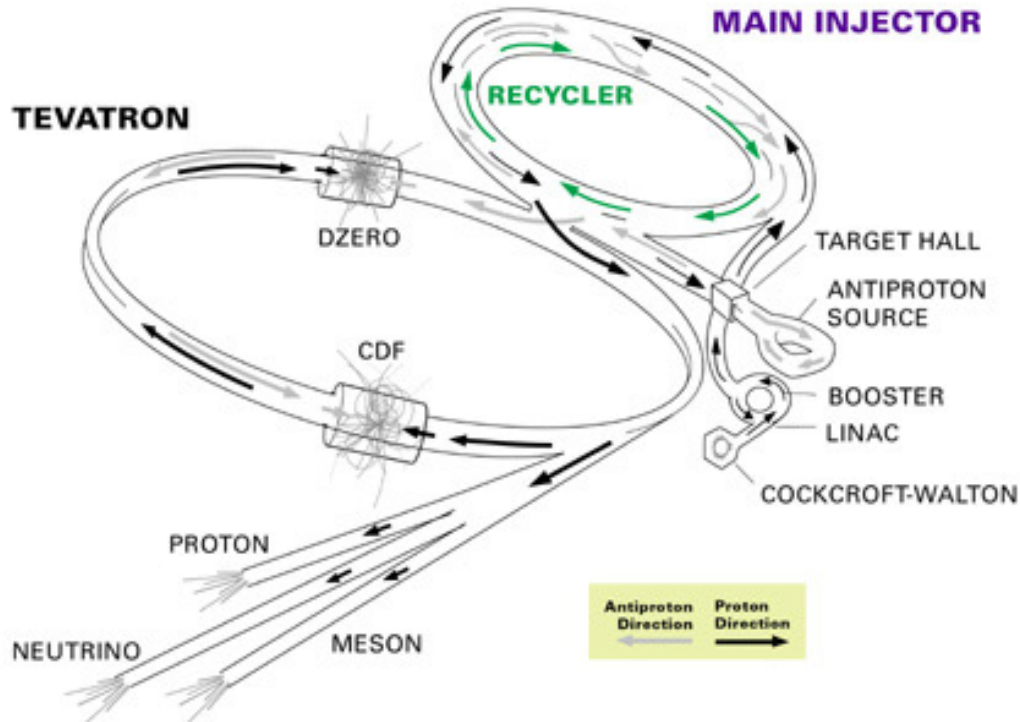


Figure 3.1: Fermilab's accelerator chain

Hydrogen atoms are fed to a magnetron source to produce H^- ions, which are sent to the Cockcroft-Walton generator where the particles achieve an energy of 750 keV. The H^- ions are then sent to the linac where the ions reach energies of 400 MeV. At this point, electrons are stripped off the H^- ions in the booster and the particle beam, a combination of particles flowing in through six consequent cycles from the linac, is accelerated to 8 GeV before it is sent to the main injector. The main injector accelerates the proton beams to 120 GeV for collision experiments and certain neutrino experiments such as the NuMI. The 120-GeV proton beam is sent to the \bar{p} source to generate antiproton beams for collision. During the shot setup

phase of the main injector, beams are accelerated for injection into the Tevatron for eventual collision. Seven bunches of protons from the booster are collected each time and coalesced into one bunch after accelerating to 150 GeV during this phase; this process of acceleration and coalescing is done 36 times so as to have 36 bunches of protons. Four bunches of antiprotons, which have been stored in an accumulator after production, are also accelerated to 150 GeV for 9 times, thus preparing 36 bunches of antiprotons for collision. 36 exclusive bunches of protons and antiprotons form a “store” that typically lasts about 24 hours. The Tevatron accelerates each of the beams to an energy of 980 GeV, taking the center-of-mass energy of the colliding beams to $\sqrt{s} = 1.96 \text{ TeV}$ (in ‘Run II’). Collisions occur at two positions in the Tevatron, at the CDF and the DØ detectors.

3.2 The DØ Detector

The DØ detector, running since 1992 and upgraded for ‘Run II’ by 2001, witnesses an average of 1.7 million collisions per second, of which about fifty interesting events per second are recorded for further analyses. Figure 3.2 depicts the cross section of the DØ detector upgraded for Run II while identifying components of the calorimetry and tracking systems [13].

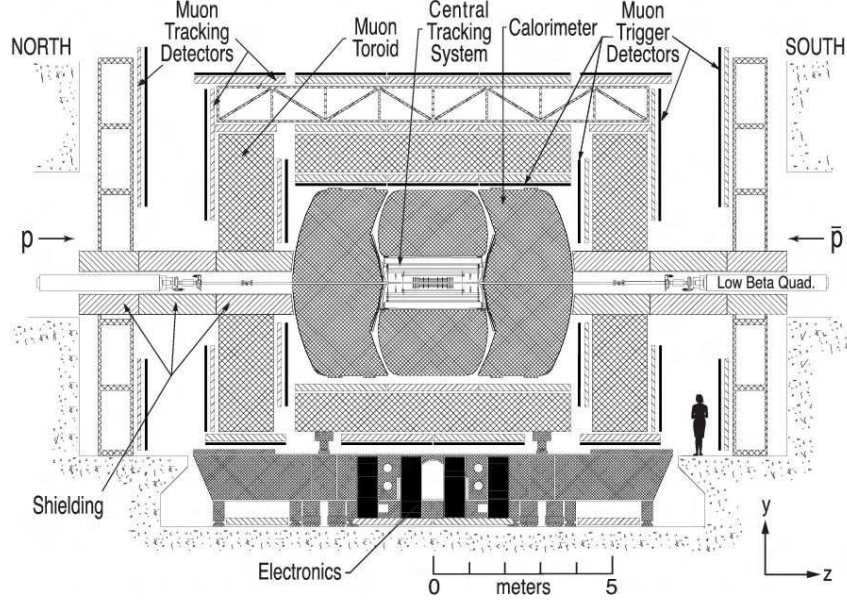


Figure 3.2: The Run II DØ detector [13]

The direction in which the proton beam travels is chosen to be the z -axis while the x -axis is the direction that points to the center of the Tevatron Collider. Figure 3.3 shows the right-handed coordinate system of the detector in three dimensions along with the polar angle θ made by a scattered particle jet with respect to the beam direction (z -axis), and the azimuthal angle, ϕ , in the x - y plane. Not shown in the figure is the polar distance component r , which is the distance perpendicular to the beam pipe.

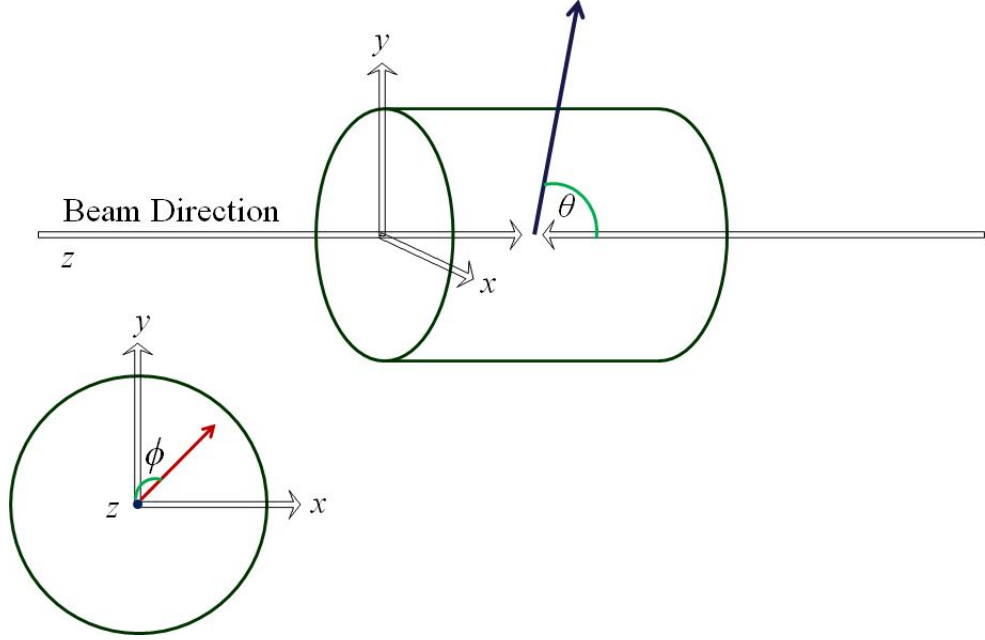


Figure 3.3: The coordinate system for the DØ detector

Reference [13] describes the DØ detector with particular emphasis on the components which were upgraded for the Run II of the detector. The following subsections introduce each of the detector’s subsystems briefly.

3.2.1 Tracking System

A good tracking system is essential to measure momentum and position of charged particles. The central tracking system of the DØ detector (Figure 3.4) comprises of the silicon microstrip tracker (SMT) and the central fiber tracker (CFT) surrounded by a solenoid. These two detectors can identify the primary interaction vertex within the beam-line with a $35 \mu\text{m}$ resolution, thereby helping precisely measure lepton p_T , jet E_T , and missing transverse energy (\cancel{E}_T).

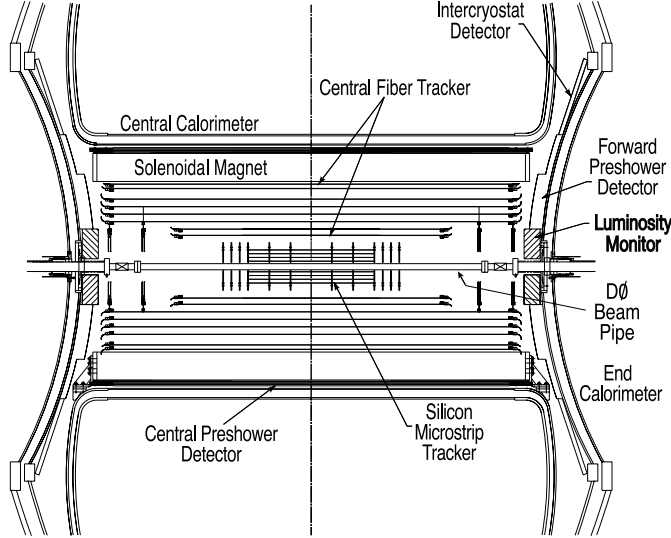


Figure 3.4: Central tracking system of the DØ detector [13]

The SMT provides signal to the Level 2 and Level 3 triggers (*cf.* Section 3.2.6) and provides tracking and vertexing information through the full η coverage for the calorimeter and the muon systems. The CFT provides faster readout for Level 1 trigger, and the track information from the signals passed by the Level 1 trigger are sent to the Level 2 trigger, while the Level 3 trigger receives slower, digitized signal readout from the analog signals of the CFT in addition to the information available from the Level 1 and Level 2 triggers. The 2 T solenoid magnet, wound using superconducting Rutherford-type cables of Cu:NbTi strands with pure aluminum, maximizes momentum resolution, improves tracking pattern recognition, and provides a uniform magnetic field throughout the volume of the detector.

3.2.2 Preshower Detectors

The preshower detector is intended to identify protons and electrons and to reject background during triggering as well as during the offline reconstruction.

Spatial matching between tracks and calorimeter showers is improved as the preshower detectors act both as a calorimeter and as tracking detectors used to match tracks to the electromagnetic (EM) showers in the calorimeter. The readout of the preshower detector connects to the readout electronics of the Central Fiber Tracker (CFT). The preshower detector comprises of central (CPS) and forward (FPS) components. The CPS is made of three concentric cylinders between the solenoid and the central calorimeter (CC), and each layer is equipped with 2560 readout channels. The FPS is located on the faces of the end-cap calorimeters (EC), between the Inter-Cryostat Detector (ICD) and the luminosity monitors. Each FPS is composed of two layers, namely the minimum ionizing particle (MIP) layer and a shower layer separated by a lead-stainless steel absorber made of 48 wedge-shaped pieces. Particles are identified by their showers and the tracks they leave.

3.2.3 Calorimetry

A calorimeter measures the energy deposited as a particle passes through it, either by sampling the measurements at discrete intervals or by measuring the full energy. Transverse segmentation of the calorimeter helps identify the direction from which the particle entered, while longitudinal segmentation provides more information about the shape of the shower allowing particle identification. DØ uses as a sampling calorimeter designed to identify electrons, photons, and jets.

The DØ calorimeter (Figure 3.5) is composed of three detectors exclusively housed in their own cryostats, namely the central calorimeter (covering $|\eta| \lesssim 1.0$), and two end-cap calorimeters (EC north and south, or ECN and ECS, extending

coverage to $|\eta| \approx 4.0$). Uranium plates are placed in chambers filled with liquid argon inside each of the cryostats. The purity of liquid argon is critical for an accurate measurement by the calorimeter as electronegative contaminants such as oxygen can interact with electrons traversing the gaps and alter the energy measurement; 1 ppm impurity can result in a signal loss by 5 %. *In situ* measurement of liquid argon contamination sensitive to less than 1 ppm is thus performed through radioactive ^{241}Am (α source) and ^{106}Ru (β source) sources. A change in temperature also affects the signal and the temperature of the liquid argon is therefore constantly maintained at 90.7 ± 0.1 K. While the use of liquid argon allows segmentation of the detector and makes calibration easy, it also requires the use of individual cryostats which creates inaccessible areas in the instrumentation.

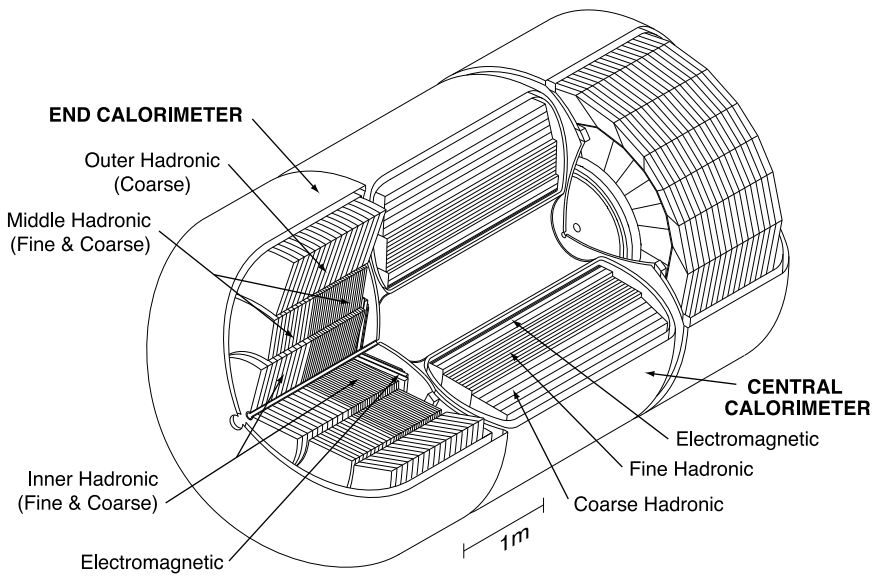


Figure 3.5: The DØ calorimeter in Run II [13]

Each detector region has an electromagnetic (EM) section, a fine and a coarse hadronic sections, spaced radially away from the interaction point. The EM section consists of absorber plates made of nearly 100% pure depleted uranium, with 3 mm-thick plates in the CC and 4 mm-thick plates in the EC regions; these plates are arranged in four layers of varying depth in CC and four different depth layers in EC. While the fine hadronic section consists of 6 mm-thick plates made out of uranium-niobium alloy, the coarse hadronic section has 46.5 mm-thick copper plates in the CC and stainless steel plates in the EC. The calorimeter comprises of towers $0.1 \times 0.1 \text{ in}^2$ in the region $|\eta| < 3.2$ and of towers $0.1 \times 0.1 \text{ in}^2$ in the region beyond, segmented in the η - ϕ space.

The DØ calorimeter has a total of 55,296 electronic readout channels with 47,032 of them corresponding to physical readout channel modules in the cryostats. The data from the detector are first sent to the charge preamplifiers on the cryostats and then to the baseline subtractor (BLS) boards and precision signals from the BLS boards are sent to the ADC cards and finally to the data acquisition system for decision-making by the Level 3 trigger (*cf.* Section 3.2.6), and signals passing the triggers are eventually stored. The readout chain showing preamplifiers, BLS boards and ADC cards is presented in Figure 3.6.

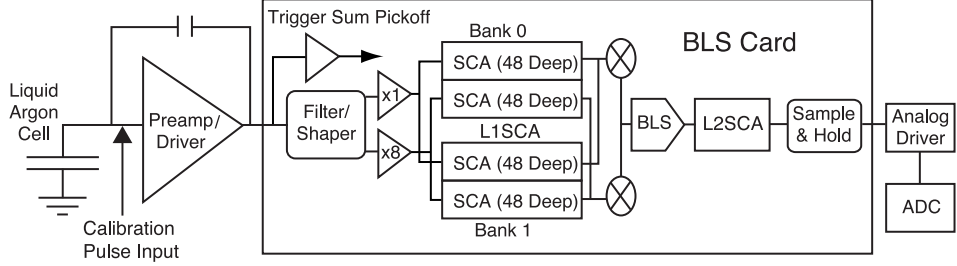


Figure 3.6: Readout chain of the DØ calorimeter [13]

The detector segmentation and η coverage is shown in Figure 3.7. The region $0.8 < |\eta| < 1.4$ is not completely covered and thus requires additional sampling layers. Single-cell structures called massless gaps are calorimeter readout cells in front of the first layer of uranium within the central and end cryostats. The region $1.1 < |\eta| < 1.4$ is covered by the inter-cryostat detector (ICD) comprising of scintillator sampling components attached to the exterior surface of the end-cryostats. 0.5 inch-thick scintillating tiles which are fit inside light-tight aluminum boxes cover an area of $\Delta\eta \times \Delta\phi \approx 0.3 \times 0.4$ with twelve sub-tiles of $\Delta\eta \times \Delta\phi \approx 0.1 \times 0.1$, and a half-tile in the south-end of the detector is deliberately removed due to cryogenic services for the solenoid. The ICD electronics are in a low-magnetic field region away from tiles, in a drawer system. Each ICD drawer comprises photomultiplier tube (PMT) electronics and preamplifiers for readout through six channels; three sections (north, east, west) of the ICD consists of 16 drawers each and the south end consists of 15 drawers with the one less drawer accounting for the missing half-tile, thus making ICD readout available through a total of 378 channels.

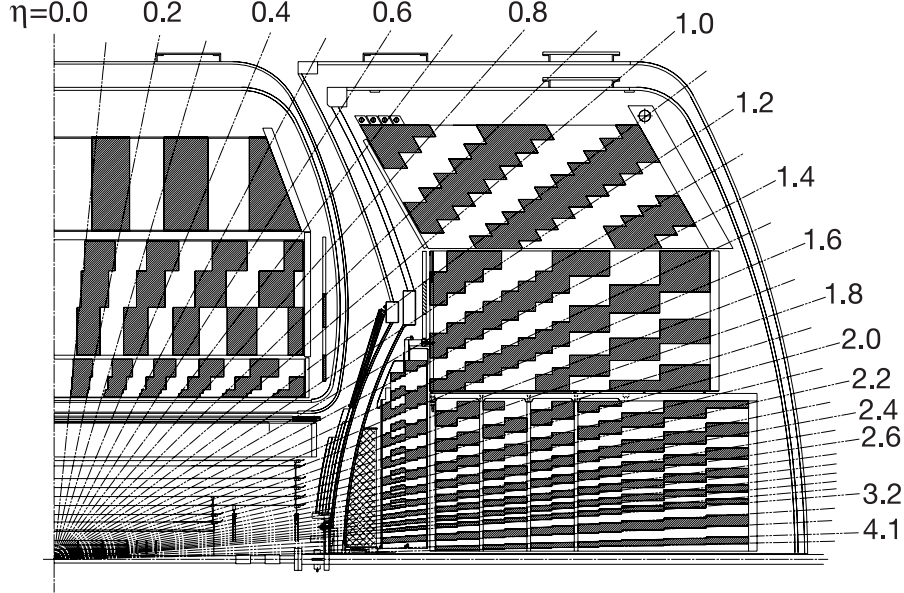


Figure 3.7: Schematic of a quadrant of the DØ calorimeters showing the the distribution of pseudorapidity [13]

3.2.4 Muon System

The muon system consists of a central and forward muon detectors along with a toroid magnet. While the central muon detector detects through the region $|\eta| \lesssim 1.0$. The forward muon detector covering through $|\eta| \approx 2.0$ has been added to the detector during the Run II phase. Scintillation counters are used for triggering and for rejecting the background events. The toroidal magnets are built in three sections to enable access to the detector's interior, with the center-bottom section providing a platform to the calorimeters and central tracking detectors. The central muon detector also contains drift chambers for precise coordinate measurements of muons. They are composed of one layer of rectangular proportional drift tubes (PDTs) inside the central toroid and two layers of PDTs outside it. Cosmic cap and bottom scintillation counters of the central muon detector help reject the background noise, and the $A\phi$ scintillation

counters help identify muons and reject out-of-time background scatter from the forward direction with the help of a linkage to the Tevatron clock to detect timing. The forward muon detector consists of end toroidal magnets, the mini drift tubes (MDTs) to extend the coverage to $|\eta| \approx 2.0$, and beam-pipe shielding. The MDTs are also arranged in three layers like the PDTs in the central muon detector, and are used in the forward section instead of PDTs because of their advantages such as shorter electron drift time and lesser-than-a-millimeter coordinate resolution. Muons with higher momentum are better resolved by the forward muon system, particularly in the range $1.6 \lesssim |\eta| \lesssim 2.0$. Sources of background affecting the muon system measurements include scattered fragments of protons and antiprotons interacting with the calorimeter or the beam-pipe (which affect the inner layer of the detectors), or due to these scattered fragments interacting with the Tevatron low-beta quadrupole magnets or due to halo interactions inside the tunnel (which affect the outer layers of the detectors). The background due to halo interactions, *i.e.* interactions of particles with the beam-pipe, and other sources is reduced by shielding of the beam-pipe.

3.2.5 Luminosity Monitor

The luminosity monitor (LM) comprises 24 plastic scintillation counters with photomultiplier tube (PMT) readout located in front of the end calorimeter, radially between the FPS and the EC. The luminosity in the D \emptyset interaction region is measured from inelastic $p\bar{p}$ collisions. The luminosity is directly proportional to the number of inelastic collisions and is inversely proportional to the effective cross section of the luminosity monitor.

Thus, luminosity is defined as

$$\mathcal{L} = \frac{\nu \times \bar{N}_{LM}}{\sigma_{LM}}, \quad (3.1)$$

where ν is the frequency of beam crossing, \bar{N}_{LM} is the number of inelastic $p\bar{p}$ collisions per beam crossing, and σ_{LM} is the effective cross section of the LM. By the end of Run II in September 2011, the recorded luminosity was about 10.7 fb^{-1} , as can be seen in Figure 3.8.

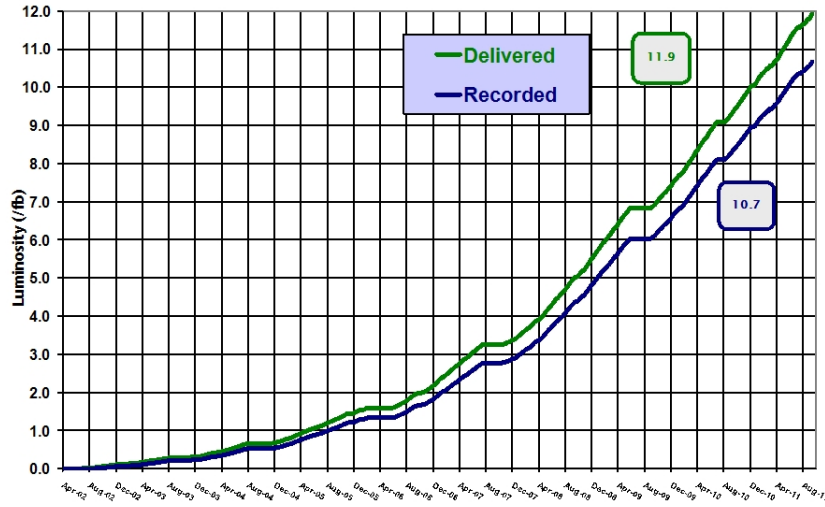


Figure 3.8: Integrated luminosity in Run II

The luminosity monitor also provides halo rates, or the sizes of the the halos which are formed when particles interact with the beam-pipe; smaller halo rates indicate that the particle beam is in a proper position inside the beam-pipe.

3.2.6 Triggers

While a large amount of data can be collected from over 1.7 million collision events inside the detector, storage of these data is limited by the speed with which

they can be written to magnetic tape. Thus, some kind of mechanism is necessary to choose which events to store and which to discard. Triggers are used to choose only the “most interesting” and important collision data. The influx of data is at a frequency in the range of megahertz (MHz), thereby rendering reconstruction of events within the time interval between two crossings of the beams impossible. The storage to magnetic tape occurs at 50 Hz, and DØ uses a trigger system in order to bridge this gap in the frequencies of data flow and data storage.

The DØ triggers are in a three-level structure, such that each higher level has more time and more information to make a decision about what data to keep or discard. Trigger Control Computers (TCC) TCC1, TCC2, and TCC3 control the triggers at the respective levels L1, L2, and L3 and communicate with the COOR, which interacts with all subsystems of the detector and tracks the updated detector configuration and controls the run. The Level 1 (L1) triggers are electronic triggers that detect particle flow based on energy and make the decision of keeping an event. The L1 trigger has buffers associated with it, in order to store data while the decisions are made based on input from the trigger framework. The Level 2 (L2) trigger involves preprocessors which work with the inputs from the L1 triggers. All data from various detector components are correlated and the physics objects are passed to the L2 Global trigger for decision-making. The trigger framework interacts with both the L1 and the L2 triggers, as shown in Figure 3.9 [13]. Level 3 (L3) involves software triggering for preliminary data reconstruction and storage. Data available for L3 must have already passed one of the 128 physics triggers in L1 and must have passed through the scripts imposed by L2. Filter tools of the L3 trigger make decisions based on physics objects

themselves or the relation between them (such as angular separation of two objects).

Apart from keeping track of the updated detector configuration and controlling the runs, COOR (Figure 3.9) also sends information to various subsystems and ensures that user-issued commands do not create conflicts.

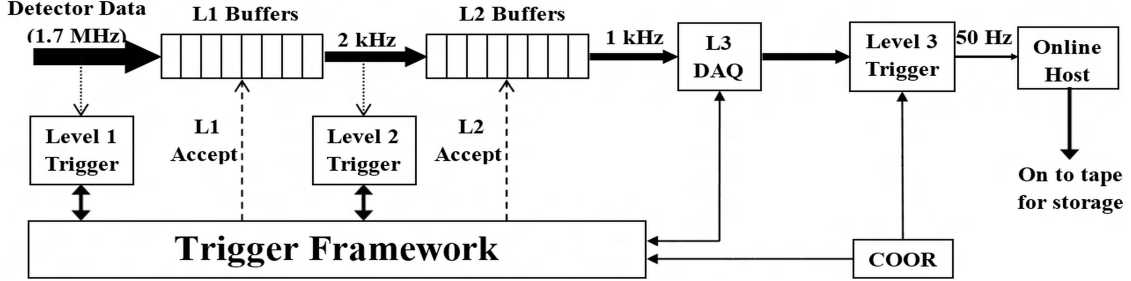


Figure 3.9: Data flow in DØ triggers

The trigger framework (TRGFR) coordinates with various subsystems of the L1 and L2 triggers, as shown in Figure 3.10, and communicates with COOR, TCC, and front-end electronics. In addition, it applies “prescales” to high-frequency events at the Level 1 trigger. Prescales for each trigger are determined based on luminosity – these numbers are set according to the frequency of the particular collision event, and are applied so that the data from the rarest-occurring events are given the highest priority to be kept against more frequently occurring events and that the most frequently occurring events are given the least priority to be kept. The trigger framework also provides scalars for counting trigger rates and dead times. The trigger framework also enables accurate jet reconstruction by accurately determining the position of the primary vertex in the reconstructed jet and by the removal of hot calorimeter cells.

This analysis uses the inclusive jet triggers JT8, JT15, JT25, JT45, JT65, JT95, and JT125, which trigger on jets with uncorrected p_T of 8, 15, 25, 45, 65, 95, and 125 GeV respectively.

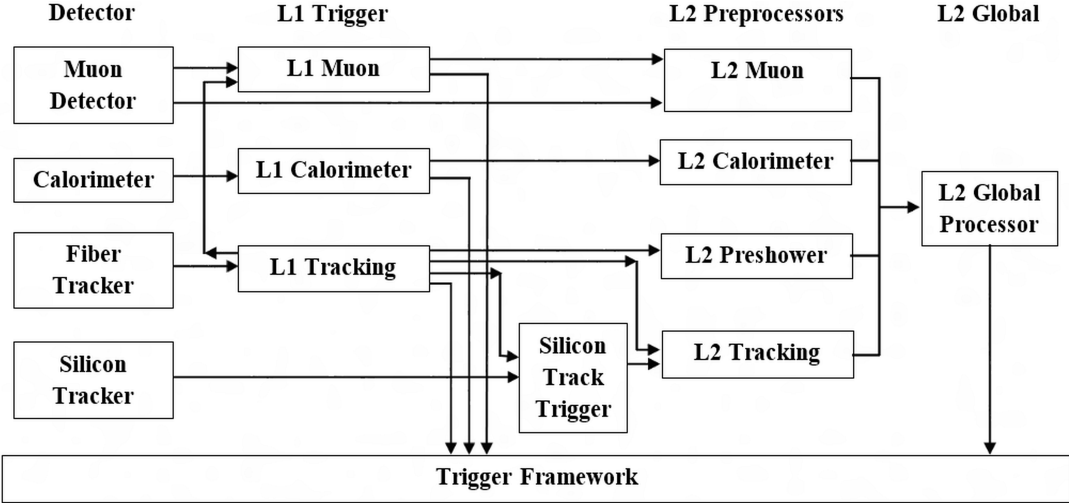


Figure 3.10: Trigger framework in DØ triggers

3.2.7 Data Acquisition at DØ

The data acquisition system (L3DAQ, or simply DAQ) receives the data from readout crates to the L3 processing nodes and facilitates communication with COOR. The COOR program is run on the online host system that receives the event data to be distributed for logging and monitoring tasks. COOR, which receives user requests to configure the detector or to start or stop runs, coordinates with the relevant data logging subsystems to execute the received commands. The data are ultimately transported to a robotic tape system located about two miles away from the detector, at a rate of 10 MB/s in order to ensure proper streaming because the tape drive nodes do not have intermediate disk buffers; multiple tape streams are handled by the online

host system which also enables buffering in the situations where the tape robot is unavailable.

3.3 Jet Energy Calibration and p_T Resolution

Jet energy calibration or jet energy scale (JES) and p_T resolution happen to be the two largest systematic uncertainties that affect jet observables and also require the largest corrections.

3.3.1 Jet Energy Calibration

The jet energy calibration is the procedure that links initial particles produced in hard scatter process and calorimeter energy deposits clustered into calorimeter jets, through hadronization of outgoing partons in showers into particle jets. Jet energy is biased due to calorimeter's different responses to different particles. Uncertainties in the energy scale during reconstruction of hadronic jets amplify if not corrected. The purpose of the jet energy calibration is thus to set the calorimeter energies of jets back to the particle-level values existing before their interaction with the detector. Figure 3.11 is a graphical depiction of the jet energy scale at different levels.

Software reconstruction of a jet is done by adding energy-momentum four-vectors of each calorimeter tower defining the jet. The jet energy calibration is done such that it takes into account the offset energy, calorimeter response, relative response correction, and the showering correction.

The corrected jet energies are thus given by

$$E_{jet}^{particle} = \frac{E_{jet}^{calorimeter} - O}{F_\eta \cdot R \cdot S} \cdot k_{bias}. \quad (3.2)$$

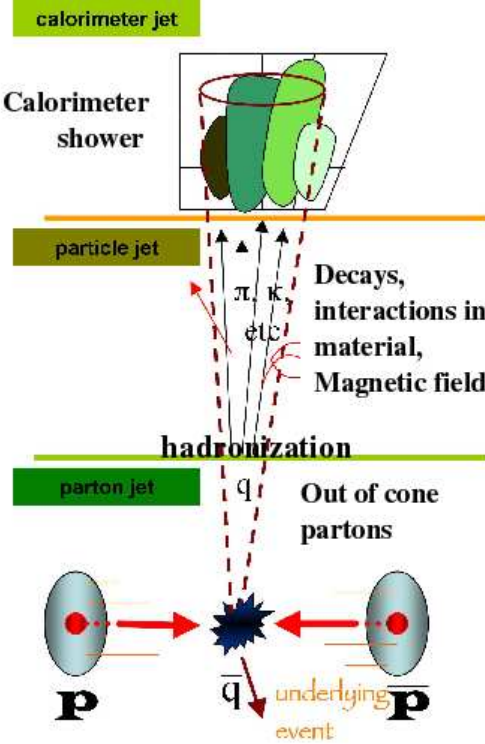


Figure 3.11: Jet energies at parton, particle, and calorimeter levels [21]

Each of the contributing terms are introduced hereunder. All these contributors to the jet energy calibration depend on the position of the jet in the detector (defined by η and ϕ), jet energy (E), and the number of hard interactions in the event (N_{vtx}).

The offset energy, O , is the energy due to noise, pileup, and the “underlying event” which happens when the actual proton-antiproton collision occurs. The offset energy is estimated as the sum of energy densities from all towers within the jet cone. Multiple interactions between colliding beams adds additional energy to the signal in the form of noise due to the electronics or uranium noise. The non-zero energy measurement in the calorimeter when there is no beam is nullified by calibration but remnants of it still affect the measurement. Pile-up occurs because the preamplifiers in the calorimeter work slower than the beam crossing, thus setting a previous

signal as the baseline to another signal and thereby subtracting the wrong baseline. Multiple interactions (MI) are measured using minimum-bias (MB) events triggered by luminosity monitors. MB events with one primary vertex are subtracted from these total number of events in order to estimate the MI events. Noise is estimated using zero-bias (ZB) events with no specific trigger requirements and require to have no vertices. The total offset correction is done for a jet cone with specific η by adding up all calorimeter towers within ϕ .

$$(N_{pv}, \eta, \mathcal{L}_{inst}) = MI(N_{pv}, \eta, \mathcal{L}_{inst}) - MI(N_{pv} = 1, \eta, \mathcal{L}_{inst}) + NP(N_{pv}, \eta, \mathcal{L}_{inst}). \quad (3.3)$$

The calorimeter's absolute response correction, R , is the largest numerical correction to the jet energy scale. Due to particle interactions with material in the tracking system after collision, they may be bent due to the magnetic field and may not be a part of the jet as they should be. Also, DØ is a non-compensating detector, implying that the response for electromagnetic particles (linear) and hadronic particles (logarithmic) is different. While this factor can be found through Monte Carlo simulation by comparing the reconstructed jets with true particle-level energies (ratio of observed signal to incident energy), this does not give a complete measure as some of the detector effects are not simulated using Monte Carlo. Thus, the data is also compared by a method known as the missing E_T projection factor (MPF), according to which the response of a tag object (a jet or a Z boson or a photon) and with that of a probe object (a second jet) is compared. Ideally, the magnitudes of the momenta of the tag jet and the recoiled jet are the same and thus their vector sum is zero as

the recoil is in an exactly opposite direction as the tag jet. However, in a practical situation, the tag jet results in a recoil with a momentum whose magnitude is less than that of the tag jet itself by an amount that accounts for the missing transverse energy. That is, $|\vec{p}_{T,tag}^{measured}| + |\vec{p}_{T,recoil}^{measured}| = \cancel{E}_T$. Since the response correction is simplistically defined as the ratio of the energy measured and the actual energy, or $R \cdot p_T = p_T^{measured}$, the response correction is given, for a certain value of η , as

$$R = \frac{R_{recoil}}{R_{tag}} = 1 + \frac{\cancel{E}_T \cdot \eta_{T,tag}}{p_{tag}^{measured}}, \quad (3.4)$$

Imposing the requirements that the tag and probe objects are exactly back to back (*i.e.* $\Delta\phi > 3.0$) and that the pseudorapidity of the photon is $|\eta| < 1.0$ and that of the jet is $|\eta| < 0.4$, it can be assumed that $R_{recoil} \approx R_{jet}$.

The relative response correction, also called the η -intercalibration F_η , is done to ensure equal jet response everywhere within the calorimeter. The detector response is non-uniform as a function of η in regions not instrumented as well ($0.5 < |\eta| < 1.8$). The inter-cryostat detector (ICD, $1.1 < |\eta| < 1.4$) and the massless gap (MG) detector ($0.7 < |\eta| < 1.2$) cover a part of this region. The η -intercalibration precedes measuring energy dependence of response correction. Thus, jets in all η regions are corrected accordingly by comparing a probe jet to the central response correction using the MPF method:

$$F_\eta(E, \eta_{detector}) = \frac{R(E, \eta_{detector})}{R_{CC}(E)}. \quad (3.5)$$

Showering correction, S , is done to ensure that the energy inside the cone of the jet does not come from outside as a shower at an edge of the cone or due to a

change in trajectory by the solenoid's field. In other words, S is a correction factor for the net energy flow across the boundary of the jet cone due to showering which is a result of interactions with the detector material. The calculation of the showering correction involves using the same sample as that used for MPF in calculating the relative response correction with the events being back to back $\gamma + 1$ jet with only one vertex (in order to eliminate MI effects); the tag object for this calculation can be in any η region. Jet energy profile, energy distribution in rings of $\Delta\mathcal{R}(y, \phi)$ with respect to jet axis, is determined with the jet reconstruction algorithm. Energy from the particle jets reconstructed within the cone and outside the cone are estimated from the MC. The showering correction is determined as the ratio of the visible energy in a cone of radial width smaller than that of the cone radius to the visible energy from the total particle jet energy as

$$\frac{E_{\text{jet}}^{\text{measured}}}{E_{\text{particle jet}}^{\text{measured}}} = \frac{E_{\text{particle jet}}^{\text{measured}, \Delta\mathcal{R} < \mathcal{R}_{\text{cone}}} + E_{\text{not particle jet}}^{\text{measured}, \Delta\mathcal{R} < \mathcal{R}_{\text{cone}}}}{E_{\text{particle jet}}^{\text{measured}}}. \quad (3.6)$$

Additional biases in the jet energy scale are corrected through the factor, k_{bias} [22].

For instance, the MPF method introduces a bias at $\sim 1\%$ level, unclustered energies are left over during collision events because the jet reconstruction has a threshold of $p_T = 6 \text{ GeV}$, and response to photons can be off as they are narrower than jets.

While the $\gamma + \text{jet}$ sample is dominated by quark jets at low p_T ($p_T < 100 \text{ GeV}/c$) and by gluon jets at high p_T , the dijet sample has an exact opposite behavior. These differences have been accounted for exclusively with particular emphasis on calibration of QCD samples such as the inclusive jet samples and the dijet samples [23]; the relative response bias method was used for forward regions and MC comparison was

used for the central region. The correction factors for each of the four components of the JES are studied for these particular samples and the jet energy scale corrections for these samples are usually referred to as J4S corrections.

3.3.2 p_T Resolution

Jet p_T resolutions are responsible for the largest corrections to the observable. The p_T resolution uncertainties originate from 15 independent sources; the effects of each source are taken as fully correlated between all data points. The systematic uncertainty of the noise component has contributions from four different angular regions, namely CC ($0.0 < |\eta| < 0.8$), IC ($0.8 < |\eta| < 1.2$), EC ($1.2 < |\eta| < 2.4$), and the very forward region ($|\eta| > 2.4$). The statistical uncertainty of the final fit also contributes to the systematic uncertainty through four sources: the fit uncertainty, the soft radiation correction, the particle level imbalance fit, and Monte Carlo reconstruction in the closure test. These four contributions of the statistical uncertainty contribute as seven more correlated sources: six sources distributed through an angular width of 0.4 each in the angular region $0.0 < |\eta| < 2.4$, and a seventh source pertaining to the remaining angular region ($|\eta| > 2.4$).

3.4 Detector Simulation

A thorough understanding of the detector effects is necessary to reliably measure jet production rates and/or differential distributions which are convoluted with detector resolution effects. Different jet transverse momentum resolutions and jet energy calibrations for data and Monte Carlo indicate that the jet reconstruction is not completely described by the GEANT-based [24] simulation of the DØ detector [13].

Thus, the current analysis uses a parametrized simulation of the DØ detector response for jet measurements, called “DØJetSim” [25], which is based on the best understanding of all the relevant instrumental effects pertaining to the data set being used in the analysis. The input is based on jets reconstructed with the DØ Run II cone algorithm in events generated by the Monte Carlo generators SHERPA with MSTW2008LO PDFs [26] and PYTHIA tune QW with CTEQ6.6 PDFs [27]. DØJetSim is used to determine all the additional corrections and the uncertainties pertaining to the data set after implementing the jet energy scale corrections and rapidity-bias corrections as in dijet four-vector JES (J4S). As all jet four-vectors vary due to the different detector effects, the ratio of the original, “true” observable and the simulated observable gives the correction factor that needs to be applied to each individual bin of the data. The uncertainty of the observable is determined by varying each effect within the limits of its uncertainty.

The instrumental effects that are simulated include: jet transverse momentum (p_T) resolution, jet pseudorapidity (η) resolution, azimuthal angle (ϕ) resolution, the distribution of the vertex position along the beam-line (z_{vtx}), the jet energy scale uncertainties, and jet ID efficiency. Since the official GEANT simulation excluded muons and neutrinos when calibrating the jet energy to particle-energy level, DØJetSim determines the necessary corrections and applies these to the final results [28].

CHAPTER 4

MEASUREMENT PROCEDURE

The current analysis involves selecting suitable data, correcting the data with the help of Monte Carlo simulations, computing the systematic as well as statistical uncertainties that affect the data and simulations, and comparing the final corrected data to the next-to-leading order pQCD predictions of the theory. This chapter deals with all but the final step outlined here, which is presented in Chapter 5.

4.1 Data Selection

The data used for the current analysis have an integrated luminosity of 0.7 fb^{-1} and were collected during 2004–’05. Data from each collision event are arranged in a tree structure called an “ n -tuple” or a “ROOT-tuple”, owing to the fact that these trees can be read by the ROOT framework [29]. The n -tuple sorts the jet variables in each event in the decreasing order of jet transverse momenta, with the first jet having the highest jet transverse momentum. Since the current research aims to analyze dijet or multijet events, the analysis considers only events with at least two “good” jets. The goodness of jets implies that the flag “calfail” is set to “false” for these runs (in order to remove data collected while the calorimeter has a problem), and that the z positions of the jet vertices are within 50 cm of the center of the detector. The standard missing E_T cut ($\cancel{E}_T/p_T < 0.7$ for the leading jet, in order to remove the

effects of cosmic ray incidence on the detector) is applied to these events and only the primary vertices which are constructed using at least three tracks (so as to ensure that the collision event occurred in a fiducial region of the detector) are chosen. More quality cuts are imposed on the data according to [30], including the coarse hadronic fraction (CHF) cut to remove jets dominated by the coarse hadronic calorimeter noise, the minimal electromagnetic fraction (EMF) cut to remove jets dominated by hadronic noise, and the Level 1 confirmation cut whose effect is negligible.

In addition to the above standard data selection criteria, a few more requirements specific to the current analysis are imposed on the data:

- y^* , defined as one-half of the absolute difference between the rapidities of the two leading jets, must be less than or equal to 2.0.

$$y^* = \frac{|y_1 - y_2|}{2} \leq 2.0, \quad (4.1)$$

- y^{boost} defined as the average value of the rapidities of the two leading jets, must be less than or equal to 0.5.

$$y^{boost} = \frac{y_1 + y_2}{2} \leq 0.5, \quad (4.2)$$

- The second leading jet transverse momentum is at least 30 GeV.

$$p_{T_2} > 30 \text{ GeV}, \quad (4.3)$$

- The leading jet transverse momentum is at least one-third of H_T

$$p_{T_1} > \frac{H_T}{3}, \quad (4.4)$$

where H_T is defined as the sum of all jet transverse momenta such that the transverse momentum of individual jets is at least 30 GeV and that the absolute difference of individual jet rapidity and boost rapidity is less than the maximum value of y^* of 2.0 (as mentioned in Section 2.6).

The subscripts 1 and 2 above, for p_T and y , refer to the leading and the second leading jet respectively; the subscript i refers to the index of the jet in the list of all jets sorted in decreasing order of p_T .

Justification for the selection criteria

It may be noticed that the definitions of y^* and y^{boost} are such that the maximum absolute jet rapidity y in this analysis is 2.5. Thus, it can be seen from Figure 3.7 that the current analysis covers the central, intermediate, and forward regions of the DØ detector. The ranges in y^* and the requirements for p_T^{min} , y_{max}^* , and y^{boost} are chosen such that all jets are always inside $|y| < 2.5$ where the jet energy scale and jet p_T resolutions are well known and where the DØ jet triggers are fully efficient. The requirement $p_{T_1} > \frac{H_T}{3}$ gives a well-defined lower boundary for the leading jet p_T in each H_T bin based on which the jet triggers are selected.

Implementation

For the current analysis, one histogram is filled with the H_T for events within the inclusive jet cross section encompassing the entire accessible range of $\Delta\phi$ and three more distinct histograms are filled with the H_T for events within the inclusive jet cross section for individual regions of $\Delta\phi_{max}$, *i.e.* $\Delta\phi_{max} = \frac{7}{8}\pi$, $\frac{5}{6}\pi$, or $\frac{3}{4}\pi$. These histograms are binned in H_T with the bin boundaries chosen thus to match with

trigger turn-ons: 180, 205, 235, 270, 310, 360, 415, 470, 530, 600, 680, 770, and 900 (all in GeV). The observable $R_{\Delta\phi}$ (defined in Section 2.6) is thus computed as the ratio of the histogram filled for the particular $\Delta\phi_{max}$ region and the histogram filled for the inclusive jet cross section. This computation is performed in each of the three y^* regions, *i.e.* 0.0–0.5, 0.5–1.0, and 1.0–2.0.

4.2 Triggers

In order for a trigger to be used in a particular range of H_T , the particular trigger must have been at least 98 % efficient in that range. This criterion can be verified by comparing the H_T cross section distribution curves for a trigger to corresponding curves from a trigger with lower p_T threshold. Turn-on curves thus obtained for individual triggers in each y^* region and $\Delta\phi_{max}$ region are fit using the modified error function:

$$f(H_T) = 0.5 + 0.5 \times \text{erf} \left(\frac{H_T - a}{b + c \cdot \log(H_T/\text{GeV})} \right), \quad (4.5)$$

where a , b , and c are the three fit parameters used to optimize the fit. The $\frac{\chi^2}{ndf}$ for the fit was often between 1.0 and 2.0 but it had a higher value occasionally, particularly when the fit could not get better due to fluctuations and/or lack of statistics.

This analysis uses the triggers JT45, JT65, JT95, and JT125, and JT25 is used for trigger studies. Since the highest jet p_T is always over 60 GeV ($p_T > \frac{H_T}{3}$) and $H_T > 180$ GeV as noted in Section 4.1), JT45 was turned on at this transverse momentum and thus JT25 was not required to be used for the analysis. Trigger efficiencies are studied as a function of H_T by comparing the dijet cross section in data

sets obtained by triggers with different p_T thresholds in regions where the trigger with lower threshold is fully efficient. The trigger with lowest p_T threshold has been shown to be fully efficient in studies of an event sample obtained independently with a muon trigger [31]. The turn-on curve for each trigger was determined for the inclusive dijet cross section and for each of the three $\Delta\phi_{max}$ values, in each of the three y^* regions. In order to determine these efficiencies, four histograms per trigger are filled with the H_T for events based on the particular trigger that fired the event: one histogram for events with the inclusive dijet cross section encompassing the entire accessible range of $\Delta\phi$ and three histograms for events within the inclusive dijet cross section for individual regions of $\Delta\phi_{max}$ as above. Trigger efficiencies thus determined are presented in Appendix A. Table 4.1 lists the ranges of H_T used for each trigger such that the particular trigger was at least 98 % efficient in that range of H_T in all the $\Delta\phi_{max}$ and y^* regions. The table also lists the approximate value of H_T for which the 98 % efficiency is achieved in the most forward region of y^* for $\Delta\phi_{max} = \frac{7}{8}\pi$. It can be seen that the range where the trigger is used is nearly always after the trigger is 98 % efficient. Also listed in the table are the integrated luminosities pertaining to the data set used for the current analysis.

Table 4.1: H_T ranges and integrated luminosities for triggers in this analysis

Trigger	$\gtrsim 98\%$ efficiency for $\Delta\phi_{max} = \frac{7}{8}\pi$, $1.0 < y^* < 2.0$	H_T	\mathcal{L} (pb^{-1})
JT45	180 GeV	> 180 GeV	17
JT65	260 GeV	> 310 GeV	72
JT95	390 GeV	> 415 GeV	507
JT125	530 GeV	> 530 GeV	707

4.3 The Observable $R_{\Delta\phi}$

The observable $R_{\Delta\phi}$ is measured in three y^* regions (0.0–0.5, 0.5–1.0, and 1.0–2.0), and for different $\Delta\phi_{max}$ requirements of $\frac{7}{8}\pi$, $\frac{5}{6}\pi$, or $\frac{3}{4}\pi$, according to the methodology described in Section 4.1. The histograms used for this purpose are shown in Figure 4.1. Due to lesser phase space, the extreme kinematic regions in H_T have fewer statistics rendering their use in the analysis unreliable. Thus, bins with less than 50 events have not been considered for this analysis.

Events from SHERPA [32] and PYTHIA [33] Monte Carlo simulations have been reweighted for a previous measurement of multijet cross section ratios [34] to describe the p_T and y distributions of the three leading jets in the event. Figure 4.2 shows the observable in data overlaid with reweighted SHERPA and PYTHIA Monte Carlo simulations at the detector-level.

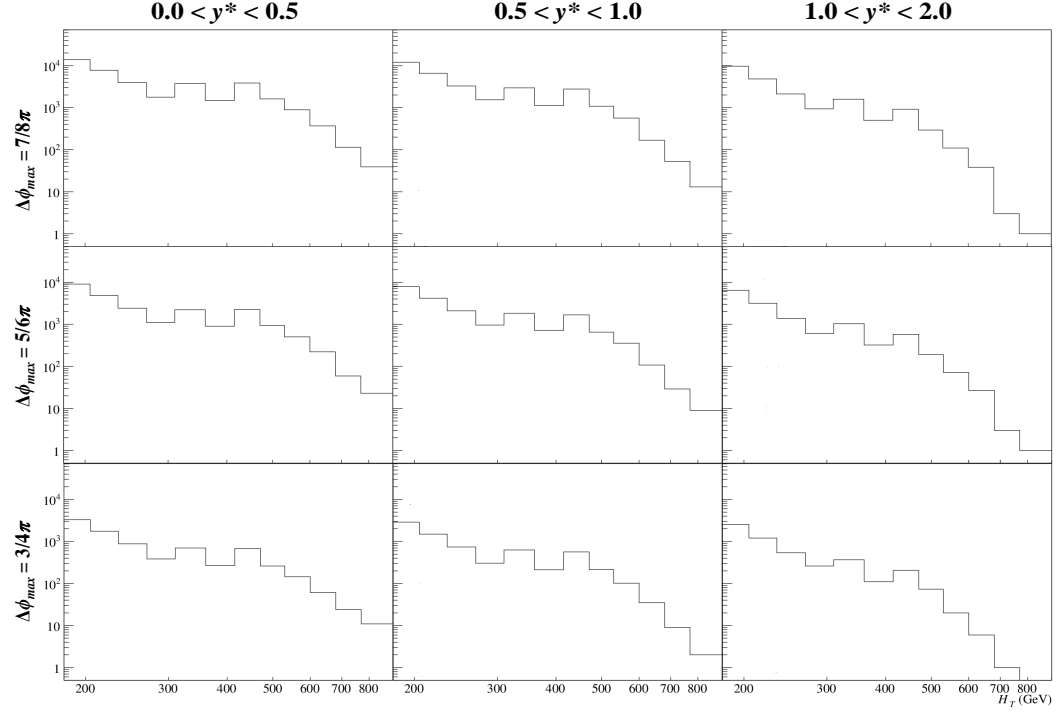
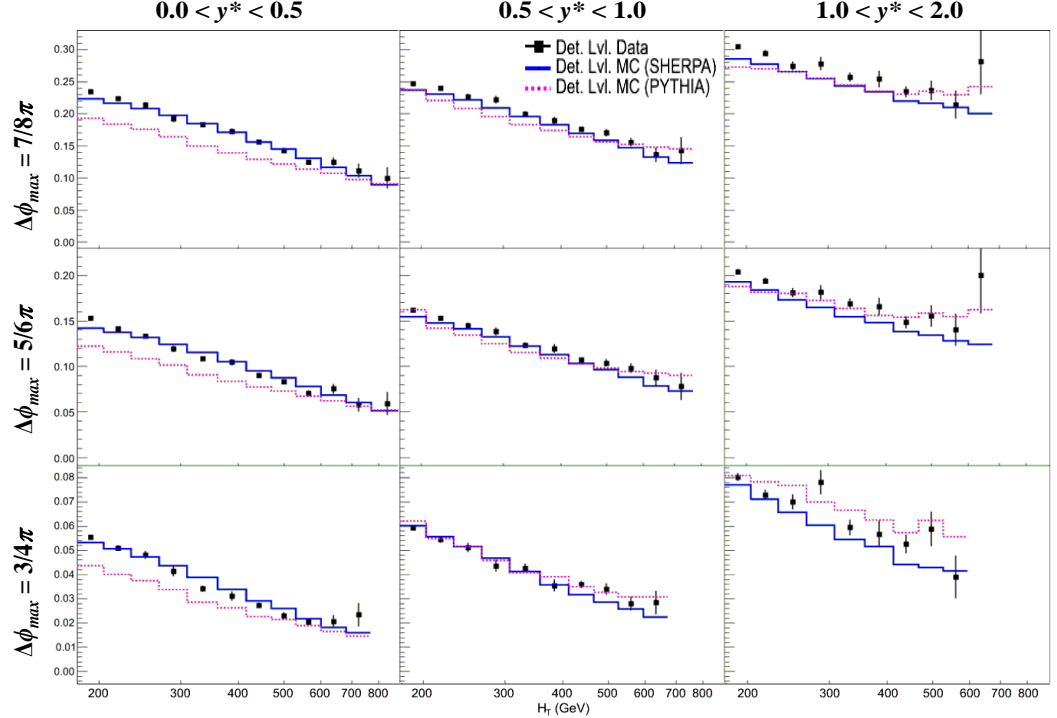


Figure 4.1: Event counts per bin

Figure 4.2: $R_{\Delta\phi}$ distributions overlaid with detector-level SHERPA and PYTHIA Monte Carlo simulations

4.4 Correction Factors

The observable $R_{\Delta\phi}$ shown in Figure 4.2 is measured in the data at the detector level. This distribution needs to be brought to the particle level (or the “truth level”) by correcting for all the detector effects. Reweighted PYTHIA and SHERPA Monte Carlo simulations are employed for this purpose.

The observable $R_{\Delta\phi}$ is calculated from the Monte Carlo at the particle level and at the detector level and a ratio thereof is computed. This ratio is treated as the “correction factor” for the data. The correction procedure can be expressed mathematically as follows, where the observable $R_{\Delta\phi}$ in all cases is a function of H_T , y^* , and $\Delta\phi_{max}$:

$$(R_{\Delta\phi})_{MC, \text{particle level}} = \left[\frac{\frac{d^2\sigma_{dijet}(\Delta\phi < \Delta\phi_{max})}{dH_T dy^*}}{\frac{d^2\sigma_{dijet}(\text{inclusive})}{dH_T dy^*}} \right]_{MC, \text{particle level}}, \quad (4.6)$$

$$(R_{\Delta\phi})_{MC, \text{detector level}} = \left[\frac{\frac{d^2\sigma_{dijet}(\Delta\phi < \Delta\phi_{max})}{dH_T dy^*}}{\frac{d^2\sigma_{dijet}(\text{inclusive})}{dH_T dy^*}} \right]_{MC, \text{detector level}}, \quad (4.7)$$

$$(\text{Correction Factor})_{MC} = \frac{(R_{\Delta\phi})_{MC, \text{particle level}}}{(R_{\Delta\phi})_{MC, \text{detector level}}}, \quad (4.8)$$

$$(\text{Observable})_{\text{corrected}} = (\text{Correction Factor})_{MC} \times (\text{Observable})_{\text{uncorrected}}. \quad (4.9)$$

The correction factors thus obtained from SHERPA and PYTHIA Monte Carlo simulations are depicted in Figure 4.3 for the three values of $\Delta\phi_{max}$ and the three regions of y^* . The figure also shows a smoothed average of the correction factors obtained using SHERPA and PYTHIA, which ignores the fluctuations in some of the

bins. The smoothing is done using the 353QH algorithm [35] included in the ROOT framework. It can be observed from the figure that the smoothed correction factors are usually within 5 %; as these are multiplicative factors, it can be deduced that the detector effects do not affect the data by more than 5 % in most of the H_T range.

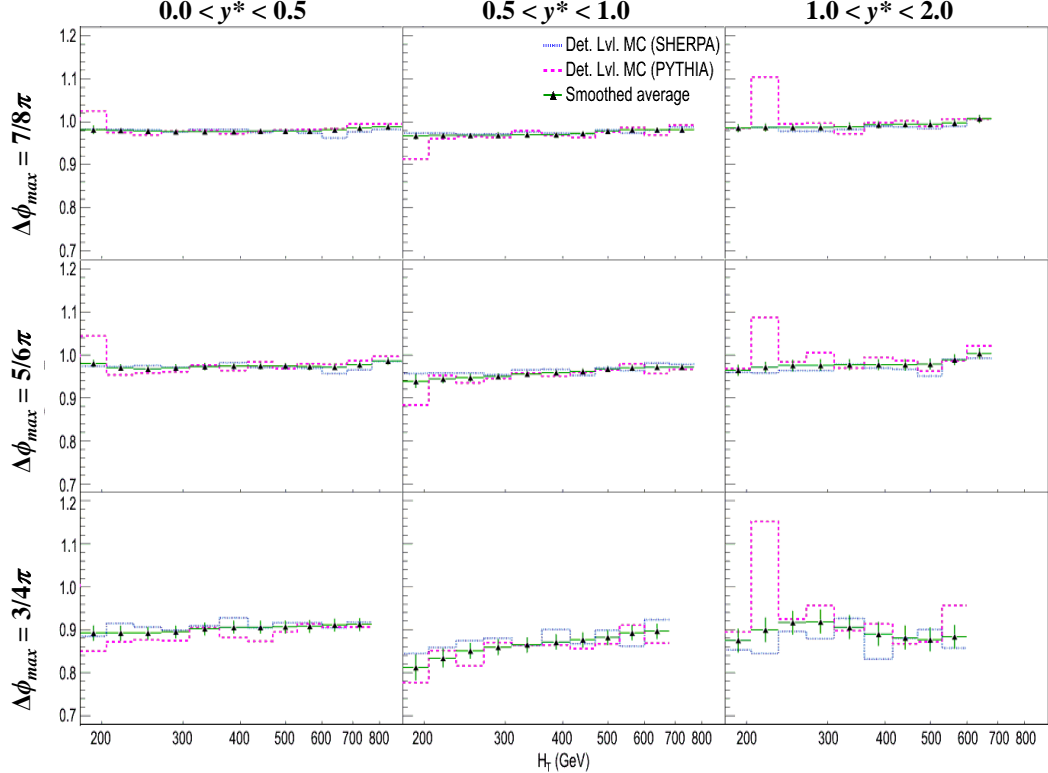


Figure 4.3: Total correction factors obtained from fast-parametrized Monte Carlo simulations

Various individual correction factors contribute to these total correction factors, namely η resolution, ϕ resolution, jet p_T resolution, jet ID efficiency, and corrections to include muons and neutrinos (*cf.* Section 3.4). These individual correction factors are calculated in the same way as the total correction factors obtained through the Monte Carlo simulations and are presented in Appendix B.

4.5 Systematic Uncertainties

While the JES uncertainty is a combination of uncertainties from 49 different sources, the p_T resolution uncertainty is a combination of 15 different sources as noted in Section 3.3.2. Apart from these two uncertainties arising from multiple sources, there are other uncertainties arising from individual sources that affect the data: jet ϕ resolution, jet η resolution, jet η bias, jet ID efficiency, and modeling of the vertex distribution. Each of these seven different types of uncertainties have an upper variation and a lower variation, the bin-by-bin quadrature sum of which results in the total uncertainty of each particular type. The largest uncertainties that affect the observable $R_{\Delta\phi}$ are due to the jet energy scale and the jet p_T resolution. The upper/lower effects due to the variation of each source of uncertainty is added in quadrature to obtain the total upper/lower systematic uncertainty. The upper and lower total systematic uncertainties are then added in quadrature to the respective counterparts of the statistical uncertainties which affect the data, so as to obtain the total uncertainty of the data in each H_T bin. Figure 4.4 shows the upper and lower total systematic uncertainties affecting the observable. The total systematic uncertainties are usually about 2–3 % in the central ($0.0 < y^* < 0.5$) and intermediate ($0.5 < y^* < 1.0$) regions and for $\Delta\phi_{max} = \frac{7}{8}\pi$ and $\Delta\phi_{max} = \frac{5}{6}\pi$. Even in the forward region ($1.0 < y^* < 2.0$) and in the region with the smallest value of $\Delta\phi_{max} = \frac{3}{4}\pi$, the uncertainties are not more than $\sim 5\%$ in most part of the H_T regime. Appendix C lists the upper and lower variations of the seven types of individual uncertainties.

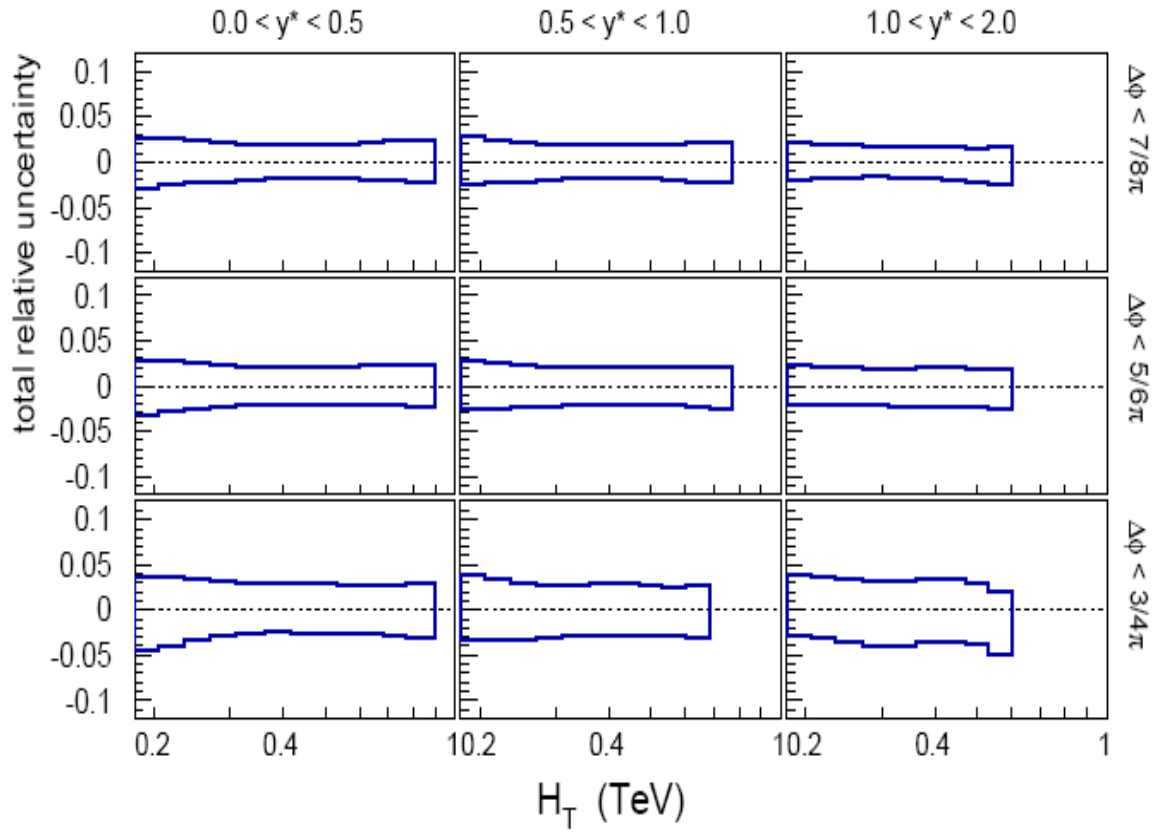


Figure 4.4: Upper and lower variation of the total systematic uncertainties

CHAPTER 5

RESULTS

The results of the measurement are shown in Figure 5.1 as the values of $R_{\Delta\phi}$ corrected to the particle level.

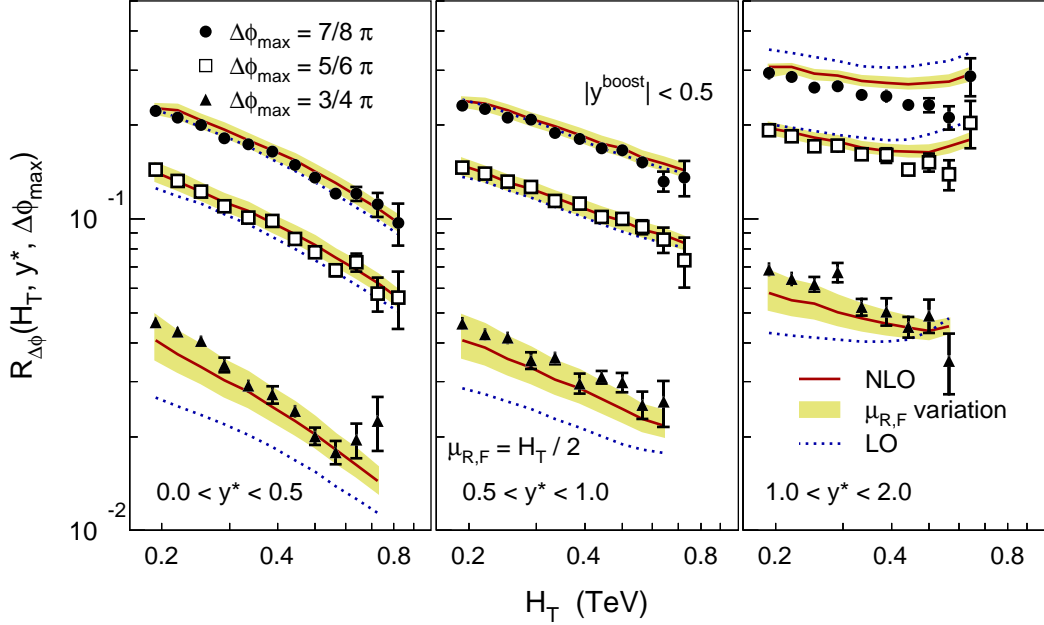


Figure 5.1: Observable $R_{\Delta\phi}$ along with LO and NLO pQCD predictions

Since the observable $R_{\Delta\phi}$ is defined as a triple-differential variable, this figure can be used to evaluate how the observable varies by these three variables, namely H_T , y^* , and $\Delta\phi_{max}$. It can be readily observed that an increase in the value of H_T causes a decrease in the dijet azimuthal decorrelations, as the observable $R_{\Delta\phi}$ falls

along the positive x -axis in all regions of y^* and for all three values of $\Delta\phi_{max}$. In all three y^* regions, it can also be observed that $R_{\Delta\phi}$ decreases as the value of $\Delta\phi_{max}$ becomes smaller. This behavior is expected because of less phase space available for a stronger requirement of the $\Delta\phi_{max}$ value, since the cross section (*i.e.* the numerator of the ratio $R_{\Delta\phi}$) reduces as the kinematically available phase space decreases.

For the first time, the rapidity dependence of dijet azimuthal decorrelations is also observed through the result of the present work. A rise in the value of the observable can be noticed when moving from the central value of y^* (0.0–0.5) to the intermediate region (0.5–1.0) and further into the forward region (1.0–2.0). This behavior is better visible in Figure 5.2 in which the data from Figure 5.1 in selected H_T regions and for different $\Delta\phi_{max}$ requirements are displayed.

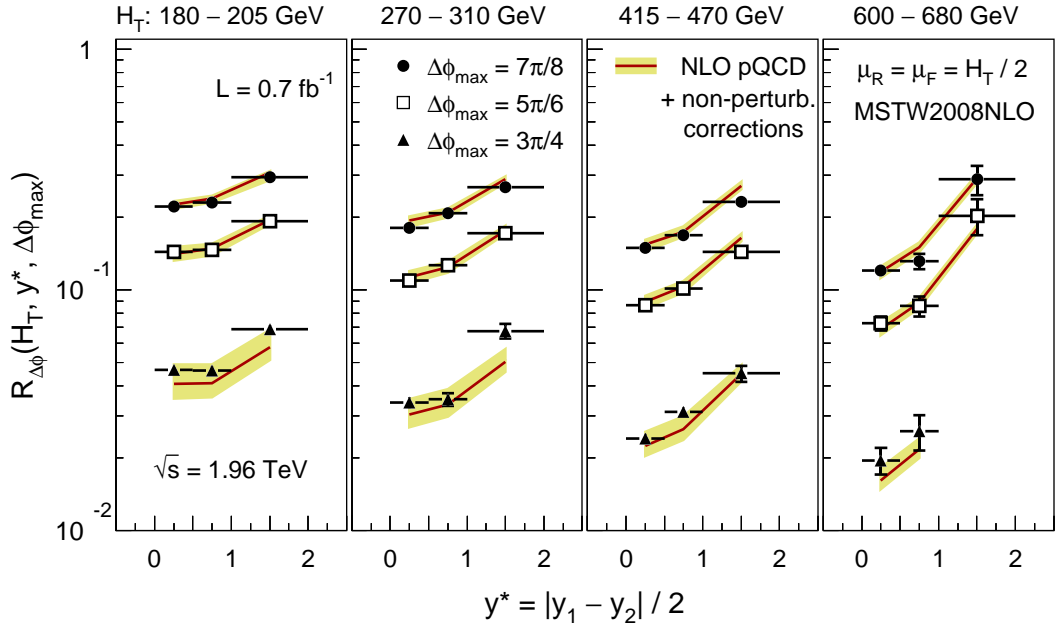


Figure 5.2: Observable $R_{\Delta\phi}$ as a function of y^* in selected H_T regions and for different $\Delta\phi_{max}$ requirements

The next-to-leading-order (NLO) pQCD predictions obtained as outlined in Section 2.7 are presented in Figure 5.1 together with the leading order (LO) pQCD predictions and the data. In order to better compare the theory to the data, a ratio of data and the theory is shown in Figure 5.3. Also included is the ratio of the LO and NLO predictions, which is the inverse of the k -factor, $k = \frac{R_{\Delta\phi}^{NLO}}{R_{\Delta\phi}^{LO}}$.

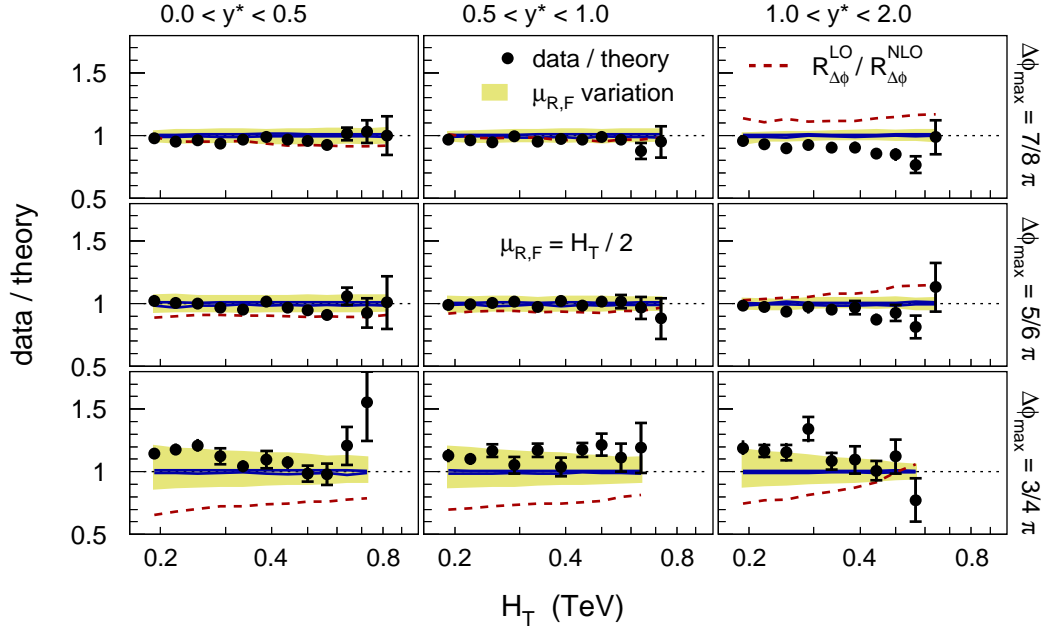


Figure 5.3: Ratio of the data and theory

From the figure it can be observed that the theory closely agrees with the data in the regions $0.0 < y^* < 0.5$ and $0.5 < y^* < 1.0$ for values of $\Delta\phi_{max} = \frac{7}{8}\pi$ and $\Delta\phi_{max} = \frac{5}{6}\pi$. In other words, NLO corrections are small in these four kinematic regions where $1.0 < k < 1.1$. In the forward rapidity region ($1.0 < y^* < 2.0$), theory is higher than the data by about 10–20 %. For large dijet azimuthal decorrelations ($\Delta\phi_{max} = \frac{3}{4}\pi$), the theory is lower than the data by about 10–20 %. Thus, it can be

concluded that there is a poor agreement where the k -factors are large ($1.3 \lesssim k \lesssim 1.6$ for $\Delta\phi_{max} = \frac{3}{4}\pi$) or are less than unity ($0.8 \lesssim k \lesssim 0.9$ at $1.0 < y^* < 2.0$), indicating a larger or negative contribution from the NLO. Larger corrections from further higher orders, *i.e.* NNLO and above, may be expected in these regions ($1.0 < y^* < 2.0$ or $\Delta\phi_{max} = \frac{3}{4}\pi$) as the NLO does not provide a good description of the data.

CHAPTER 6

CONCLUSIONS AND OUTLOOK

6.1 Conclusions

This analysis studies the properties of the strong interaction in hadron-hadron collisions at a center-of-mass energy of 1.96 TeV. For the first time, the rapidity dependence of dijet azimuthal decorrelations is measured at a hadron collider. The current analysis defines and measures a new variable, $R_{\Delta\phi}$, triple-differentially as a function of total transverse momentum, H_T , the dijet azimuthal separation, $\Delta\phi$, and the dijet rapidity y . The analysis uses data with an integrated luminosity of 0.7 fb^{-1} obtained from the DØ detector at the Fermilab Tevatron Collider. The data are corrected for detector effects and are presented at the particle-level.

While previous analyses [1], [37], and [38] did establish that the decorrelations depend on the transverse momentum, p_T , the dependence was not explicitly measured. The current analysis establishes clearly that the dijet azimuthal decorrelations decrease with H_T for all $\Delta\phi_{max}$ requirements and in all rapidity regions. The current analysis also establishes for the first time that dijet azimuthal decorrelations increase with increasing rapidity.

The results are compared to the pQCD predictions at NLO and are found to agree with the theory in those regions where the NLO k -factors are not large, which is at central rapidities ($y^* < 1$) and for azimuthal separations of $\Delta\phi_{max} = \frac{7}{8}\pi$ and $\Delta\phi_{max} = \frac{5}{6}\pi$.

6.2 Outlook

The results of this analysis may be used for extractions of the strong coupling constant, α_s [36]. Since the observable is a ratio, in which the PDF dependence in the numerator and denominator cancel to a large extent, only a weak sensitivity to PDFs remains. Since this analysis is performed over a transverse momentum range of $\sim 90\text{--}450\,\text{GeV}$, the running of α_s as predicted by pQCD can be tested for up to twice the energies of previous measurement at the final LEP energy of 209 GeV [36].

The approach used in this analysis may be extended by the ATLAS and CMS collaborations at the CERN Large Hadron Collider (LHC) for data with center-of-mass energies up to seven times that of the Tevatron. This will increase the accessible H_T range by a similar factor. Observations of the current analysis will also be helpful in other analyses involving precision measurements and searches for new physics where a study of the QCD radiation is necessary to understand the ongoing soft and hard radiative processes.

APPENDIX A

TRIGGER EFFICIENCIES

The trigger turn-on curves for individual triggers are presented in the Figures A.1 through A.12, with a trigger's turn-on curves in particular regions of y^* in one figure that includes the turn-on curve for inclusive jet cross section and the counterparts for $\Delta\phi_{max} = \frac{7}{8}\pi$, $\frac{5}{6}\pi$, and $\frac{3}{4}\pi$. The horizontal dashed lines on each turn-on curve indicate the range of efficiencies between 0.98 and 1.0, while the vertical dashed line indicates the H_T value above which the trigger is used. It can be noted that all triggers are at least 98 % efficient in the desired H_T range in all y^* regions and for all values of $\Delta\phi_{max}$. However, while the fits on the turn-on curves for triggers JT45 ($0.0 < y^* < 0.5$ and $0.5 < y^* < 1.0$) and JT125 ($0.5 < y^* < 1.0$) when $\Delta\phi_{max} = \frac{3}{4}\pi$ may indicate a lesser efficiency in the desired range of H_T , it may be observed that these are only cases of poor fits due to lower statistics. The trigger turn-on curves thus establish the fact the stipulated efficiency is achieved through the desired range of H_T where each trigger was used (Table 4.1).

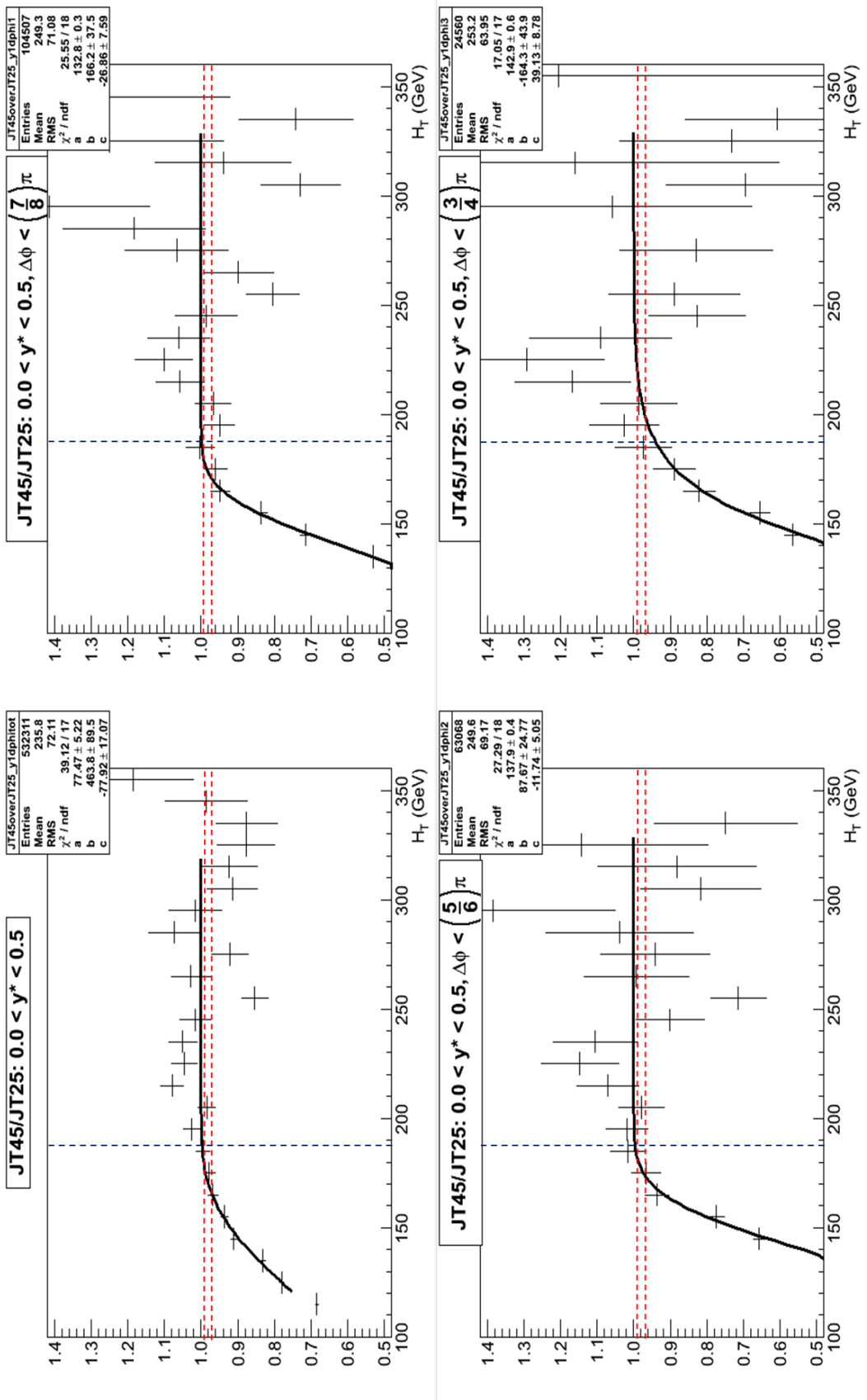


Figure A.1: Trigger turn-on curves (Trigger: JT45; $0.0 < y^* < 0.5$)

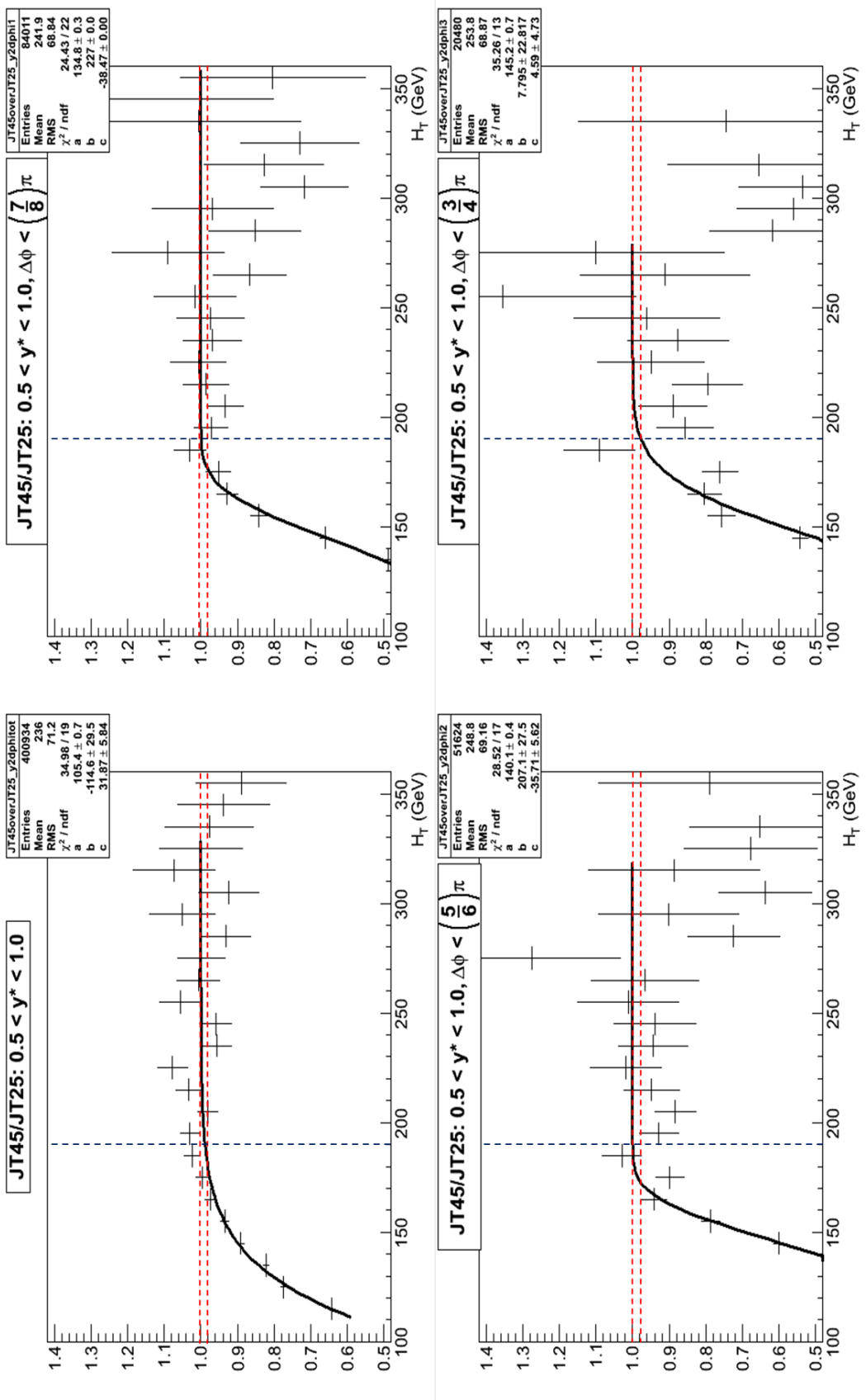


Figure A.2: Trigger turn-on curves (Trigger: JT45; $0.5 < y^* < 1.0$)

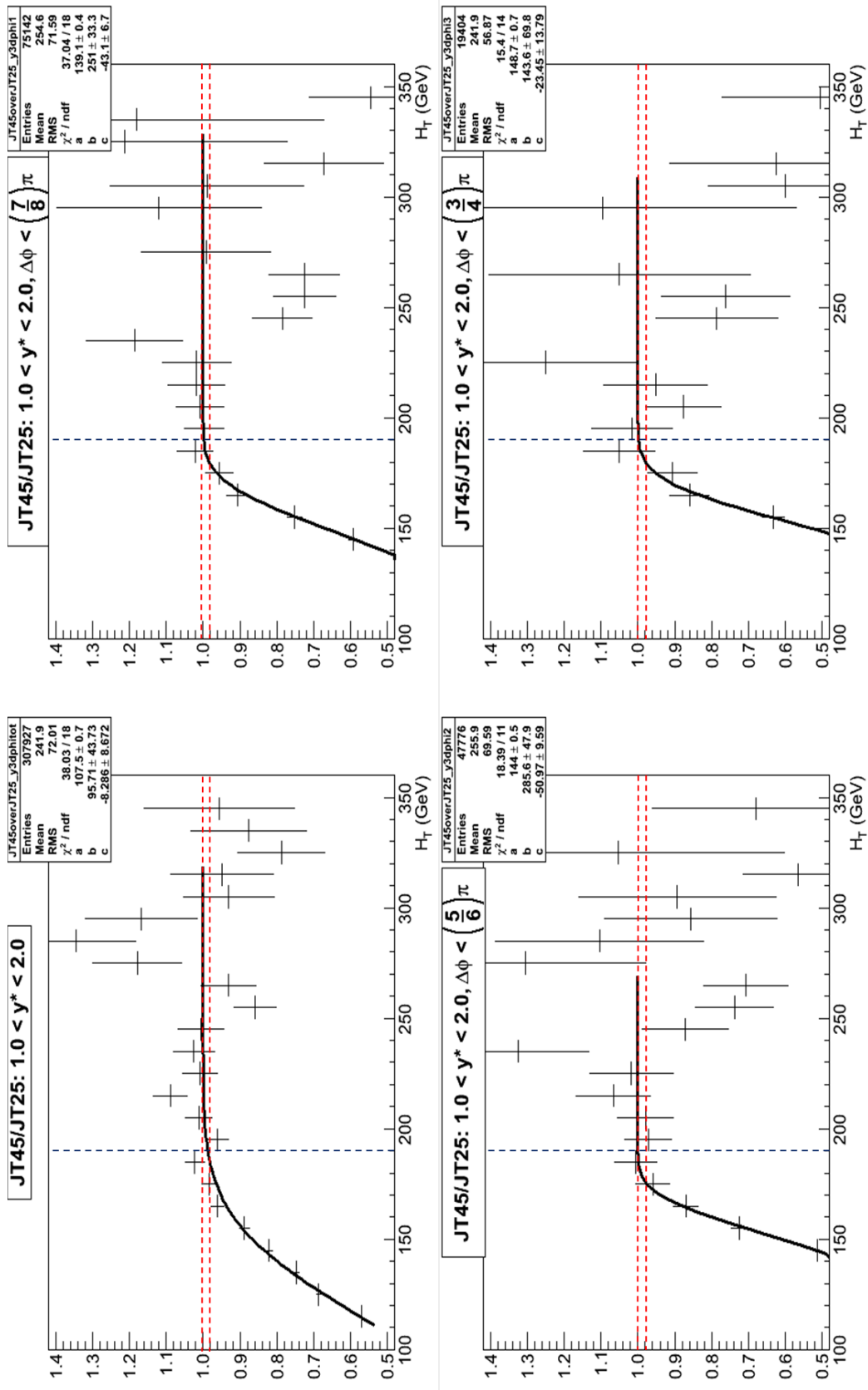


Figure A.3: Trigger turn-on curves (Trigger: JT45; $1.0 < y^* < 2.0$)

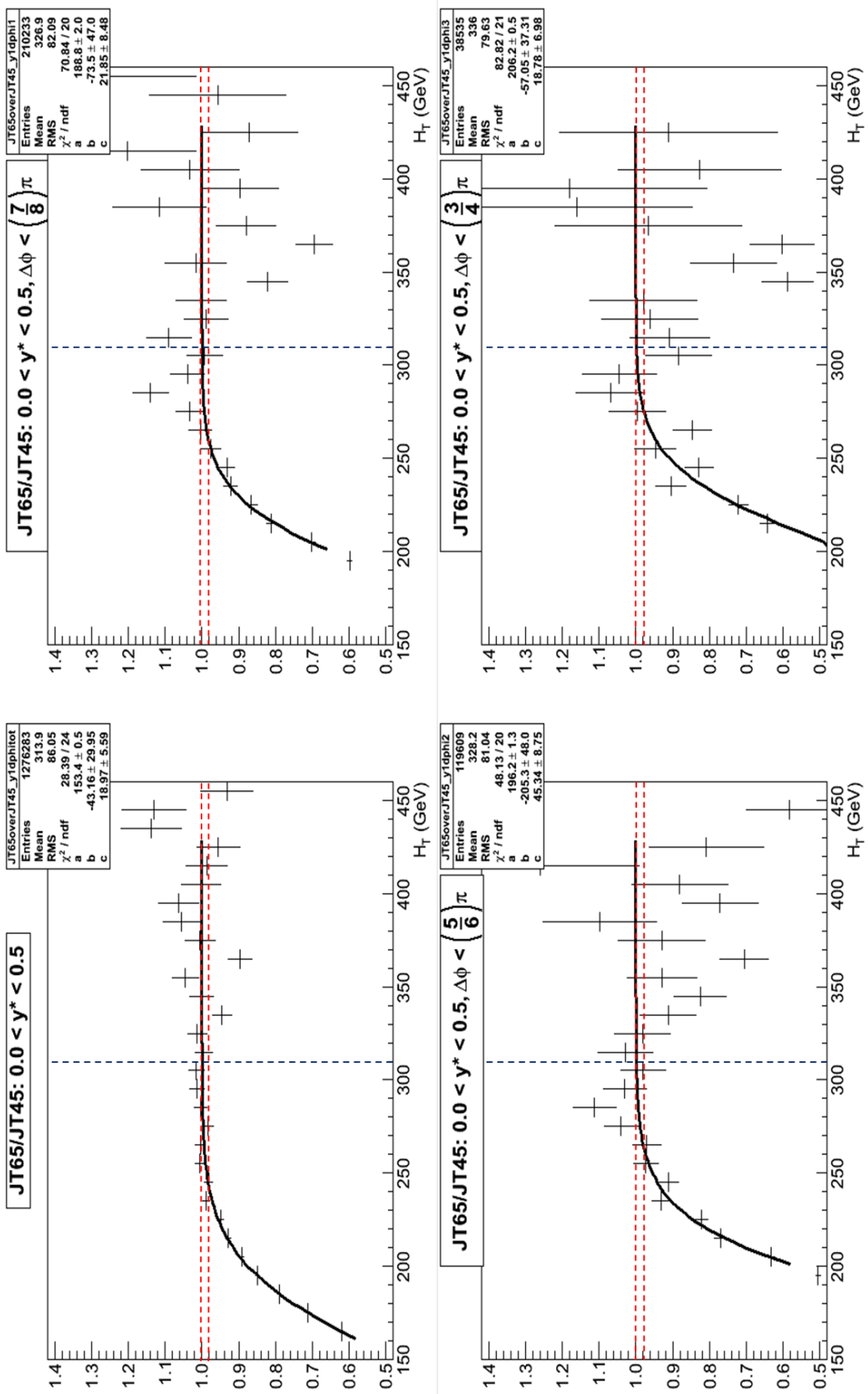


Figure A.4: Trigger turn-on curves (Trigger: JT65; $0.0 < y^* < 0.5$)

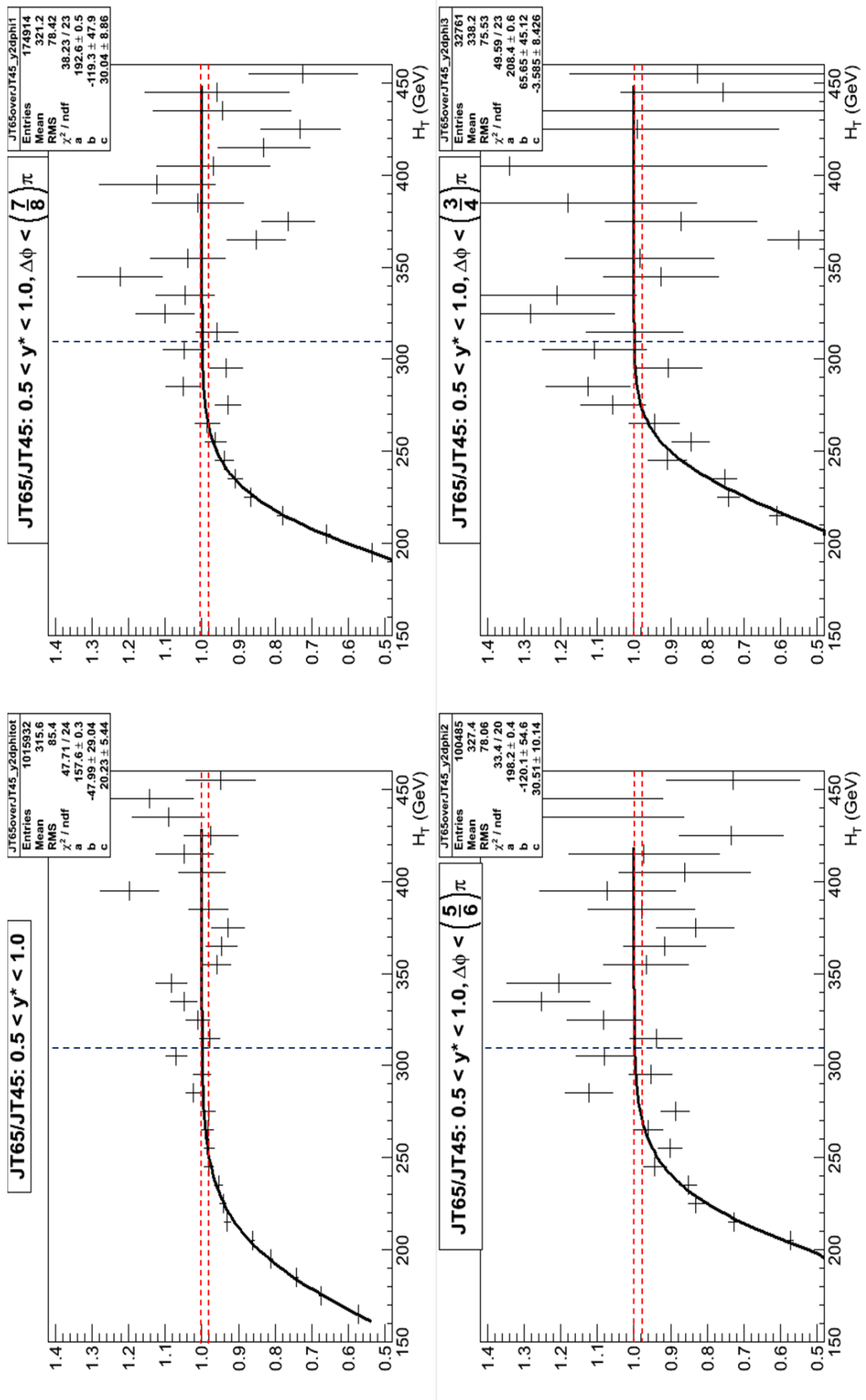
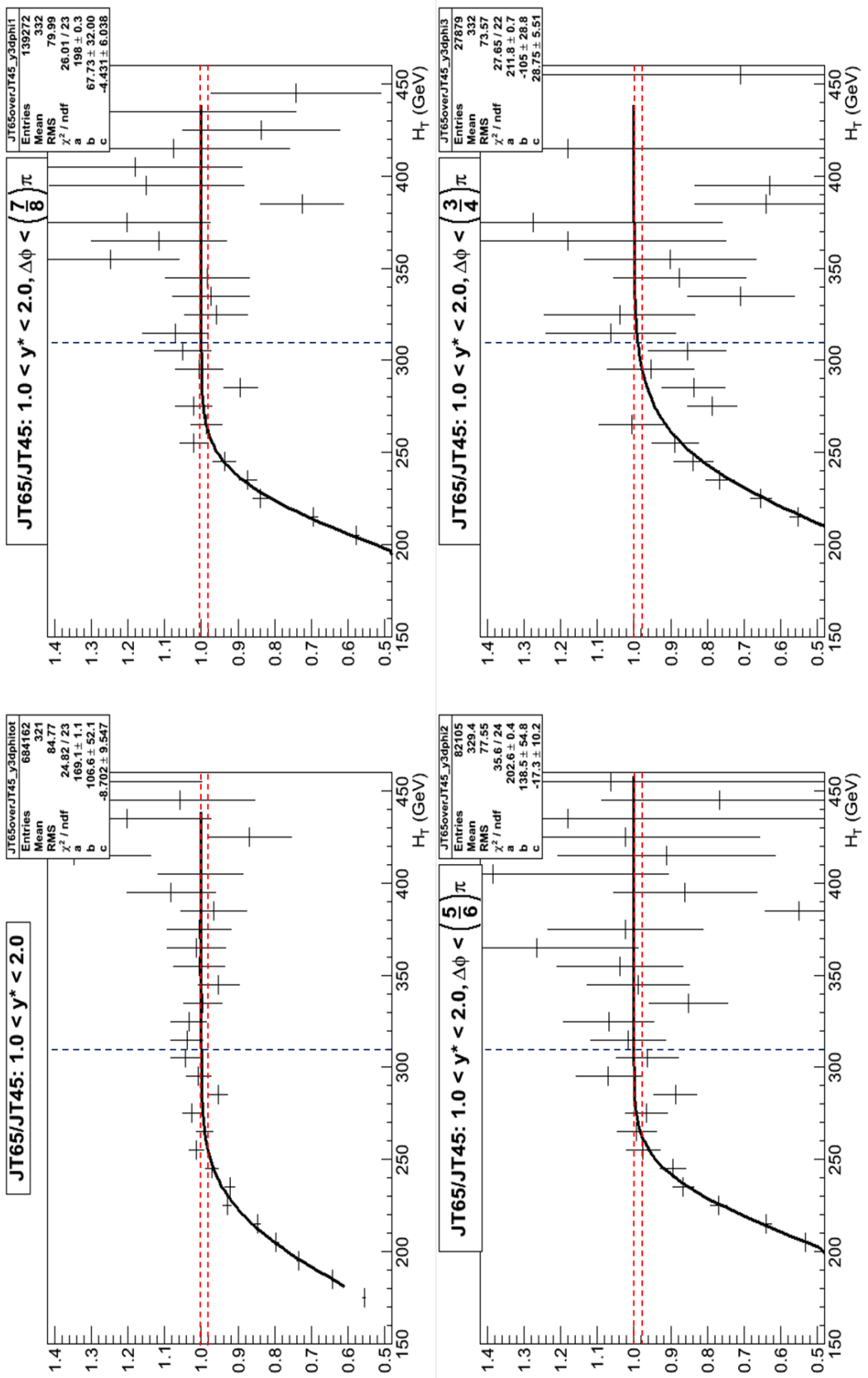


Figure A.5: Trigger turn-on curves (Trigger: JT65; $0.5 < y^* < 1.0$)

Figure A.6: Trigger turn-on curves (Trigger: JT65; $1.0 < y^* < 2.0$)

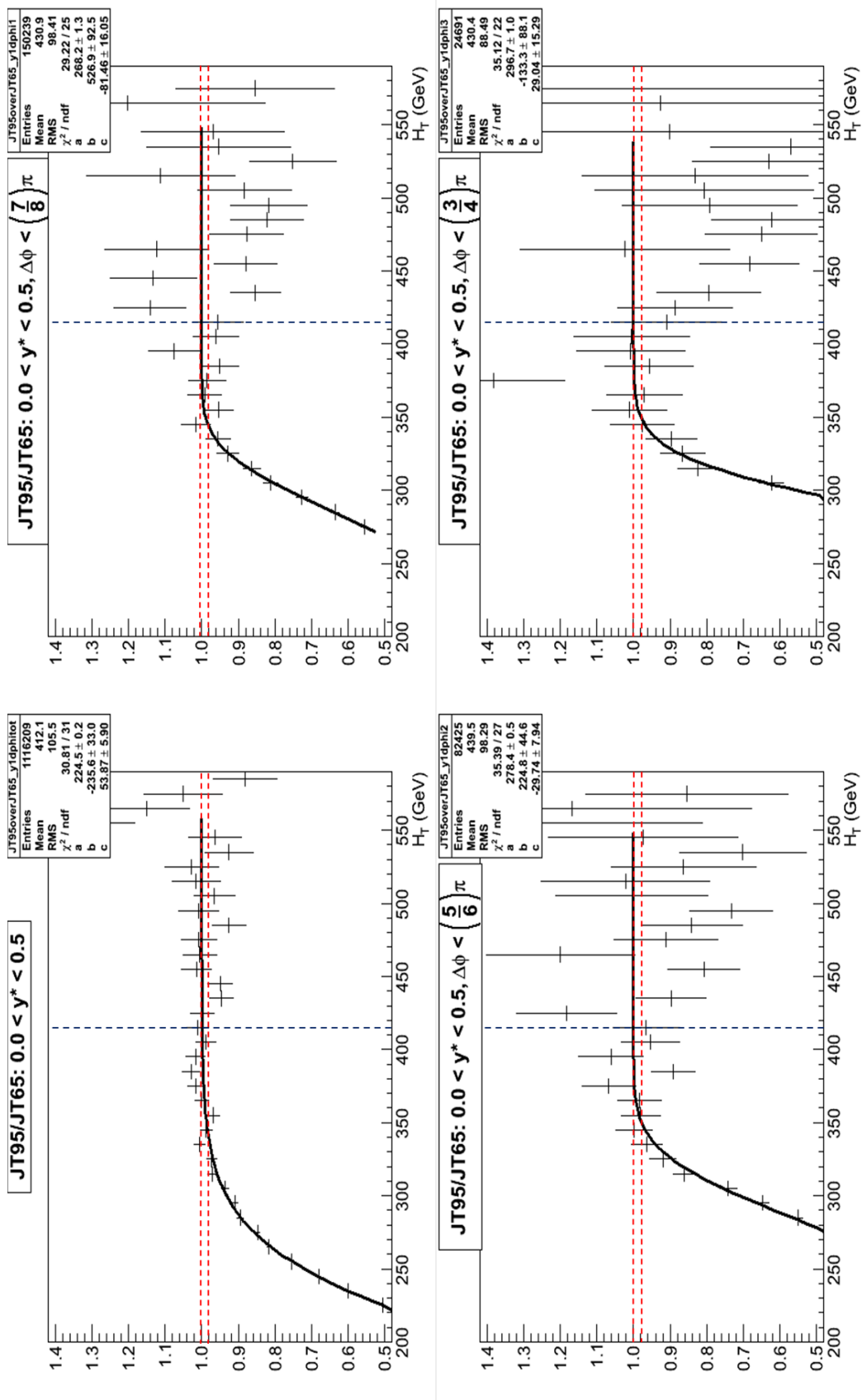


Figure A.7: Trigger turn-on curves (Trigger: JT95; $0.0 < y^* < 0.5$)

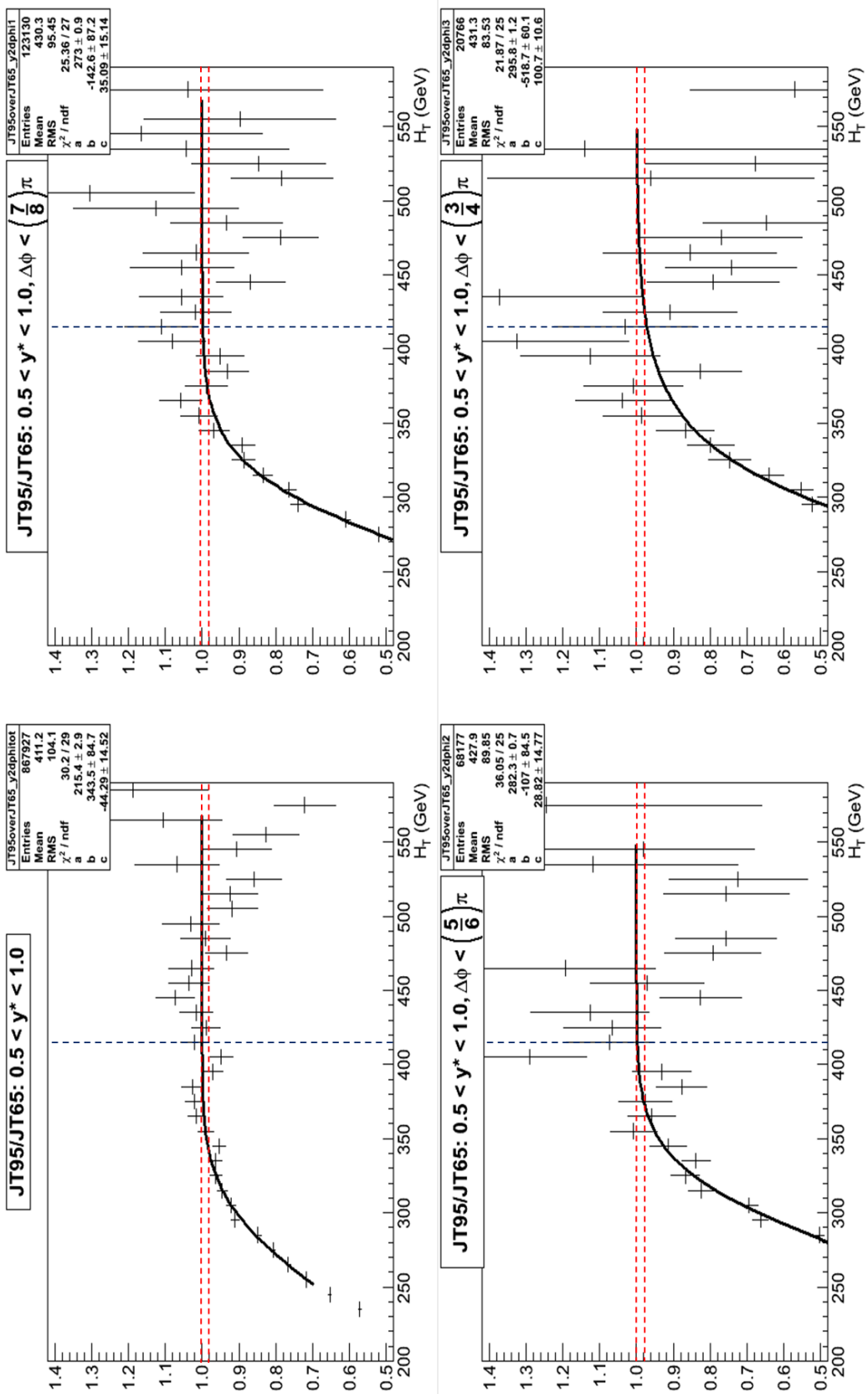


Figure A.8: Trigger turn-on curves (Trigger: JT95; $0.5 < y^* < 1.0$)

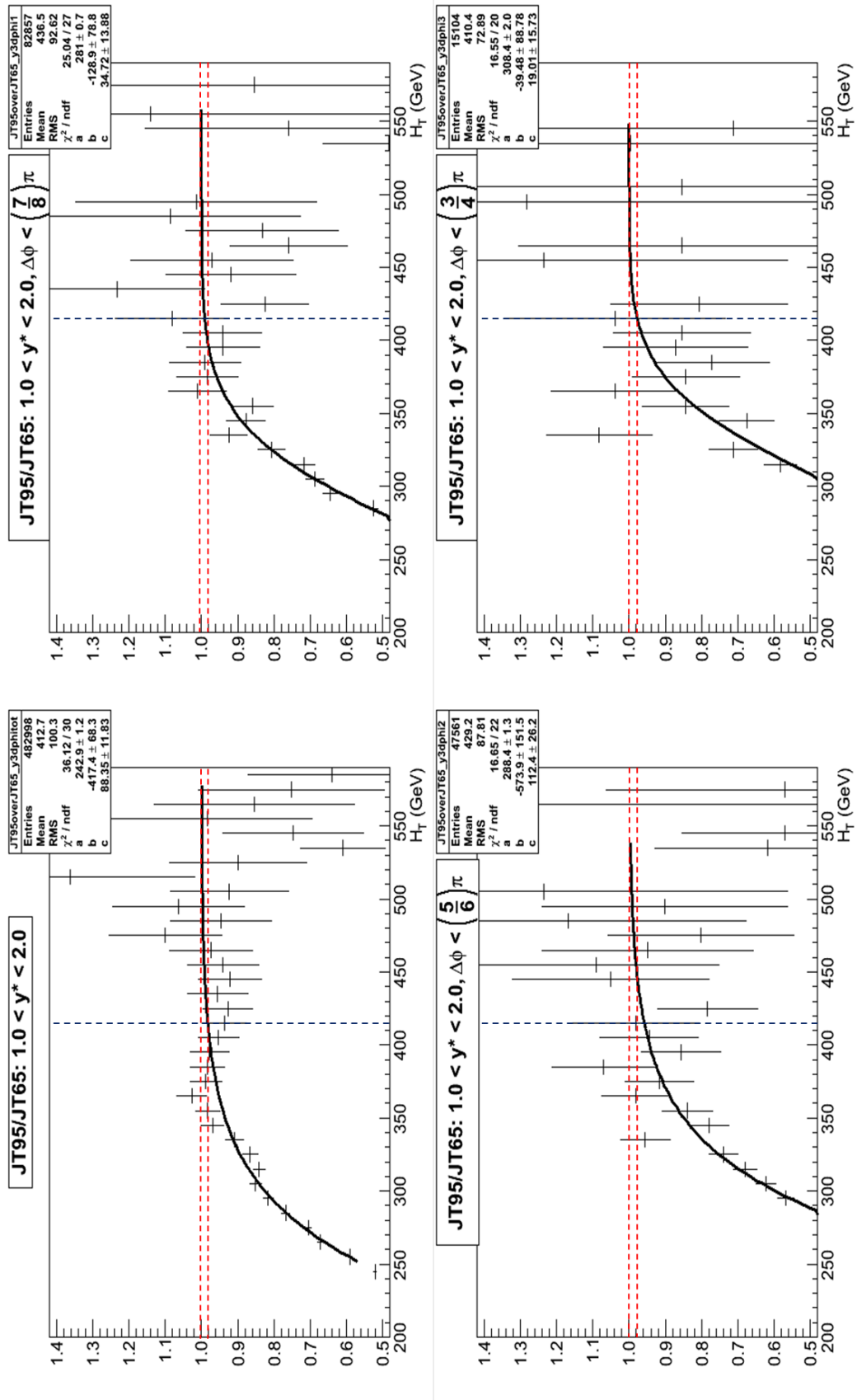


Figure A.9: Trigger turn-on curves (Trigger: JT95; $1.0 < y^* < 2.0$)

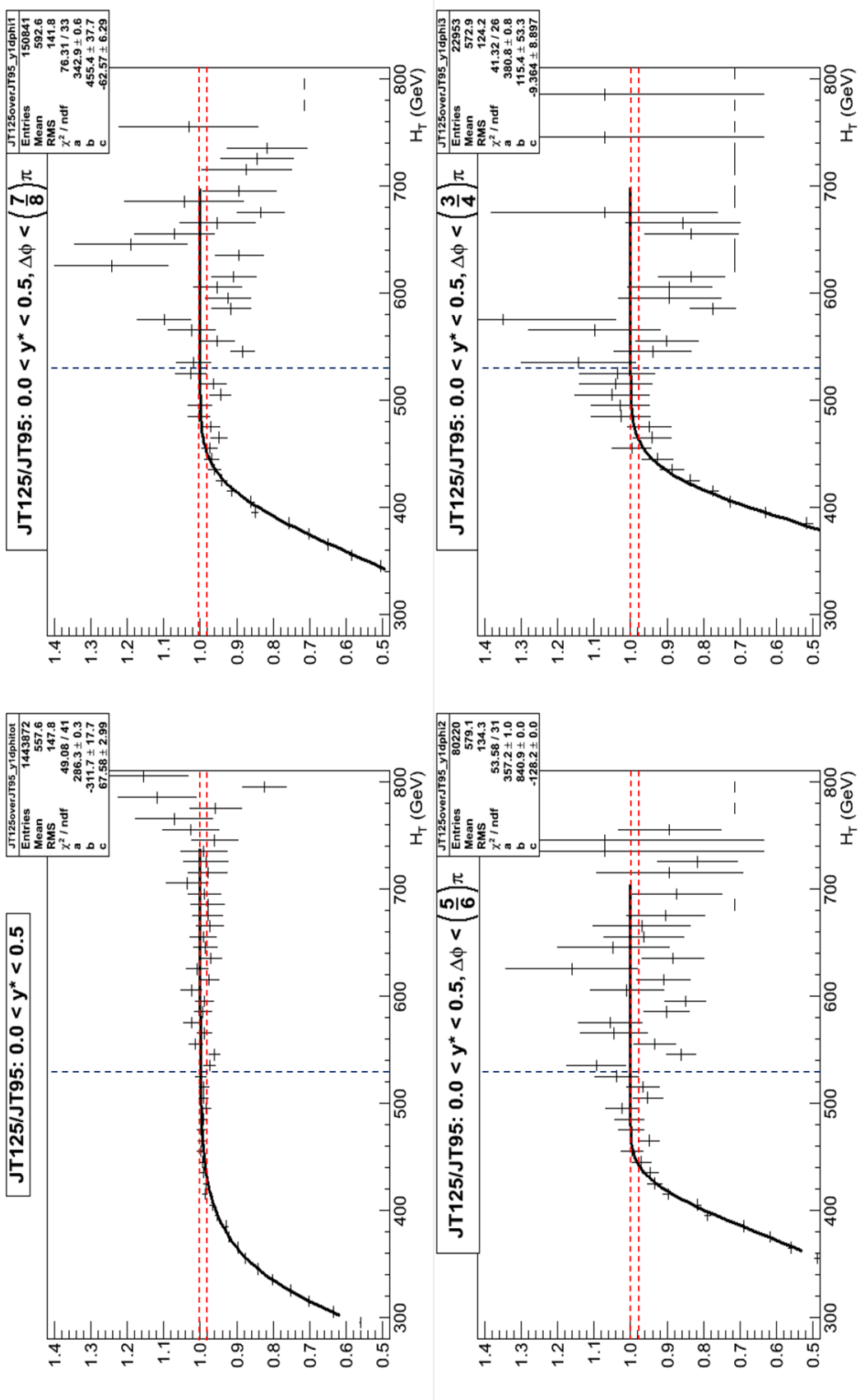


Figure A.10: Trigger turn-on curves (Trigger: JT125; $0.0 < y^* < 0.5$)

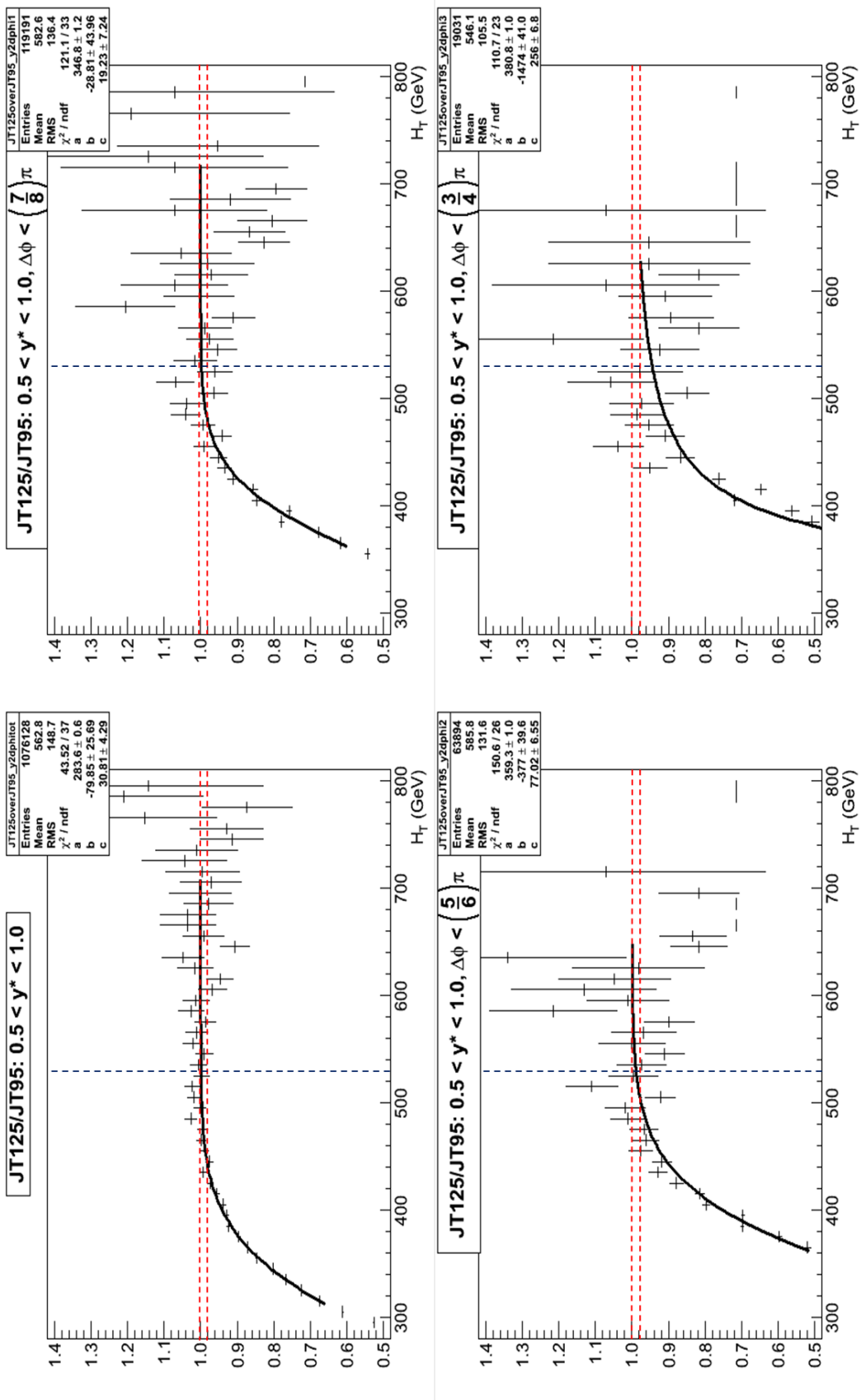


Figure A.11: Trigger turn-on curves (Trigger: JT125; $0.5 < y^* < 1.0$)

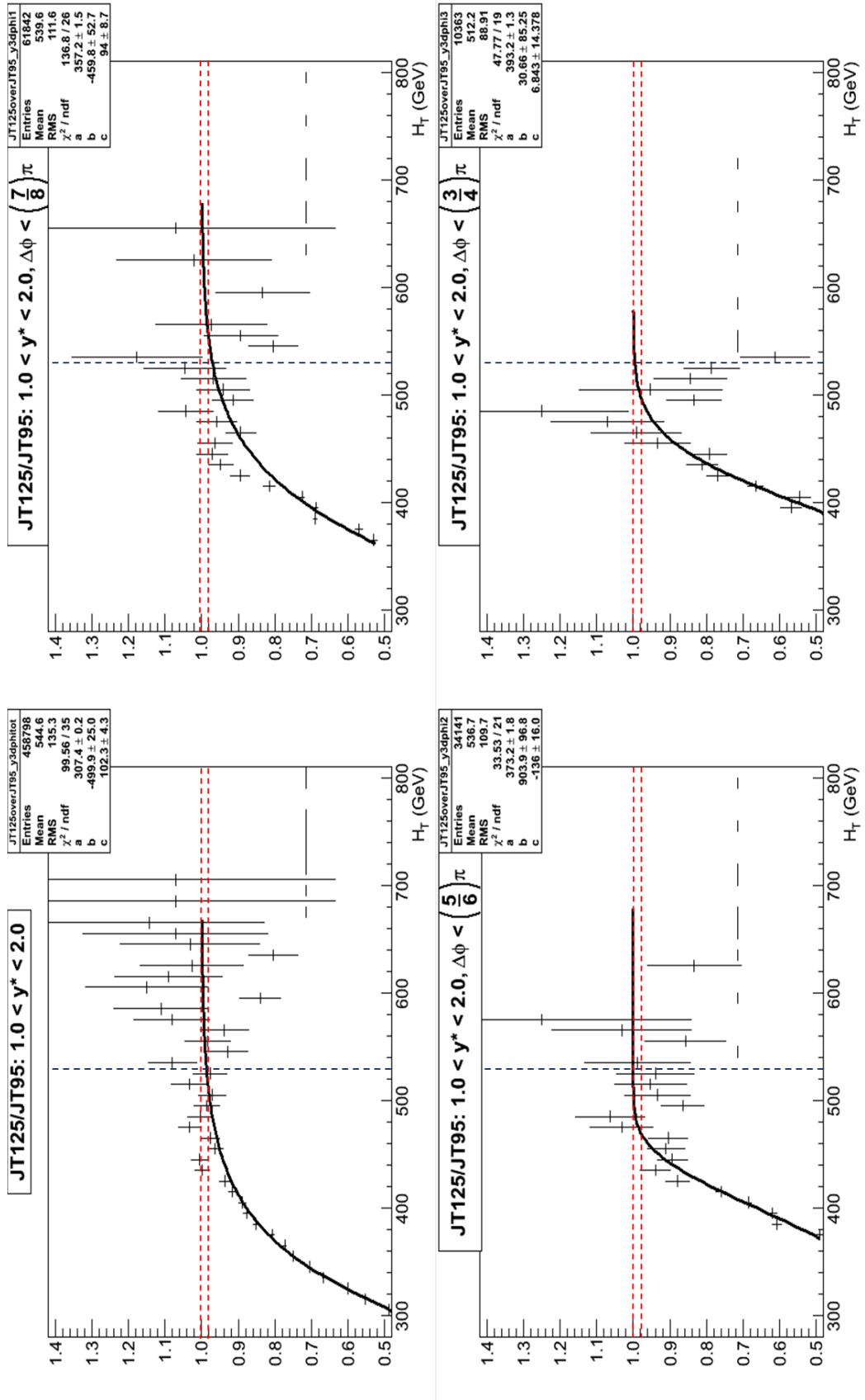


Figure A.12: Trigger turn-on curves (Trigger: JT125; $1.0 < y^* < 2.0$)

APPENDIX B

CORRECTION FACTORS

The correction factors for individual detector effects are presented in the Figures B.1 through B.5. These corrections are together applied to the data at the detector-level in order to obtain the data at the particle-level. The total correction factors thus obtained from these individual correction factors are shown in Figure 4.3. Section 3.4 introduces the motivation for these corrections and Section 4.4 explains the correction procedure.

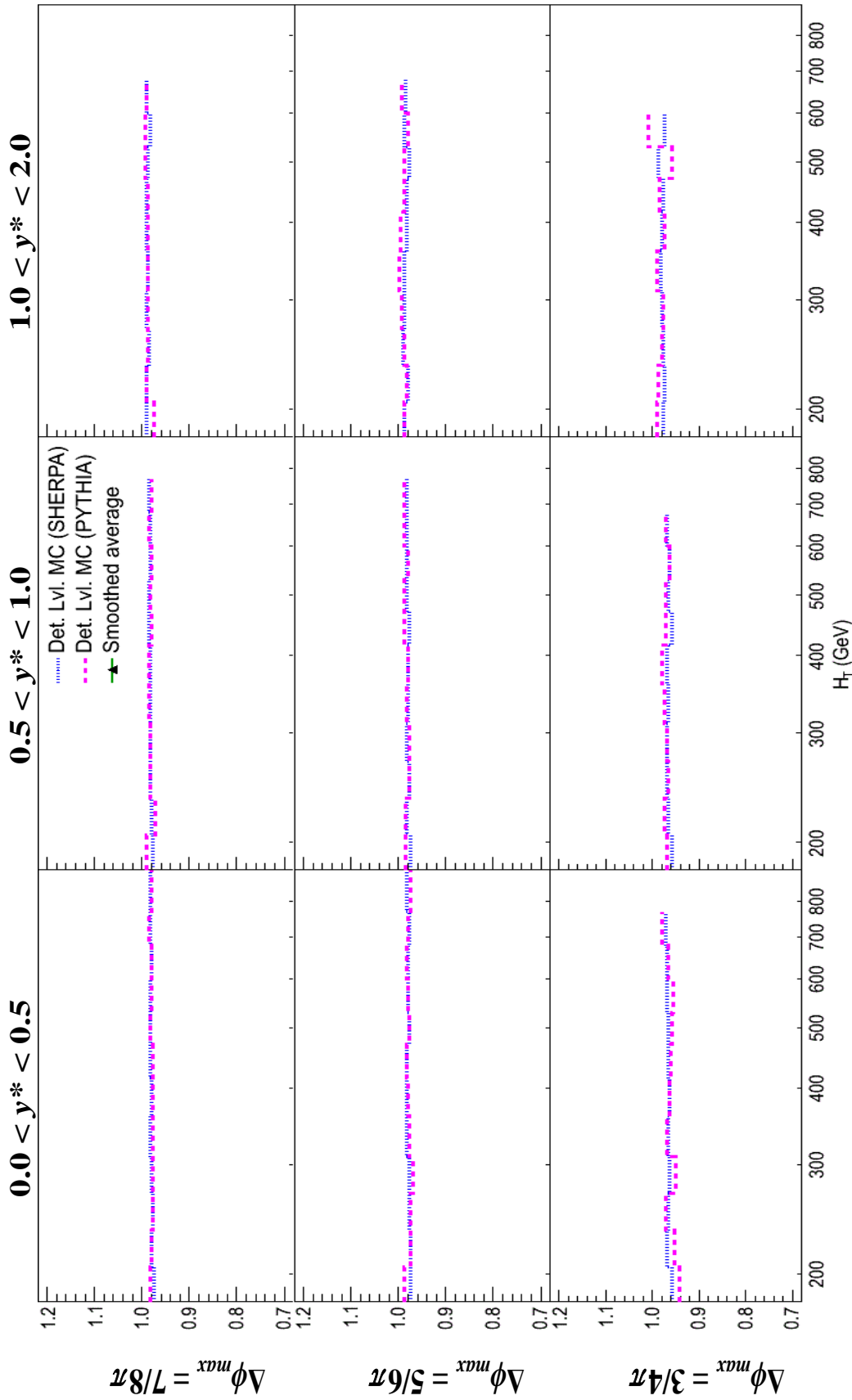


Figure B.1: Correction factors for jet ID efficiency, obtained from fast-parametrized Monte Carlo simulations

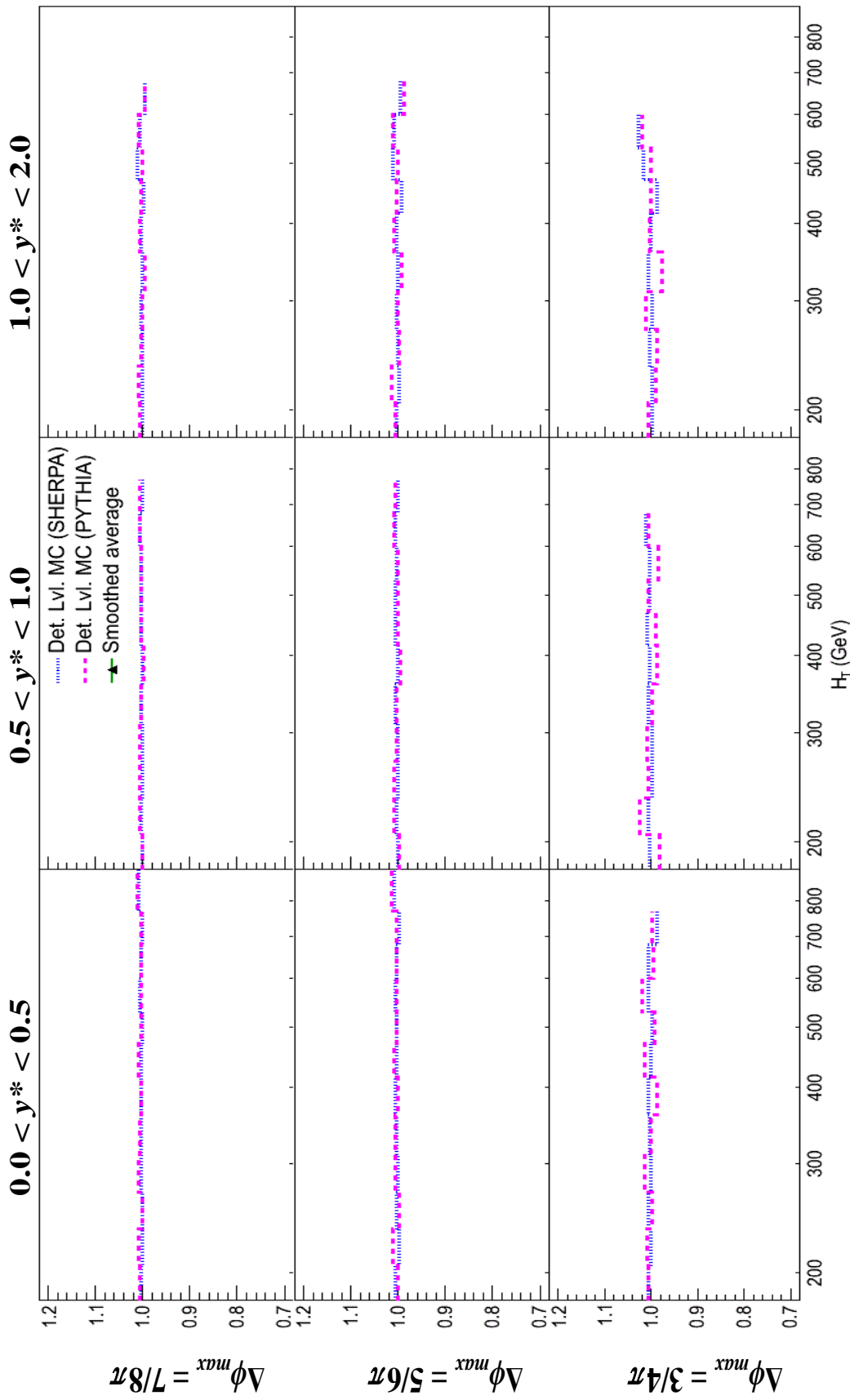


Figure B.2: Correction factors for inclusion of muons and neutrinos, obtained from fast-parametrized Monte Carlo simulations

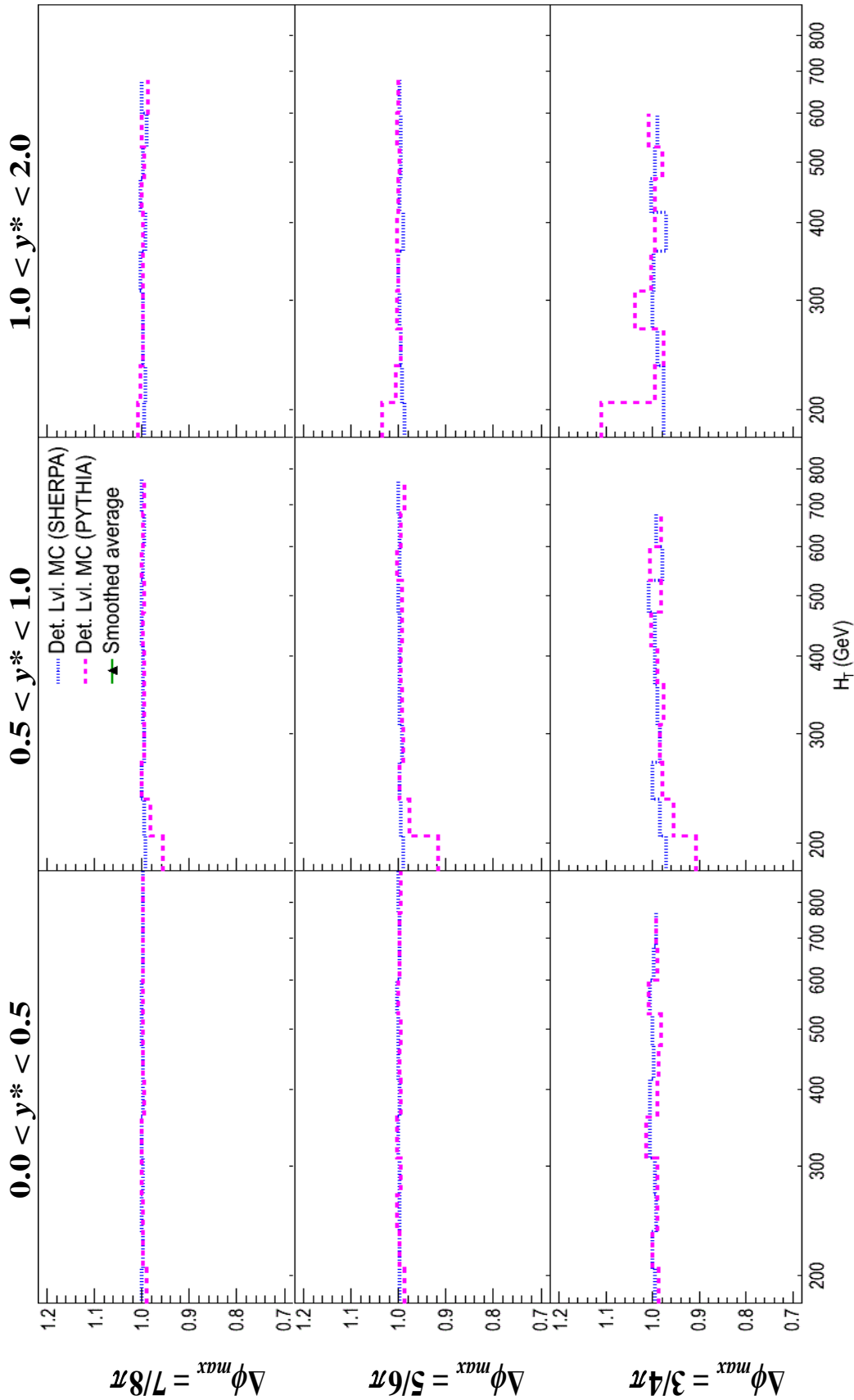


Figure B.3: Correction factors for η resolution, obtained from fast-parametrized Monte Carlo simulations

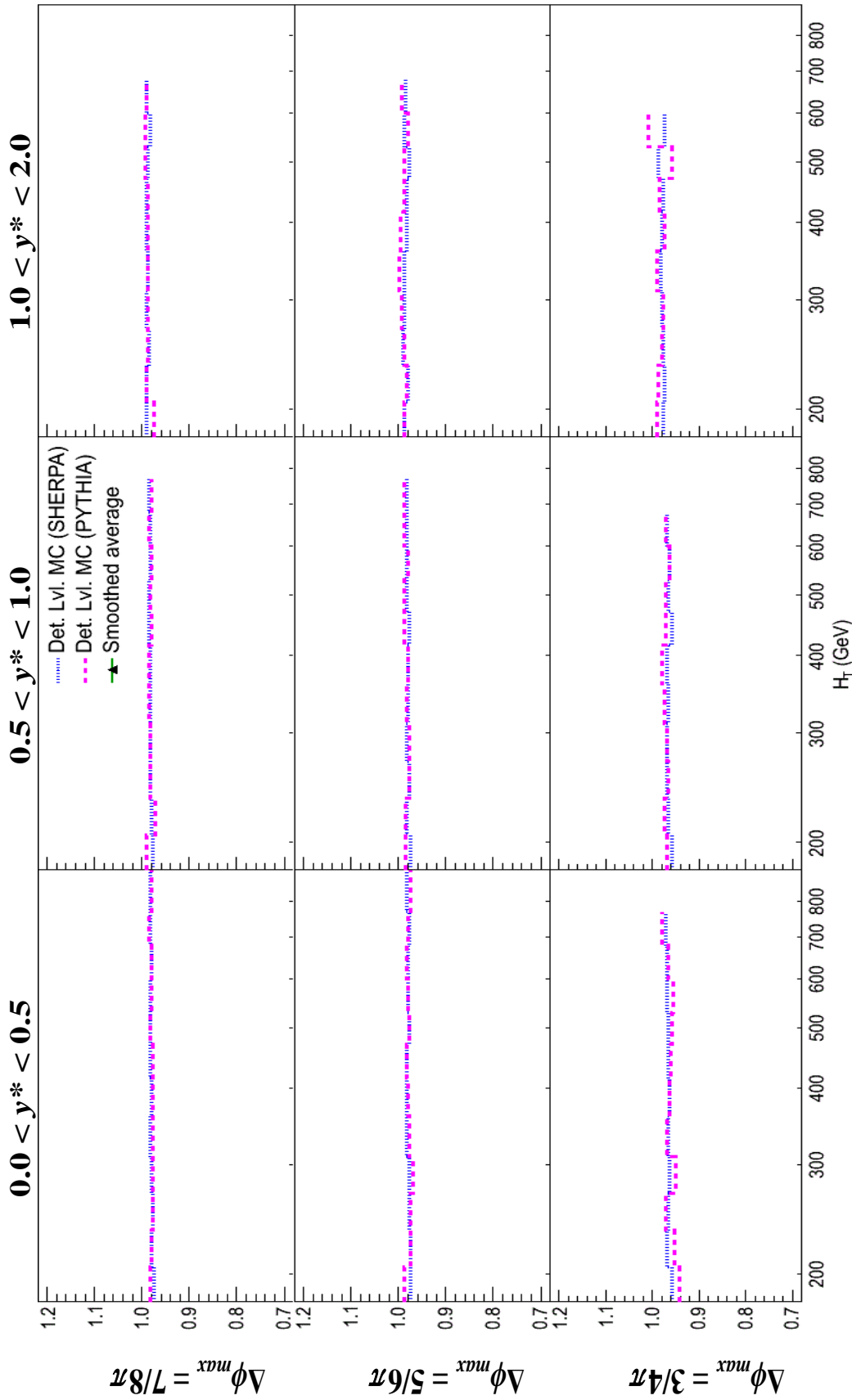


Figure B.4: Correction factors for ϕ resolution, obtained from fast-parametrized Monte Carlo simulations

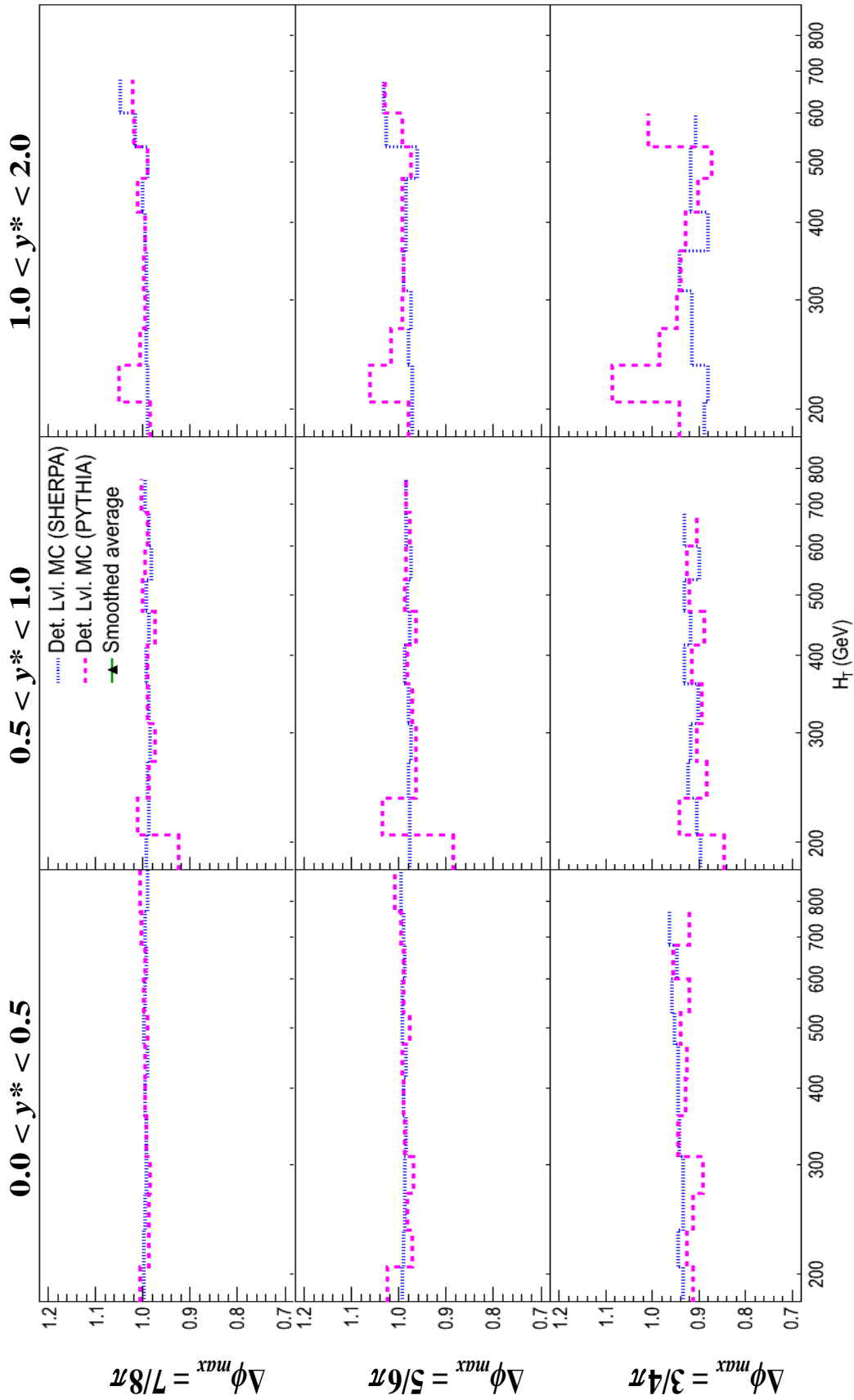


Figure B.5: Correction factors for p_T resolution, obtained from fast-parametrized Monte Carlo simulations

APPENDIX C

SYSTEMATIC UNCERTAINTIES

Figures C.1 through C.7 present the upper and lower variations of various systematic uncertainties that affect the data. The total systematic uncertainties shown in Figure 4.4 are a combination of all these individual uncertainties in the respective y^* regions and for the respective $\Delta\phi_{max}$ requirements. Section 4.5 outlines how these uncertainties are applied to the data.

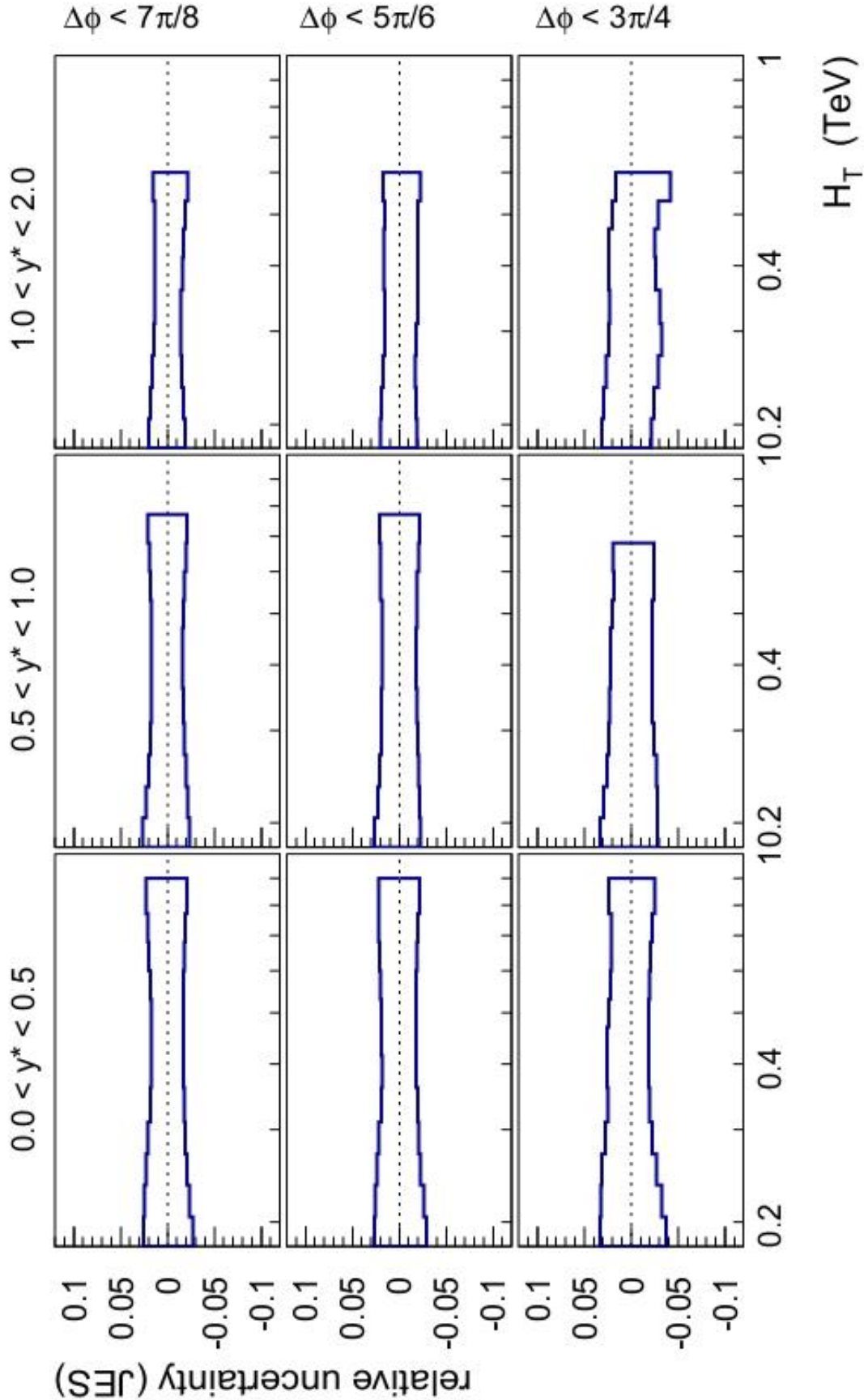


Figure C.1: Upper and lower variation of the JES uncertainty

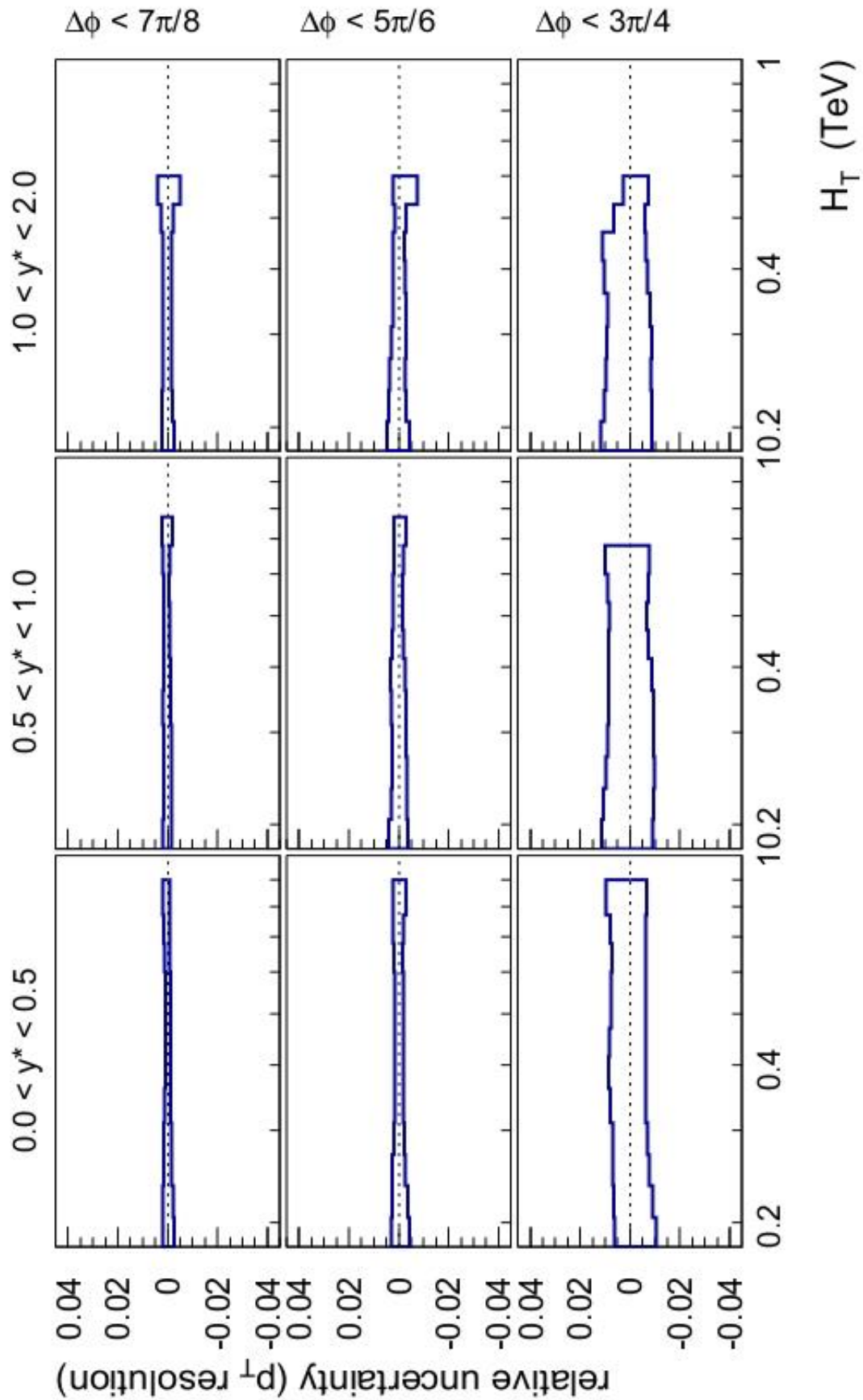


Figure C.2: Upper and lower variation of the p_T resolution uncertainty

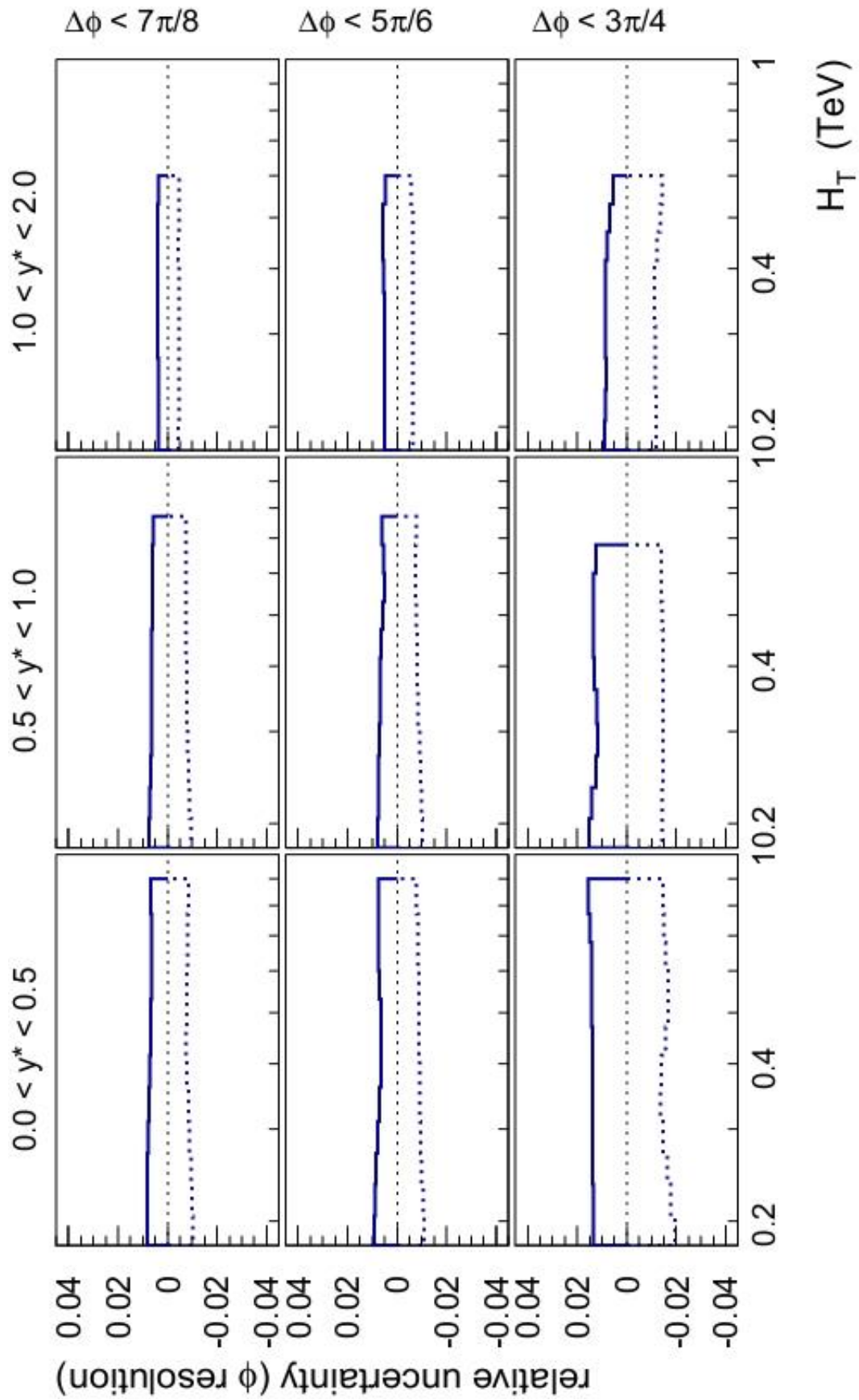


Figure C.3: Upper and lower variation of the ϕ uncertainty

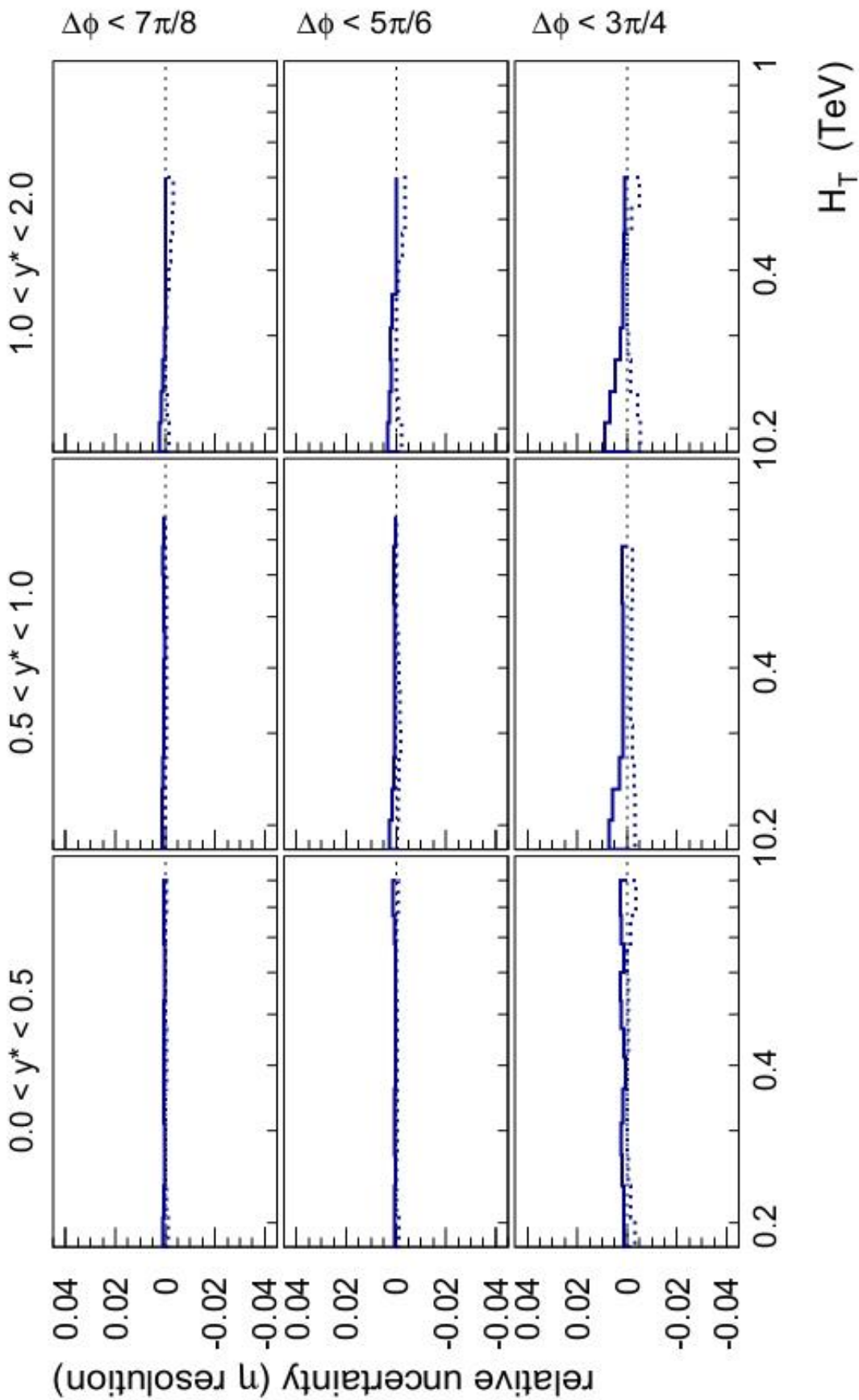


Figure C.4: Upper and lower variation of the η resolution uncertainty

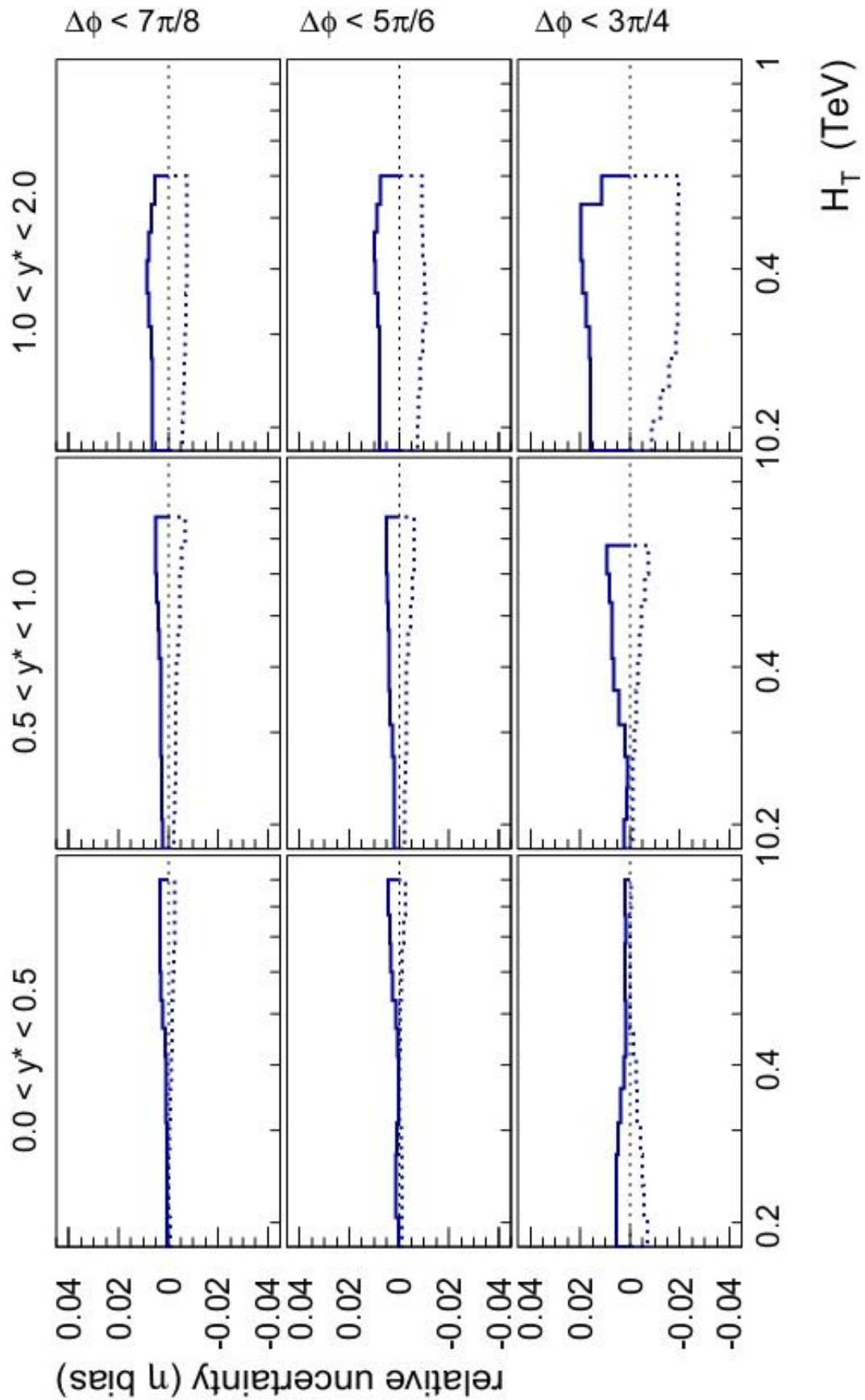


Figure C.5: Upper and lower variation of the η bias uncertainty

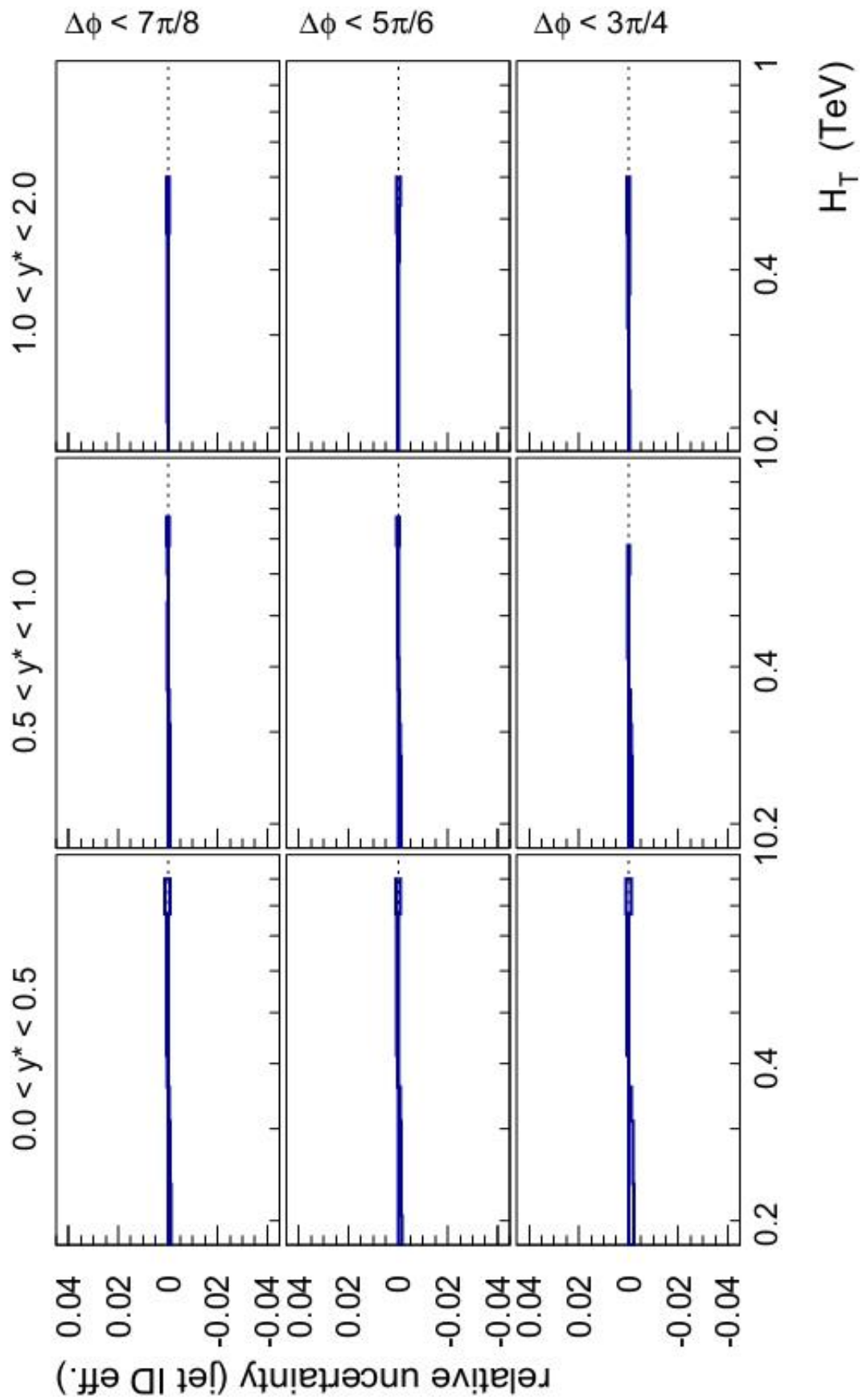


Figure C.6: Upper and lower variation of the jet ID efficiency uncertainty

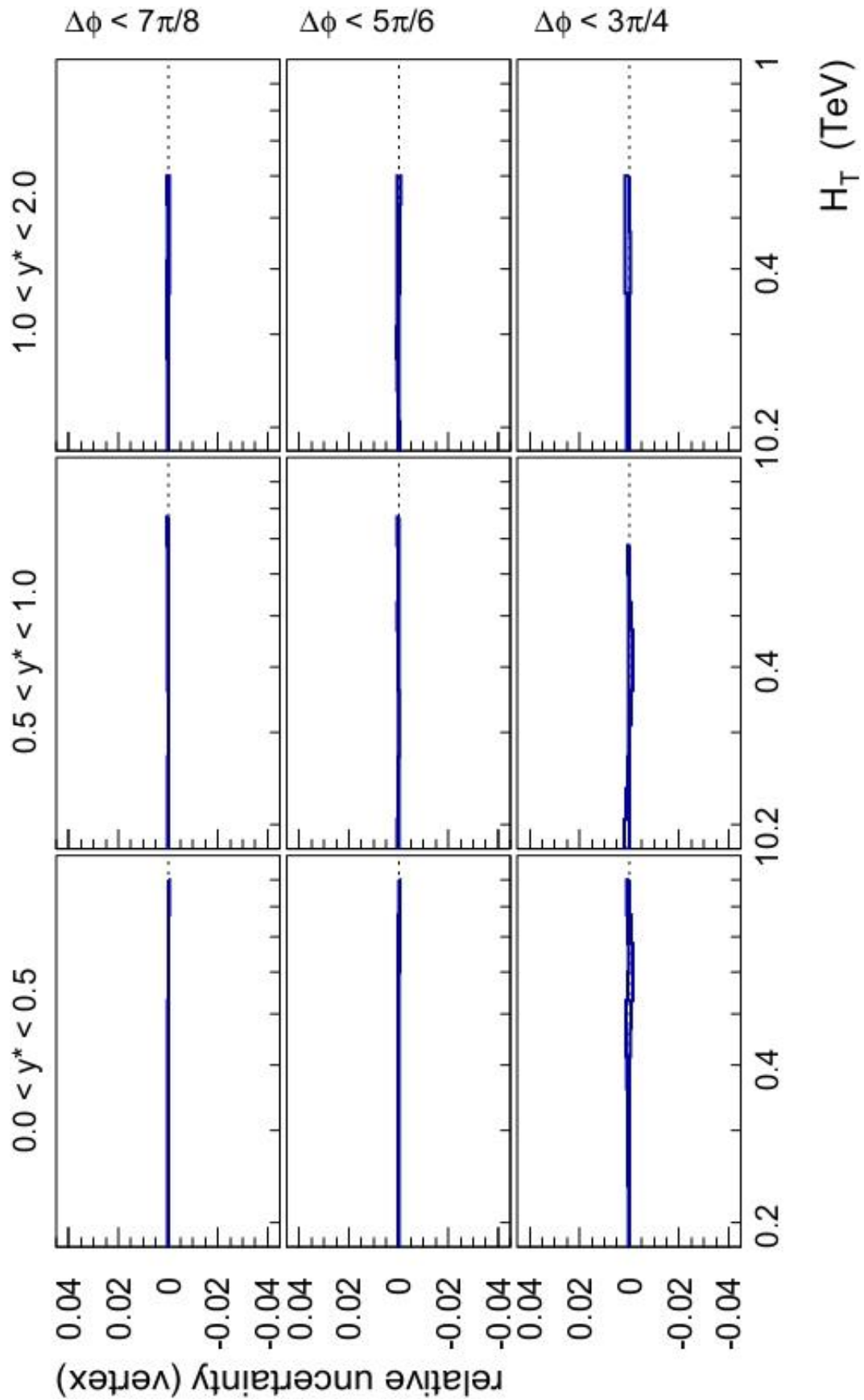


Figure C.7: Upper and lower variation of the vertex uncertainty

BIBLIOGRAPHY

- [1] V. M. Abazov *et al.* (DØ Collaboration), Phys. Rev. Lett. **94**, 221801 (2005).
<[arXiv:hep-ex/0409040v1](https://arxiv.org/abs/hep-ex/0409040v1)>
- [2] L. M. Brown, M. Riordan, M. Dresden, and L. Hoddesen in *The Rise of The Standard Model: Particle Physics in the 1960s and 1970s*, edited by L. Hoddesen, L. M. Brown, M. Riordan and M. Dresden (Cambridge University Press, 1999), p. 3.
- [3] CERN Video productions, *4th July 2012, Press Conference. Update on the Higgs Boson searches at the LHC* (2012). <[CERN-MOVIE-2012-101](https://cds.cern.ch/record/1420000)>
- [4] K. Nakamura *et al.* (Particle Data Group), J. Phys. G **37**, 075021 (2010).
- [5] G. Sterman *et al.* (The CTEQ Collaboration), Rev. Mod. Phys. **67**, 157 (1995).
- [6] W. Greiner, S. Schramm and E. Stein, *Quantum Chromodynamics* (Springer, Germany, 2002).
- [7] S. M. Bilenky, *Introduction to Feynman Diagrams*, translated and edited by F. Pardee (Pergamon Press, Hungary, 1974).
- [8] W. A. Bardeen *et al.*, Phys. Rev. D, **18**, 3998 (1978).
- [9] S. Bethke, Eur. Phys. J. C **64**, 689 (2009). <[arXiv:0908.1135v2 \[hep-ph\]](https://arxiv.org/abs/0908.1135v2)>
- [10] D. E. Soper, Nucl. Phys. (Proc. Suppl.) **53**, 69 (1997). <[arXiv:hep-lat/9609018v1](https://arxiv.org/abs/hep-lat/9609018v1)>
- [11] H.-L. Lai *et al.*, Phys. Rev. D **82**, 074024 (2010). <[arXiv:1007.2241v3 \[hep-ph\]](https://arxiv.org/abs/1007.2241v3)>

- [12] B. Abbott *et al.* (DØ Collaboration), Phys. Rev. D, **64**, 032003 (2001). <[arXiv:hep-ex/0012046](#)>
- [13] V. M. Abazov *et al.* (DØ Collaboration), Nucl. Instrum. Methods Phys. Res. A, **565**, 463 (2006). <[arXiv:physics/0507191v1](#)>
- [14] A. R. Baden and N. J. Hadley, DØ Note No. 957, 1993 (unpublished).
- [15] G. Blazey *et al.*, in *Proceedings of the Workshop: QCD and Weak Boson Physics in Run II, 2000* (FERMILAB-PUB-00-297), edited by U. Baur, R. K. Ellis, D. Zeppenfeld. <[arXiv:hep-ex/0005012v2](#)>.
- [16] M. Albrow *et al.* (TeV4LHC QCD Working Group), FERMILAB-CONF-06-359 (2006). <[arXiv:hep-ph/0610012v1](#)>
- [17] T. Kluge, K. Rabbertz, and M. Wobisch, in “*Tevatron-for-LHC Report of the QCD Working Group*”, edited by M. Carena and S. Mrenna (DESY 06-186 and FERMILAB-CONF-06-352-E, 2006), p. 58. <[arXiv:hep-ph/0609285v2](#)>
- [18] Z. Nagy, Phys. Rev. Lett. **88**, 122003 (2002).
- [19] Z. Nagy, Phys. Rev. D **68**, 094002 (2003).
- [20] G. Aad *et al.* (The ATLAS Collaboration), New J. Phys. **13**, 053033 (2011). <[arXiv:1012.5104v2 \[hep-ex\]](#)>
- [21] S. Ellis *et al.*, Prog. Part. Nucl. Phys. **60**, 484 (2008). <[arXiv:0712.2447 \[hep-ph\]](#)>
- [22] JES Group, DØ Note No. 5382, 2007 (unpublished).
- [23] M. Voutilainen, DØ Note No. 5550, 2007 (unpublished).
- [24] R. Brun and F. Carminati, CERN Program Library Long Writeup W5013, 1993 (unpublished).
- [25] Z. Hubacek *et al.*, DØ Note No. 5703, 2008 (unpublished).

- [26] A. D. Martin *et al.*, Eur. Phys. J. C **63**, 189 (2009). <[arXiv:0901.0002v3 \[hep-ph\]](#)>
- [27] T. Sjöstrand *et al.*, Comput. Phys. Commun. **135**, 238 (2001). <[arXiv:hep-ph/0010017](#)>
- [28] L. Sawyer and M. Wobisch, DØ Note No. 6278, 2012 (unpublished).
- [29] I. Antcheva *et al.*, Comput. Phys. Commun. **182**, 1384 (2011).
- [30] A. Harel, DØ Note No. 4919, 2005 (unpublished).
- [31] M. Voutilainen, Ph.D. Dissertation, Helsinki University of Technology (2008).
- [32] T. Gleisberg *et al.*, J. High Energy Phys. **0902**, 007 (2009). <[arXiv:0811.4622 \[hep-ph\]](#)>
- [33] T. Sjöstrand, Comput. Phys. Commun. **82**, 74 (1994).
- [34] S. Atkins, L. Sawyer, and M. Wobisch, DØ Note No. 5820, 2009 (unpublished).
- [35] J. Friedman, in Proceedings of the 1974 CERN School of Computing, Norway, 11-24 August, 1974.
- [36] L. Sawyer and M. Wobisch, DØ Note No. 6279, 2012 (unpublished).
- [37] V. Khachatryan *et al.* (The CMS Collaboration), Phys. Rev. Lett. **106**, 122003 (2011). <[arXiv:1101.5029v2 \[hep-ex\]](#)>
- [38] G. Aad *et al.* (The ATLAS Collaboration), Phys. Rev. Lett. **106**, 172002 (2011). <[arXiv:1102.2696v2 \[hep-ex\]](#)>